

Radiation Damage
Effects within Materials

By

Joel Davis

A Thesis Submitted for the degree of
Master of Science by Research

University of Technology, Sydney

2015

CERTIFICATE OF ORIGINAL AUTHORSHIP

I certify that the work in this thesis has not previously been submitted for a degree nor has it been submitted as part of requirements for a degree except as fully acknowledged within the text.

I also certify that the thesis has been written by me. Any help that I have received in my research work and the preparation of the thesis itself has been acknowledged. In addition, I certify that all information sources and literature used are indicated in the thesis.

Signature of Student Joel Davis:

Date:

ACKNOWLEDGEMENTS

I would like to thank my supervisors Professor Matthew Phillips (UTS), Dr Richard Wuhrer (UWS) and Dr Greg Lumpkin (ANSTO) for their support and assistance throughout this project.

I would also like to thank Dr Ken Short and Mihail Ionescu (ANSTO) for assistance with ion implantation on the PI³ and STAR accelerators.

I would like to thank Mark Blackford and Robert Aughterson (ANSTO) for their assistance with transmission electron microscopy.

I would like to make an extended special thanks to Dr Ric Wuhrer for his friendship, motivation and technical contributions during this project, without his assistance, time and effort this project would not have been possible.

Finally I would like to thank the ANSTO department of Materials Engineering for supporting me through this project and allowing access to all the instrumentation required.

TABLE OF CONTENTS

TITLE PAGE.....	I
CERTIFICATE OF ORIGINAL AUTHORSHIP.....	II
ACKNOWLEDGMENTS.....	III
TABLE OF CONTENTS.....	IV
LIST OF FIGURES.....	VI
LIST OF TABLES.....	IX
TABLE OF ACRONYMS.....	X
ABSTRACT.....	XII
1 INTRODUCTION.....	1
1.1 Background.....	1
1.2 Significance of this Research.....	2
1.3 Aims and Objectives.....	2
1.4 Statement of Main Findings.....	3
1.5 Publications arising from this Work.....	5
2 LITERATURE REVIEW: NUCLEAR REACTORS & MATERIALS.....	6
2.1 Introduction.....	6
2.2 Nuclear Reactors.....	6
2.3 Current Reactor Materials.....	9
2.4 New Reactor Materials.....	10
3 Literature Review RADIATION DAMAGE.....	16
3.1 Introduction.....	16
3.2 Types of Radiation Damage.....	16
3.3 Radiation Damage Characterization.....	18
4 EXPERIMENTAL: RADIATION DAMAGE & TESTING METHODS.....	28
4.1 Introduction.....	28
4.2 Ion Implantation Versus Neutron Irradiation.....	28
4.3 Plasma Immersion Ion Implantation (PI ³).....	29
4.4 Small Tandem for Applied Research (STAR) Accelerator.....	31
4.5 Materials Selection.....	32
4.6 Instrumentation Selected.....	34
5 EXPERIMENTAL: CHARACTERISATION OF MATERIALS.....	35
5.1 Introduction.....	35
5.2 Materials.....	35
5.3 Pre Irradiation Sample Preparation.....	35
5.4 Characterisation of Materials.....	36
5.4.1 Scanning Electron Microscopy (SEM).....	36
5.4.2 SEM Secondary Electron Imaging.....	36
5.4.3 SEM Backscattered Electron and Backscattered Electron Channeling Contrast Imaging.....	37
5.4.4 Energy Dispersive X-Ray Spectroscopy (EDS).....	37
5.5 Atomic Force Microscopy Analysis (AFM).....	38
5.6 Microhardness Measurement.....	38

5.7	Electron Backscatter Diffraction (EBSD).....	38
5.8	Computer Modeling of Damage (SRIM).....	39
5.9	Cross Sectional Sample Preparation.....	39
5.10	Mechanical Polishing.....	39
5.10.1	Cross Sectional Ion Beam Polishing	40
5.10.2	Focused Ion Beam (FIB)	40
5.10.3	Precision Ion Beam Polishing (PIPS).....	41
5.11	TEM Sample Preparation	41
5.11.1	Focused Ion Beam	41
5.12	Transmission Electron Microscopy (TEM) Characterisation.....	42
6	RESULTS AND DISCUSSION.....	43
6.1	Introduction.....	43
6.2	First Initial Experiment.....	43
6.3	Second Initial Experiment:	51
6.4	Investigation of various steels.....	57
6.4.1	Investigation of 430 Grade Stainless Steel	58
6.4.2	Investigation of 304 Grade Stainless Steel	60
6.4.3	Investigation of 2205 Grade Stainless Steel	62
6.4.4	Investigation of MA956 Grade Stainless Steel.....	66
6.5	STAR Accelerator Results.....	69
6.5.1	Further investigation of the 2205 Duplex Steel.....	72
6.6	Cross-section Method Development for Shallow Damage Layers.....	76
6.6.1	Mechanical Polishing.....	76
6.6.2	Large-Scale Ion Beam Cross Sectional Polishing	77
6.6.3	Cross Section Preparation Using Focused Ion Beam	79
6.6.4	Cross Section Preparation Using Precision Ion Beam Polishing.....	80
6.6.5	EBSD study of irradiated 316 stainless steel cross section	82
6.7	Sample Preparation for Transmission Electron Microscopy	84
6.8	Transmission Electron Microscopy Results	86
6.9	Chapter Conclusion.....	90
7	CONCLUSIONS AND FUTURE WORK.....	92

REFERENCES

APPENDICES

LIST OF FIGURES

Figure 2-1: Schematic diagram of a nuclear power plant using a pressurised-water reactor, the most common commercially used type of fission power reactor. [Encyclopaedia Britannica Inc.]	7
Figure 2-2: The ITER tokamak reactor design. The fuel is contained in a doughnut-shaped vessel and heated to 10 times the temperature of the sun’s core, forming a plasma. [iter.org].....	8
Figure 3-1: The energy spectrum for neutrons taken from a variety of reactor types and a monoenergetic proton beam. Reproduced from Stoller, R. E.; Greenwood, L. R. J. Nucl. Mater. 1999, 271–272, 57–62.	20
Figure 3-2: Primary knock-on atom (PKA) damage fraction produced as a function of PKA energy for three neutron spectra (DEMO, IFMIF, and HFR) compared with ion-beams (20MeV and 10MeV heavy ions). Serruys et al. (2008) [38].....	21
Figure 4-1: Plasma immersion ion implantation (PI ³) instrument used for this project, which is housed at the Institute of Materials Engineering, ANSTO.	30
Figure 4-2: Schematic diagram showing the plasma immersion ion implantation (PI ³) process [54].	31
Figure 4-3: The STAR accelerator used for this project, which is housed at the Centre for Accelerator Science, ANSTO.	32
Figure 6-1: Atomic Force Microscopy (AFM) showing some evidence (13 nm) of sputtering and surface degradation was measured when using argon ions.	44
Figure 6-2: Optical image showing the regions where instrumented indentation was performed in the shielded and irradiated regions.	44
Figure 6-3: Results from the instrumented indentation to a maximum load of 250 mN as performed on the shielded region of the argon implanted steel.	45
Figure 6-4: Results from the instrumented indentation to a maximum load of 250 mN as performed on the unshielded region of the argon implanted steel.	45
Figure 6-5: EBSD Map of 316 stainless steel before ion implantation. Map shows euler angle colouring with a very high pattern indexing rate.	46
Figure 6-6: Backscattered electron image showing the irradiated and shielded regions and also the region where the EBSD map was taken from on the polished stainless steel surface. Argon ions were used for implantation.	47
Figure 6-7: Corresponding EBSD map showing the loss of EBSD pattern indexing in the irradiated region (top of map).	48
Figure 6-8: Backscattered electron image showing the irradiated and shielded regions and also the region where the EBSD map was taken from on the polished stainless steel surface. Helium ions were used for implantation.	49
Figure 6-9: Corresponding EBSD map showing the loss of EBSD pattern in the irradiated region (right hand side of the map). Note the area mapped was shielded using a silicon wafer and gave a gradient of damage across the mapped region unlike the hard edge given by the TEM grid used in figure 6.8.	49
Figure 6-10: EDS spectrum showing argon present in the stainless steel ~0.2 weight % was found. However, this may not be considered representative of the true concentration as the interaction volume of X-ray generation will be predominantly below the region of deposited argon into the surface of the steel. As a result the fraction of argon present maybe higher.	50
Figure 6-11: Secondary electron image showing the irradiated region.....	52
Figure 6-12: Corresponding EBSD line scans showing the EBSD pattern is still present in the irradiated region.....	53

Figure 6-13: Secondary electron image showing the cross-section of the irradiated region mounted in epoxy resin and polished to a 1 micron diamond finish. Figure 6-14 below shows this region in high magnification.....	54
Figure 6-14: Backscattered electron channeling contrast image showing the cross-section of the irradiated region and a line of radiation damage caused by the helium ions approximately 10µm under the surface. Scratches remain in the top edge of the cross section due to edge rounding during mechanical polishing.....	55
Figure 6-15: Secondary electron image showing the cross-section of the irradiated sample after heavy etching. The line of radiation damage caused by the helium ions approximately 10µm under the surface has been completely etched away.	56
Figure 6-16: Backscattered electron channeling contrast image showing the irradiated and shielded regions of the 430 grade stainless steel. The region where the EBSD map was taken from on the polished stainless steel surface is also shown. Helium ions were used for implantation.....	59
Figure 6-17: EBSD orientation map showing the partial indexing of the EBSD pattern in the non-shielded irradiated region (lower half) of the 430 grade stainless steel.	60
Figure 6-18: Backscattered electron channelling contrast image showing the irradiated (lower) and shielded region (upper) of the 304 grade stainless steel. Helium ions were used for implantation.	61
Figure 6-19: EBSD orientation map showing the complete loss of indexing of the EBSD pattern in the irradiated region (lower half) of the 304 grade stainless steel.....	62
Figure 6-20: Backscattered electron channeling contrast image showing the irradiated and shielded regions of the 2205 grade stainless steel. The region where the EBSD map was taken from on the polished stainless steel surface is also shown. Helium ions were used for implantation.....	63
Figure 6-21: EBSD orientation map showing the partial or complete loss of pattern indexing from the grains in the irradiated region (lower half) of the 2205 grade steel.	64
Figure 6-22: EBSD phase map showing the irradiated region (lower half) of the 2205 grade steel. The red colour is the FCC phase and the blue colour is the BCC phase. We can see that in the irradiated region (lower half) that the FCC phase was not able to be indexed however the BCC phase still shows partial indexing.	65
Figure 6-23: Backscattered electron channeling contrast image showing the irradiated (lower) and shielded region (upper) of the MA956 grade stainless steel. Helium ions were used for implantation.....	67
Figure 6-24: EBSD orientation map showing the partial indexing of the EBSD pattern in the irradiated region (lower half) of the MA956 grade stainless steel.....	68
Figure 6-25: Backscattered electron channeling contrast image of the 430 grade steel showing the cross-section of the irradiated region and a line of radiation damage caused by the helium ions approximately 9.7 µm under the surface.	69
Figure 6-26: Backscattered electron channeling contrast image of the 304 grade steel showing the cross-section of the irradiated region and a line of radiation damage caused by the helium ions approximately 9.6 µm under the surface.	70
Figure 6-27: Backscattered electron channeling contrast image of the 2205 grade duplex steel showing the cross-section of the irradiated region and a line of radiation damage caused by the helium ions approximately 7.6 µm under the surface.	71
Figure 6-28: Backscattered electron channeling contrast image of the MA956 grade ODS steel showing the cross-section of the irradiated region and a line of radiation damage caused by the helium ions approximately 8 µm under the surface.....	72

Figure 6-29: Backscattered electron channeling contrast image of the 2205 grade duplex steel at high magnification showing the damage region caused by the helium ions at a grain boundary.....	73
Figure 6-30: EBSD phase map of the cross section of the 2205 grade duplex steel grain boundary region showing the BCC phase in blue on the left grain and the FCC phase in red on the right grain.....	74
Figure 6-31: X-ray mapping of the cross section of the 2205 grade duplex stainless steel showing the corresponding grains as seen in figure 6.30. The X-ray mapping shows which elements are specific to the BCC and FCC phases.....	75
Figure 6-32: Illustration demonstrating the Stopping Range of Ions in Matter (SRIM) calculations put the expected peak damage layer at a depth of ~ 150 nm for 316 stainless steel.....	76
Figure 6-33: The result of mechanical polishing of the cross sectioned stainless steel samples showing edge rounding well beyond the 100nm below surface area of interest. The area above the steel is an epoxy resin which is much softer and allows for the polishing rate to differ causing the rounding of the stainless steel edge.....	77
Figure 6-34: Schematic diagram showing the method of polishing performed in the large scale ion beam cross sectional polisher. [Hitachi High Technologies America, Inc. 2015].....	78
Figure 6-35: Blank stainless steel sample prepared using the JEOL cross sectional polisher with edge retention in the sub 100nm region.	79
Figure 6-36: SEM image of the partially milled cross section using the focused ion beam.....	80
Figure 6-37: Schematic diagram of the PIPS instrument [Gatan Inc.].....	81
Figure 6-38: Precision ion beam polished cross section of the 316 stainless steel un-irradiated test sample showing excellent edge retention in the sub 150nm region.....	82
Figure 6-39: Backscattered electron channelling contrast image showing the helium ion implantation damage layer in the PIPS prepared cross section with a depth that agrees with SRIM calculations.	83
Figure 6-40: EBSD band contrast map (left) and orientation map (right) of the cross section showing a partial loss of indexing in the damage region.	84
Figure 6-41: EBSD map of the area in the irradiated region to determine the grain boundary of interest prior to FIB milling.	86
Figure 6-42: Low magnification STEM image of the FIB prepared cross section showing the grain boundary of the helium implanted duplex stainless steel. BCC phase is the lower region; FCC phase is the upper region.....	88
Figure 6-43: High magnification TEM image showing the grain boundary between the two phases. We can see in this image the significant increase in the amount of defects in the FCC phase compared to the BCC phase.....	89
Figure 6-44: TEM images of the grain boundary between phases shown in under-focus (left) and over-focus (right) condition. The lower images are digitally blown up regions of the corresponding images above for ease of viewing. Fresnel-contrast imaging is used to reveal the voids and point defects in the damage layer.....	90

LIST OF TABLES

Table 2-1: Table showing commercial nuclear reactors currently in use and proposed designs [10 - 33].	9
Table 4-1: Table showing materials used in various types of nuclear reactors. M.T. Simnad, Nuclear reactor materials and fuels, in Encyclopedia of Physical Science and Technology, Third Edition, R.A. Meyers (Ed.), Academic Press, 2001, pp. 775 – 815.	33
Table 5-1: Compositions and crystal structures of the stainless steel materials being studied in this project.	35
Table 6-1: Compositions and crystal structures of the stainless steel materials being studied in this project.	58

TABLE OF ACRONYMS

AFM	Atomic force microscopy
AGR	Advanced gas-cooled reactor
ANSTO	Australian nuclear science and technology organisation
ASB	Angular selective backscatter
BCC	Body centred cubic
BSECCI	Backscattered electron channelling contrast imaging
BSEI	Backscattered electron imaging
BWR	Boiling water reactor
DEMO	DEMONstration power plant (relating to ITER)
EBS	Electron backscatter diffraction
EDS	Energy dispersive spectroscopy
FBR	Fast neutron reactor
FCC	Face centred cubic
FFTF	Fast flux test facility
FIB	Focused ion beam
HFIR	High flux isotope reactor
HFR	High flux reactor
IFMIF	International fusion materials irradiation facility
ITER	International Thermonuclear Experimental Reactor
LWGR	Light water graphite reactor
Magnox	Magnesium non-oxidising
ODS	Oxide dispersed steel
PBR	Pebble-bed reactor
PHWR	Pressurised heavy water reactor
PI ³	Plasma immersion ion implantation
PIPS	Precision ion beam polishing
PKA	Primary knock-on atom
PWR	Pressurised water reactor
RBMK	<i>reaktor bolshoy moshchnosty kanalny</i> , high-power channel reactor
RBS	Rutherford backscattering spectrometry
RF	Radio frequency

SCWR	Super critical water cooled reactor
SEM	Scanning electron microscope
SFT	Stacking fault tetrahedra
SRIM	Stopping range of ions in matter
STAR	Small tandem for applied research accelerator
STEM	Scanning transmission electron microscopy
TEM	Transmission electron microscope
TRISO	Tri-isotopic fuels
WDS	Wavelength dispersive spectroscopy
XRD	X-Ray diffraction

ABSTRACT

Radiation damage effects within materials are a key area of research as we strive to build longer lasting, safer and more economical nuclear reactors. Proposed materials must be tested in an appropriate manor to determine their suitability for these applications. The use of neutrons as a means to simulate a reactor environment is extremely slow and costly. Charged particle implantation has been used as a rapid, cost effective method that can be tailored to meet specific experimental requirements. We must, however, understand the fundamental differences between neutron and charged particle radiation damage studies before we can draw conclusions from the results.

Electron microscopy has long been a very important tool for the characterisation of radiation damage; used with complimentary techniques the electron microscope and its associated detectors can give insight into the mechanisms of damage like no other instrument. This research aims to gain an understanding of the radiation damage tolerance of structural reactor materials and ideally fill a gap in the knowledge base of using scanning electron microscopy based techniques to characterise this damage.

A novel use of electron backscatter diffraction has been used to reveal trends in radiation damage studies of stainless steel reactor materials, this application of EBSD has not been seen before in the literature. Results from these studies show a clear difference in the tolerance to radiation damage of FCC and BCC crystal structures within the stainless steels. Significant advances have been made in the development of cross sectional sample preparation methods enabling the findings of these studies using EBSD to be validated by traditional transmission electron microscopy techniques.

1 INTRODUCTION

1.1 Background

Radiation damage of materials is of growing significance as we strive for the common goal of providing nuclear power in a safe, economical and long lasting design. The structural materials both in-core and out-of-core must be developed to meet higher performance and reliability criteria for future reactor designs. Current materials must be optimised and future materials developed to achieve these goals. These materials will be subjected to higher temperatures and higher neutron doses in a corrosive environment well beyond those of current reactor designs.

Scientific research of these reactor materials involves finding ways of replicating the radiation environment and characterizing the damage that occurs under these conditions. Radiation-induced segregation, radiation-enhanced diffusion precipitation, interactions, swelling, helium bubble generation through transmutation and interactions between impurity elements and radiation-induced defects are all common problems facing structural reactor materials now and into the future.

As we push the boundaries of what is possible from these reactor materials we must also look into new ways to study the radiation damage effects in a scientific manor in order to fully understand the fundamental damage mechanisms. New ways of characterizing materials are constantly being developed and traditional methods are being improved through advances in instrumentation. Advances in the ways we can simulate the radiation damage are also a major consideration, as neutron irradiation remains a very slow and costly process to achieve the desired dose. Charged particle implantation remains as the most common method of neutron simulation, however, the fundamental differences between accelerated ions and neutrons must first be fully understood before we can draw conclusions from using this method in our research.

1.2 Significance of this Research

Since the 1960s scientists have been using transmission and scanning electron microscopes to study the effects of radiation damage in materials. Electron microscopy remains as the major fundamental research tool in these studies today as it can give visual insight into the mechanisms of damage like no other instrument.

Traditionally the transmission electron microscope (TEM) has been used as a high resolution application for studying very small point defects, defect clusters and loops whereas the scanning electron microscope (SEM) has been used more for bulk techniques such as energy and wavelength dispersive spectroscopy and electron backscatter diffraction (EBSD). In this research we use a novel application of EBSD in the SEM to characterise radiation damage in stainless steels by correlating the loss of diffraction with the defects produced in the steel as a direct result of charged particle implantation. This method has revealed trends in a variety of steels of differing crystal structures with respect to their tolerance to localised ion implantation. Traditionally this technique has only been used to characterise bulk changes in the mechanical properties of these materials as a result of radiation damage. Traditional TEM contrast imaging methods have then been used to quantify these trends observed using this novel application of EBSD.

The significance of these findings has implications for bulk radiation damage studies as the EBSD technique allows for mapping of large areas. Loss of diffraction due to radiation damage is a key area in TEM studies of ceramic materials however the scale at which these materials can be studied in the TEM is of three orders of magnitude smaller than the scale at which an EBSD map can cover.

1.3 Aims and Objectives

This project aims to apply radiation damage to a range of materials relevant to current and future reactor programs. These include current and Generation-4 reactors, reactor core liners, structural materials and any material that may be exposed to a radiation damage environment.

Based around the rapid damage that occurs with charged particle implantation the microstructure of these materials will be examined both before and after irradiation. Instrumentation for this research will focus on microscopy techniques coupled with other complementary macro techniques. The primary focus of this work is to develop electron microscopy techniques and understand grain-boundary interactions and how they relate to the material's tolerance to radiation damage. Ideally we would like to identify a gap in the current knowledge and application of SEM based techniques in this area.

1.4 Statement of Main Findings

The main findings of this research are summarised below:

- The use of backscattered electron channelling contrast as a means of identifying large areas of the stainless steel materials surface in plan view that may have been damaged by ion implantation. AFM results confirm that this result is not simply due to the sputtering away of the highly polished sample surface.
- Subsequent electron backscatter diffraction (EBSD) mapping of these large areas in plan view previously identified by the use of backscattered electron channelling contrast.
- An understanding was gained in EBSD sample preparation conditions for cross sectional samples with minimal edge rounding in the sub 100nm range. These methods were essential for imaging the very shallow radiation damage caused by charged particle implantation at low energies.
- The EBSD mapping revealed a trend for the FCC iron phase to be less tolerant to ion implantation when compared to the BCC iron phase. Indexing of diffraction patterns was in fact not possible for the FCC phase and the BCC phase was only partially indexed. This observation was not found in the literature nor had the use of EBSD for radiation damage studies been utilised

other than for bulk material studies. These observations were later confirmed by preparing cross-sections for subsequent EBSD mapping.

- TEM contrast mechanisms were then used to image the defects present in each phase to confirm the results found using EBSD mapping of the plan view and cross-sectional irradiated steels.

1.5 Publications arising from this Work

Full versions of these publications are attached in the appendices.

J. Davis, K. Short, R. Wuhrer, M. R. Phillips, G. R. Lumpkin and K. R. Whittle. Electron Backscatter Diffraction characterization of Plasma Immersion Ion Implantation effects in Stainless Steel. Nucl. Instrum. Methods Phys. Res., Sect. B, 10.1016/j.nimb.2012.10.007.

J Davis, K Short, R Wuhrer, M Phillips and K Whittle (2012). EBSD Studies of Ion Implanted Duplex Stainless Steel. Microscopy and Microanalysis, 18 Microsc. Microanal. 18 (Suppl 2), 2012 doi:10.1017/S1431927612008586

J Davis, K Short, R Wuhrer, M Phillips and K Whittle (2011). Plasma Immersion Ion Implantation of Stainless Steel 316. Microsc. Microanal. 17 (Suppl. 2), pp 1886-1887 doi:10.1017/S1431927611010300

2 LITERATURE REVIEW: NUCLEAR REACTORS & MATERIALS

2.1 Introduction

This chapter will discuss nuclear reactors, the materials used in their construction now and into the future and the problems associated with using these materials in a radiation damage environment.

2.2 Nuclear Reactors

The first self-sustained controlled nuclear reaction was performed in 1942 at the University of Chicago by a team of scientists [1]. Following this experiment the focus of nuclear technology was in atomic weapons manufacturing during the Second World War. The Atomic Energy Act was established in 1946 to expand the military applications of the new technology and in 1947 the establishment of the first Reactor Safeguards Committee was formed to advise on reactor safety matters [2].

Ever since the first reactor experiment was successful there has been a worldwide focus on nuclear reactor research and development in order to harness the energy available within the atomic nucleus for the generation of power.

Reactors are now used throughout the world as research tools and for the generation of electricity. Power generation plants are extremely large and capable of generating over 1000 megawatts of electricity, which is enough to meet the electrical power needs of a city populated by up to 400,000 people. Figure 2.1 is a schematical diagram of a common pressurised water fission reactor as used in a nuclear power plant today. Nuclear reactors offer a significant advantage over conventional sources of power economically due to their relatively lower environmental impact and vastly larger resources of fuel [3]. For this reason it is very important that research into the construction, safe operation and optimisation of the new generation of nuclear reactors continues.

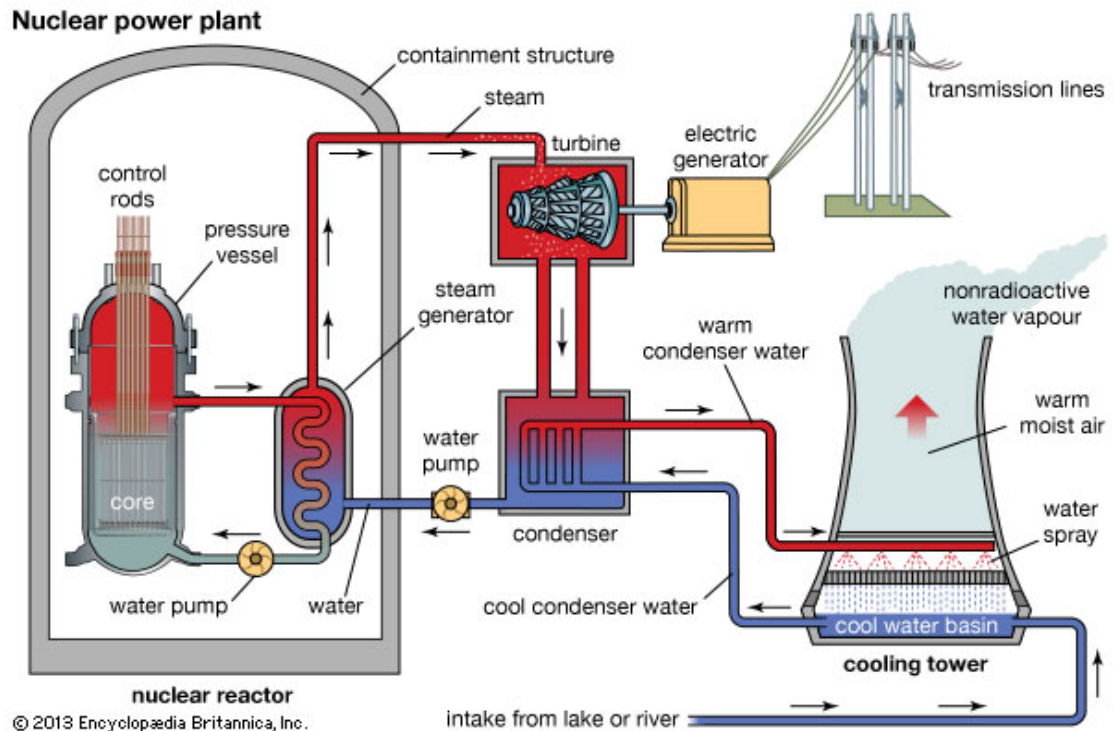


Figure 2-1: Schematic diagram of a nuclear power plant using a pressurised-water reactor, the most common commercially used type of fission power reactor. [Encyclopædia Britannica Inc.]

Fission reactors are the only type of reactors used today for power generation, however, there are many different types of fission reactors in use and there are also several different ways of classification. Fusion reactors or controlled nuclear fusion is purely experimental at this stage and has not been successful in the generation of power, however, there is currently a major joint project underway called the International Thermonuclear Experimental Reactor (ITER) which has the aim of commercialising nuclear fusion as a means to generate power. A schematic diagram of the ITER tokamak fusion reactor design is shown in figure 2.2. This thesis will not deal with the topic of nuclear fusion.

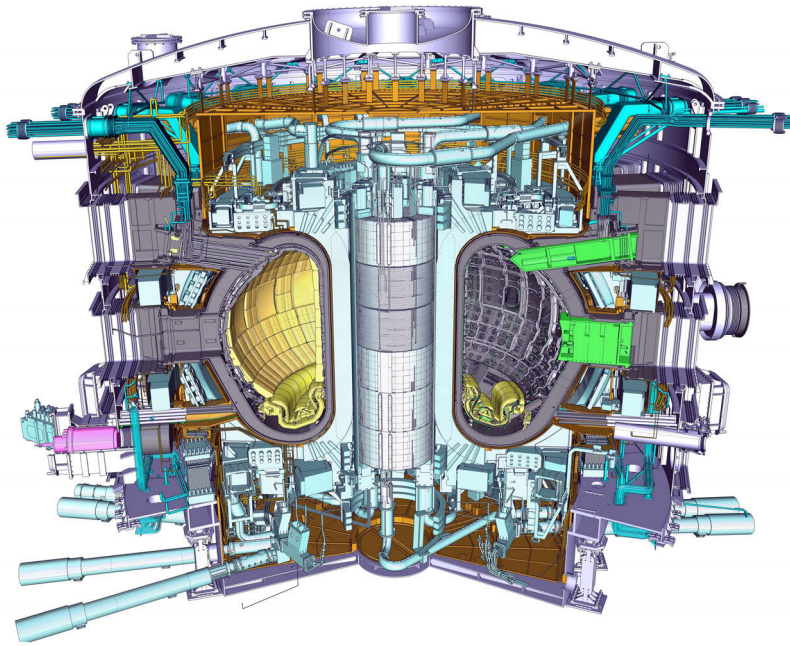


Figure 2-2: The ITER tokamak reactor design. The fuel is contained in a doughnut-shaped vessel and heated to 10 times the temperature of the sun's core, forming a plasma. [iter.org]

In nuclear fission we can break down the type of reactor into two main groups, by the characteristic neutron energy used for fission as: thermal reactors; and fast neutron reactors. Table 1. shows the nuclear fission reactors; both commercially in use now and at the prototype stage, with a description of the technology used to generate maintain the reaction and generate power [6].

Table 2-1: Table showing commercial nuclear reactors currently in use and proposed designs [10 - 33].

Reactor Type	Description	Fuel	Coolant	Moderator
Pressurised Water Reactor (PWR)	The most commonly used commercial power reactor. A thermal neutron reactor design.	Enriched UO ₂	Water	Water
Boiling Water Reactor (BWR)	Similar to a PWR without the steam generator. The second most common thermal neutron reactor design.	Enriched UO ₂	Water	Water
Pressurised Heavy Water Reactor (PHWR)	A thermal neutron reactor with multiple pressure tubes which can be re-fueled whilst running at full power.	UO ₂	Heavy Water	Heavy Water
Gas-cooled Reactor (AGR & Magnox)	A thermal neutron reactor design with high thermal efficiency as they run at higher temperatures.	U metal & Enriched UO ₂	Carbon Dioxide	Graphite
Light Water Graphite Reactor (RBMK & EGP)	Similar to PHWR in design however safety is a concern with this design. Very few remain in service.	Enriched UO ₂	Water	Graphite
Fast Neutron Reactor (FBR)	Known as a 'breeder' as this reactor can produce more fuel than it consumes.	PuO ₂ and UO ₂	Liquid Sodium	None
Pebble-bed reactors (PBR)	A prototype reactor not currently commercially used.	Tristructural-isotropic	Non-reactive Gases	Graphite
Molten salt reactors	Another prototype reactor not currently commercially used.	UF ₄ in Molten Salt	Molten Salt	Graphite

2.3 Current Reactor Materials

The selection of materials in reactors is varied depending on the application or part of the reactor in which the material will be utilised. A modern reactor contains three physical barriers between the radioactive fuel and the exterior of the reactor. Fuel cladding, reactor pressure vessel and the concrete containment are the three main barriers present with only the first two mentioned being exposed to neutrons [4]. In this chapter we will discuss only those materials that are subject to neutron irradiation damage under normal operation.

There are many factors that influence the selection of materials for intended exposure to neutron irradiation damage. These include mechanical strength, ductility, stability, neutron absorbing characteristics and susceptibility to induced radioactivity. The materials used in these conditions will have limitations within which they perform well, but beyond these limitations the materials may not be considered for use [7].

The materials used as current reactor materials will have undergone evaluations based on their intended application and only those materials most promising are selected. Simulated service tests are then carried out, however, these cannot give a true indication of the performance under actual service; since they are often accelerated tests. It is the understanding of the specific environment and damage kinetics under which the material will be operating that allows the engineer to determine whether the material will have a satisfactory service life [7].

Mechanical strength and ductility are not strictly nuclear factors in terms of material selection however these properties can be affected in a neutron irradiation environment where radiation damage occurs. This is why it is critical to understand the effect of neutron absorption and induced radioactivity for any chosen reactor material [8]. Radiation damage of materials is discussed in more detail in Chapter 3.

Current metallic structural reactor materials in use, subject to radiation damage include [9]:

- austenitic
- ferritic
- advanced ferritic-martensitic steels
- zirconium alloys
- vanadium alloys
- nickel based alloys.

These materials are found in the fuel rods, reactor pressure vessel or pressure tubes and as part of the general reactor structure.

2.4 New Reactor Materials

The majority of the current reactors in service are Generation-2 category; Generation-3 reactors are simply improved versions of Gen-2 in terms of safety, fuel technology, and thermal efficiency. There are only a handful of Generation-3 reactors currently in service with several designs completed but not yet built.

Generation-4 (Gen-4) reactors are considered the reactors of the future and are in the advanced stages of commercialization. It is the Gen-4 reactor materials that are considered to be the “new materials” for reactor design in that they are not yet fully qualified by engineering test programs. These materials will have higher demands of irradiation and high temperature tolerance placed upon them by the Gen-4 reactor design service environment, which pose significant challenges to materials selection and qualification [10].

Materials of interest for both nuclear fission and fusion reactors include oxide dispersed steels, refractory metals and alloys, silicon carbides and tungsten, however, some of these are solely intended as shielding materials for fusion reactors, which is beyond the scope of this research [9]. These existing reactor materials are also being considered for Gen-4 applications with improvements being made on the already extensive knowledge base, therefore we can not always call them “new materials” as they have long been used, however, the properties of these materials are being improved for Gen-4 applications.

New reactor materials are selected using the same processes as mentioned above with an emphasis on improving the neutron damage tolerance whilst not increasing the material’s susceptibility to induced radioactivity. Mechanical strength and ductility requirements must be met for the material’s intended purpose within the reactor. We can now look at these new and improved materials individually in more depth and see how advances are being made in terms of reactor material performance.

ODS Steels

Oxide dispersed steels (ODS) typically consist of nanoclusters of oxide-like particles within the steel alloy. The benefit is that these particles can hinder dislocation movement and become sinks for radiation-induced defects [10]. Research has shown that irradiated ODS materials at elevated temperatures were not affected by radiation hardening as no increase in strain (or ductility) was observed [11].

These properties make ODS steels a good candidate for fuel cladding in sodium cooled fast reactors. Manufacturing process development is the main hurdle to be overcome when considering using these materials for this purpose, as long thin walled cladding is

required on large production scales. It is the desirable properties in a radiation damage context that make this production difficult. These include the elongated fine grains parallel to the rolling direction. Grain morphology has been modified by using different steel alloys however most work is still being done on tensile and creep rupture strengths in hoop directions and irradiation performance [19]. ODS steels are essentially a new and improved version of ferritic steels with the drawbacks of poor weldability and a powder metallurgy production route.

Refractory Metals

Refractory metals have also been considered for use in Gen-4 reactors due to their extremely high melting temperatures ($>2000^{\circ}\text{C}$) with good creep resistance and swelling resistance at these high temperatures. However in 2008 K.L. Murty et al. [10] concluded that poor oxidation resistance; low temperature radiation embrittlement and fabrication difficulties meant that refractory metals are not being widely considered for Gen-4 reactor applications. K.J. Leonard et al. [18] published further on refractory materials in 2012 stating that in radiation environments the materials are not recommended at temperatures $<0.3 T_m$ (where T_m is the absolute melting temperature). However, new research particularly on molybdenum and its alloys has shown that by controlling interstitial element contamination levels, grain size and morphology, coupled with oxide dispersion strengthening improvements to the low temperature irradiation properties of refractory metals could be achieved.

Nickel Alloys

Nickel base alloys have a history of use in high temperature applications and therefore many studies have been done to test their suitability for use in Gen-4 reactors. K.L. Murty et al. [10] noted the main issue with Ni alloys was radiation embrittlement despite them having good creep rupture properties and high temperature strength. Nimonic alloy PE16 and Inconel 706 were investigated for fast breeder reactor core applications, Nimonic alloy PE16 was also successfully used for fuel element cladding and subassembly wrappers in the United Kingdom, and Inconel 706 was utilised for cladding in France [20]. Rowcliffe et al. and Angeliu et al. [21, 22] have reviewed later studies on the effects of radiation on the microstructure and mechanical properties of nickel-based alloys for Gen-4 applications and the Prometheus space reactor. Nickel-based alloys are also being considered for molten salt reactors due to their resistance to

corrosion by molten fluoride salts and high-temperature creep strength. Intergranular attack by the fission product tellurium and irradiation embrittlement due to helium production are potentially limiting factors for this application [23]. Work has also been done on a solid solution strengthened Ni-base superalloy (Alloy 617) in consideration for heat exchanger applications in next generation nuclear plants that incorporate the very high temperature reactor concept [20].

Zirconium Alloys

Zirconium alloys are currently used in light and heavy water nuclear reactor cores as structural components because of their low capture cross section to thermal neutrons and their good corrosion resistance, coupled with acceptable mechanical properties. Gen-4 reactors however have a more stringent set of requirements for their structural materials of higher temperature and stress. These requirements cannot be met by zirconium alloys due to their increased susceptibility to hydrogen embrittlement as a result of hydride formation, allotropic phase changes at higher temperatures, poor creep properties and oxidation [24].

At low temperature Gen-4 reactor design such as super critical water-cooled reactors there may be consideration for the use of some high performance zirconium alloys [10].

Silicon Carbide

Silicon carbide has historically been used in high temperature gas cooled reactors as the micro pressure vessel in the fuels, these are known as TRI-ISotropic (TRISO) fuels. Current development focuses around its composite form for applications in gas cooled and light water fission reactors and advanced sodium fast, advanced liquid salt-cooled reactors. Another key area of research is in shielding or thermal insulating applications for fusion reactors [25].

Rare Earth Alloys

Vanadium alloys and Tungsten are materials solely being considered for fusion reactors and therefore is worth mentioning as irradiation damage resistant alloys but are not currently being considered for fission applications.

Low-Activation and Advanced Steels

Finally we can discuss austenitic, ferritic, advanced ferritic-martensitic steels. These materials along with oxide-dispersed steels (previously mentioned) have significance as they have been used as experimental materials in this research.

We can start by discussing austenitic stainless steels which have been used extensively in current boiling water and pressurised water reactors (BWR and PWR) as structural materials both in-core and surrounding structures. Austenitic stainless steels have also been considered for advanced reactor technologies including fast breeder reactors and applications for fusion. With regard to these advanced technologies modified versions have been developed to improve the performance of the standard commercial stainless steels to meet performance criteria for radiation resistance in specific reactor environments [26].

Limitations of austenitic steels are primarily neutron-induced void swelling in relatively large amounts even with moderate doses. W.R. Corwin et al. [28] has shown that the extent of swelling is much higher for many austenitic steels when compared to ferritic and advanced ferritic-martensitic steels. Low thermal conductivity is also a factor that may affect reactor efficiency and radiation-induced segregation coupled with phase stability issues is the other main concerns [10].

T.R. Allen et al. [29] noted that chromium depletion at grain boundaries in austenitic steels is also an issue specifically in water or lead-alloy cooled systems as inter-granular corrosion may occur.

As mentioned above, ferritic steels offer some improvements over austenitic steels with regard to void swelling due to neutrons in a radiation environment. Due to better swelling performance in the fast neutron spectrum ferritic steels have been considered for the fast reactor industry since the 1970s and extensive research has been done on the application of ferritic steels for nuclear core components [30].

The high temperature tolerance of ferritic steels has also been dramatically improved with the development of oxide-dispersed steels. With regard to the void swelling issues there have been a series of resistant commercial ferritic steels developed. The ferritic

steel lattice is well understood and the mechanisms in which point defects interact with dislocations for microstructural stability have been extensively investigated. For fast reactor core material the 9-12% chromium ferritic-martensitic steels have been isolated as the best candidates due to their superior void swelling resistance and tolerance to radiation induced embrittlement [31].

3 Literature Review RADIATION DAMAGE

3.1 Introduction

The design of large nuclear power plants is extremely complex and requires the expertise of a range of disciplines. The reactor core is the responsibility of nuclear engineers and must be designed with numerous constraints on how the reactor is operated. These restraints include system performance in terms of reliability and economic performance within specific safety criteria [3].

The focus of this research is the characterization of neutron irradiation damage, in particular, to the engineering structural materials (modern metal alloys) used in fission reactors. A modern reactor contains three physical barriers between the radioactive fuel and the exterior of the reactor. Fuel cladding, reactor pressure vessel and the concrete containment are the three main barriers present with only the first two mentioned being metallic [4] and exposed to neutrons. Historically commercial operation of nuclear reactors in 32 countries worldwide has seen only three major accidents relating to the release of radioactive material into the environment, radiation damage studies of reactor structural materials are therefore critical for the continued safe operation and design of nuclear power reactors.

3.2 Types of Radiation Damage

Chapter 2 has briefly discussed radiation damage mechanisms that affect specific materials currently being used or considered for use as reactor materials. In this chapter we will look at some of the fundamentals of radiation damage with respect to dose and temperature. The detailed behaviour of different classes of materials ranging from polycrystalline metallic matrix to ceramic glasses is obviously very different, so particular focus will be on metallic materials used in the stress-bearing structure of fission reactors.

Components of nuclear reactors are bombarded with a spectrum of fast and intermediate neutrons at elevated temperatures during fission reactions. It is the “fast” neutrons (0.1 –

10MeV) that are a significant cause of damage to the metallic structures crystal lattice. The damage mechanism is the displacement of atoms from their stable lattice positions as a result of elastic collisions with neutrons. For displacement to occur the transferred energy in the collision must exceed the displacement energy threshold value for the particular material being bombarded which is comparatively small at around 20 – 40 eV for metals [5].

Looking more closely at radiation damage mechanisms for neutrons in the 0.1-10MeV energy range we can conclude there are at least five main ways in which the structural materials within a nuclear reactor may be compromised. These include radiation hardening and embrittlement, phase instabilities from radiation induced precipitation, irradiation creep, volumetric swelling from void formation and high temperature helium embrittlement [12]. These mechanisms occur at different temperatures and damage levels. At low temperatures radiation hardening occurs predominantly in BCC metals which results in a loss of fracture toughness. This is due to dislocation motion being hindered by the radiation induced defect clusters. Since this occurs at relatively low doses (0.001 to 0.1dpa) it often defines the operating temperature limit at the lower scale for the structural materials which are being exposed to neutrons [13].

There are three distinct damage mechanisms which occur at intermediate temperatures for doses above approximately 1 to 10 dpa. The first being segregation and precipitation as a result of radiation. This can lead to localised corrosion and a reduction in the material's localised mechanical properties as a result of grain boundary embrittlement and void swelling from the accumulation of vacancies which ultimately leads to unacceptable amounts of volume expansion [14 - 15]. Radiation induced creep may also result which may lead to anisotropic growth creating expansion along high stress directions or specific crystallographic directions [15 - 16].

Finally at very high temperatures and under an applied mechanical stress the main mechanism leading to failure in structural materials is helium produced by transmutation reactions which may migrate to grain boundaries and form cavities. This ultimately leads to swelling and intergranular fracture and therefore defines the maximum allowable operating temperature limit for the structural materials being exposed to neutrons [17].

Expanding further on the significance of transmutation reactions, these reactions produce helium in the range of <1 to 1000 atomic parts depending on the specific alloy in question and the neutron fluence it is exposed to. Transmutation reactions also produce hydrogen in even higher amounts, however it is the helium that is essentially insoluble in solids which creates the radiation damage. As mentioned above the helium precipitates to form bubbles that may become nucleation sites for larger voids ultimately migrating to grain boundaries. Therefore helium generation is the mechanism for stress driven growth of grain boundary creep cavities that ultimately lead to failure in the material [17][34].

3.3 Radiation Damage Characterization

We have discussed the mechanisms for radiation damage and briefly discussed some of the issues facing specific materials being used for or being proposed for use in reactor design.

Researchers have many methods available to scientifically test and study these materials to determine whether they are suitable for use in reactors. This chapter will cover some of the most common methods as found in the literature.

To characterise the damage a material receives in a reactor or radiation environment researchers must first look at ways to perform or simulate this neutron damage. In chapter 4 we will discuss the method used in this research, which was chosen, based on the instrumentation available and timeline required for the completion of this project. In this chapter we will discuss the methods as found in the literature for performing or simulating the radiation damage in materials, we will then discuss the most common methods used to characterise this damage.

The two methods used to perform radiation damage on a material specimen are neutron and ion irradiations; we can start by talking about neutrons. Neutron irradiation involves placing the material in a nuclear reactor for a given period of time until the dose required for the experiment has been obtained, temperatures may also be controlled in some cases using this method. The main problem with using neutrons is the experiment

is very slow, irradiation rates are very low and the dose required may take several years to achieve. The extended time to perform these experiments also makes it very expensive to perform [32]. The next hurdle to overcome with neutron-irradiated samples is the activation of the material. Once a sample is removed from the reactor, the material itself may be radioactive due to transmutation reactions that occur when the neutrons collide with certain elements within the material. This activation of the material means that special handling is required, typically hot cells and special instrumentation is required to examine the radioactive materials in a safe manor. In some cases if the radioactivity of the irradiated samples it too great then handling and examination is not possible and the material must be left for a long time until the majority of the activity has decayed [33].

Charged particle or ion beam irradiation has been used as a way of understanding radiation damage for over 60 years, with the earliest works by Kinchin and Pease dating back to the mid 1950s. Ion beam irradiations allow for more rapid and therefore lower cost experiments with rates of approximately 10 to 1000 times faster than that of neutrons depending on the mass of the charged particle. Higher rates are possible however the high temperature generated can add too much complexity to data interpretation [32]. Other than the rapid speed of irradiations the other main benefit over neutrons is the flexibility that can be tailored into the experimental design. Parameters such as dose, dose rate, temperature, chemical and mechanical environment can all be controlled [34].

In the literature many studies have been done comparing the pros and cons of neutron versus charged particle irradiations. The main limitations for charged particle irradiation are sample sizes, volumes must be must be kept small which may lead to disproportionate surface effects. High irradiation rates can affect some rate-dependent reaction pathways when replicating lower damage rates in a neutron environment. The mass and energy of the ion can vary the ballistic event within the target material making comparison with neutron irradiations more difficult to interpret [32 - 34].

Fundamentally there is a major difference in the way ions and neutrons are produced. This is important as the energy of the particles is vastly different between the two systems. Charged particles are produced in an accelerator and therefore every particle

typically has the same energy. Neutrons, which are produced in a reactor, will have an energy spread over several orders of magnitude depending on where exactly the sample is placed within the reactor vessel, see figure 3.1. To complicate things even further the energy of the neutrons will vary greatly between different reactors [55].

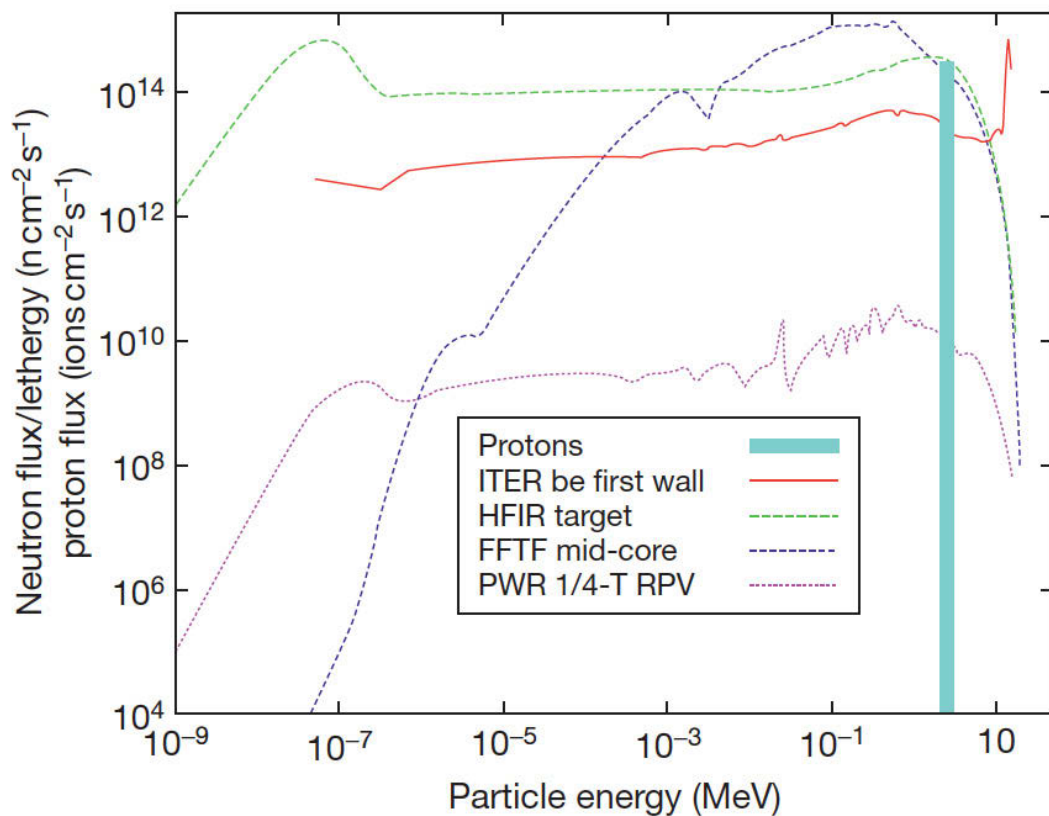


Figure 3-1: The energy spectrum for neutrons taken from a variety of reactor types and a monoenergetic proton beam. Reproduced from Stoller, R. E.; Greenwood, L. R. J. Nucl. Mater. 1999, 271–272, 57–62.

Depth of penetration also varies greatly when comparing charged particles to neutrons. Charged particles lose energy more rapidly as a result of electronic energy loss as the particle interacts with the metallic substrate. Neutrons being electrically neutral can penetrate very large distances and produce spatially flat damage profiles. Work by Serruys et al. [38] has shown that the dose rate variation between charged particles and neutrons is significant as ion beams produce significantly larger dose rates compared to neutrons. In addition to this the energy distribution of the primary knock on atoms (PKA) leads to a steeper production of displacements for neutron irradiations. Figure 3.2. illustrates this by showing the PKA damage fraction produced as a function of PKA

energy for three neutron spectra compared with ion-beams (20MeV and 10MeV heavy ions).

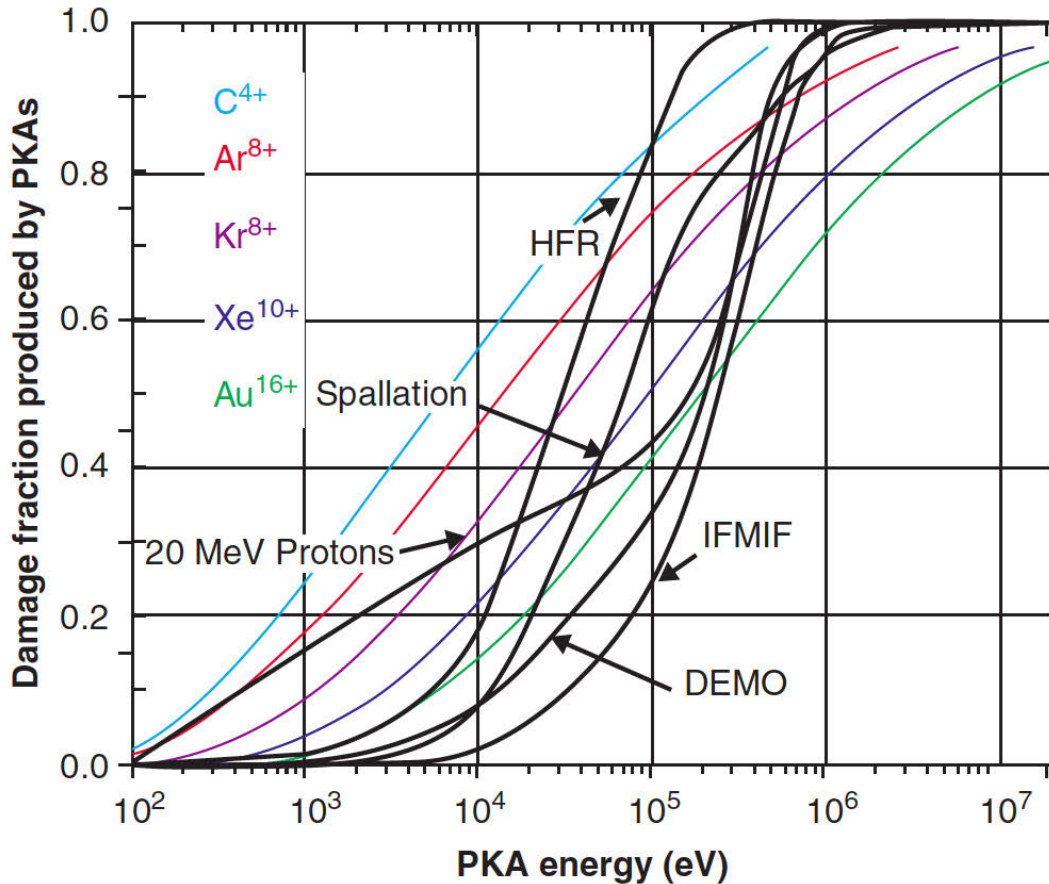


Figure 3-2: Primary knock-on atom (PKA) damage fraction produced as a function of PKA energy for three neutron spectra (DEMO, IFMIF, and HFR) compared with ion-beams (20MeV and 10MeV heavy ions). Serruys et al. (2008) [38].

Work by Kulcinski et al. [56] has shown that for comparable neutron and charged particle energies, the charged particles will cause over 100 times more damage per unit of fluence at the sample surface than neutrons.

We have discussed transmutation reactions that occur with neutron irradiations, ion irradiation produces little to no residual activity allowing us to examine the samples as soon as the irradiation has been performed. However, we must also consider how charged particle irradiation might be able to simulate these transmutation reactions if we are to fully understand any material in a neutron environment.

As previously mentioned, helium and hydrogen are produced from transmutation reactions as a result of fast neutron collisions with the nucleus of certain elements within the material. The most significant with respect to radiation damage is the production of helium by transmutation of nickel or boron. Helium and hydrogen arising from transmutation reactions will interact in ways that cannot be reproduced experimentally using charged particle irradiations which is another limitation of this technique when compared to neutrons. Hydrogen formation is more typically found in a fusion neutron spectrum or as a consequence of the electrolysis of water in a fission reactor, not as a result of transmutation [32].

In the literature we can find many examples of how scientists have tried to overcome this barrier with respect to the simulation of transmutation reactions. The use of simultaneous multiple beam ion accelerators is the most common method as it allows the implantation of both helium and hydrogen ions at the same time and or a heavy ion beam may also be employed for ballistic damage. Tanaka et al. [35] has shown that with simultaneous ion irradiation important synergies may develop which may change with dose leading to added complexity in experimental interpretation.

Multi beam irradiations, however, cannot be seen as a completely true representation of neutron irradiations. Kumar [36] showed that dual beam irradiations previously undertaken by Levy et al. [37] for a fusion study contained artifacts which were not representative in a neutron fusion environment citing interactions with self ion generated interstitials and helium as the artifact.

We have discussed methods for performing radiation damage studies with neutrons or charged particles, now we discuss methods to characterise this radiation damage as found in the literature.

As previously mentioned there are many factors that influence the selection of materials for intended exposure to radiation damage. These include mechanical strength, ductility, stability, neutron absorbing characteristics and susceptibility to induced radioactivity. Once ion implantation or neutron irradiation has been performed on a material it is these properties that can be examined to evaluate the materials performance. These properties which are mostly determined by mechanical testing set a benchmark for the material's

ultimate suitability for use in a reactor; however research is often more concentrated on the fundamental radiation damage mechanisms which occur during or after radiation damage. It is these fundamental damage mechanism studies that are the primary focus of this thesis. In the literature electron microscopy has been found to be a very widely used method for material characterization in radiation damage studies. Coupled with some other techniques electron microscopy is a very powerful means of seeing changes in a material post irradiation.

The two main types of electron microscopy are scanning electron microscopy (SEM) and transmission electron microscopy (TEM). These names describe the basic microscope operation and design however there are many different detectors which may be fitted to both these instruments which can expand their characterization capabilities. Details of these instruments and associated detectors are covered further in chapter 5.

Looking at how the TEM has been used in the literature we can see that this instrument has been used to study a material's microstructure post radiation damage since the 1960s and even longer for general microstructural studies. A TEM can give visual insight into the mechanisms of damage like no other instrument. It is a complimentary technique that like many other macroscopic techniques does have its limitations. These include sample size, samples must be very small and thin which can lead to artefacts due to the size of the sample not being representative of the bulk material in question. The resolution of the TEM is very high, less than 1nm in an ideal sample although it does have its limits that may affect the ability to see very small defect clusters. Sample preparation is critical and will also influence what is seen in the instrument [39].

Specific techniques employed by scientists when using a TEM to study radiation damage in materials both pre and post irradiation in the literature is an extremely large and complex area of research, we can only begin to touch on some of the methods used in this review.

The first technique discussed will be contrast mechanisms, which are the most commonly used methods in radiation damage studies. These contrast mechanisms arise from local changes in diffracting conditions caused by the effect on the defect strain field. There are a range of contrast mechanisms that can be studied in the TEM, these

diffraction conditions can be broken down into the following: two beam dynamical conditions, bright field kinematical, weak beam dark field and phase contrast [39]. C.A. English [40] used a series of TEM contrast images to show the irradiation damage structure induced in pure metals and alloys by low-dose fission neutron irradiation at a range of temperatures. The use of this technique was able to show the different damage mechanisms and amount of damage which occurs between the different crystal structures present in the pure metals and alloys.

Characterization of dislocation loops and stacking fault tetrahedra (SFT) is another key area of research where TEM may be utilised. Defects in the 1 nm range are visible using the contrast mechanisms mentioned above, however to fully characterise these defects in the TEM we are limited by the resolution of the instrument as typically defects less than 5 nm are difficult. Full characterisation can be broken down into two main areas. The first is to distinguish the defects between dislocation loops, SFTs and small precipitates then defining the nature of clusters as vacancy or interstitial. The next area is loop Burgers vectors (direction) habit planes and shapes, measuring cluster sizes and distributions and the determination of number densities [39]. Z. Yao and M. Hernández-Mayoral et al. [44] performed some interesting characterization of dislocation loops and Burgers vectors using an in-situ irradiation facility at Argonne National Laboratory in the USA. This facility combines electron microscopy with in situ ion irradiation at controlled sample temperatures which allows unique dynamic observations of defect formation, mobilities, and interactions during irradiation. This study of radiation damage in Fe and Fe–Cr alloys under heavy-ion irradiation showed that dislocation loops first appeared at doses between 10^{16} and 10^{17} ions m^{-2} in all materials and the number of loops retained was strongly dependent on the foil orientation in Fe, but less so in Fe–Cr alloys. This was reported as being due to the lower loop mobility in Fe–Cr alloys as a result of pinning by Cr atoms. The reduced loop loss was due to the higher loop number densities in Fe–Cr alloys compared with pure Fe.

Another key area of research performed in the TEM is characterisation of voids and bubbles as a result of radiation damage. Voids in the range of 5nm or larger may be visible using the contrast mechanisms mentioned above, this is achieved with the use of certain sample tilts and a underfocus, overfocus condition which gives rise to white dots surrounded by black fringes or vice versa depending on whether it is a void or a bubble

you are imaging. Measuring the size of these voids or cavities can be achieved by applying calculations to these images however anything less than 2nm cannot be determined accurately [39]. Work by D. S. Gelles [43] used this through focus technique to characterise two grades of martensitic commercial steels alongside an oxide dispersion strengthened ferritic alloy post irradiation.

Finally, complex microstructure characterisation of line dislocations and larger dislocation loops associated with radiation damage in a material is another important area of research using the TEM and techniques for studying the fine structure of cascades can also be employed [39]. Work by M.L. Jenkins et al. [45 – 47] has shown that a cascade structure may be directly revealed if certain conditions are met to image the disordered zones using superlattice dark-field reflections.

Scanning electron microscopy (SEM) is the other instrument that has been used in the literature to study radiation damage of materials. We can look at some examples of how this instrument has been used below.

SEM has a lower resolution than the TEM although modern field emission gun based SEMs have come a long way to closing this gap in spatial resolution. The SEM is considered a complimentary technique to TEM, not a competitor due to its ability to study surface effects or morphology and look at rather large samples without the need for extensive sample preparation. Due to this resolution limit the SEM is more commonly used for bulk techniques rather than trying to image very small defects in the material. These bulk techniques include wavelength and energy dispersive spectroscopy (WDS, EDS) as a means of studying bulk chemical compositions and electron backscatter diffraction (EBSD) which is typically used to study any changes in a material's mechanical property at a microstructural level as a result of radiation damage.

J Chen et al. [49] used the SEM to show surface morphology changes in fractured 304 stainless steel samples which had been irradiated at low temperature ($\leq 250^{\circ}\text{C}$) with 800 MeV protons to a fluence of 3×10^{25} p/m², corresponding to a displacement dose of about 8.5 dpa. This work was able to highlight how the fracture mode changed from typical ductile to partial intergranular brittle after irradiation.

Energy dispersive spectroscopy (EDS) or wavelength dispersive spectroscopy (WDS) in the SEM is commonly used in radiation damage studies where corrosion is of interest such as materials for fuel claddings and the core components in supercritical water-cooled reactors (SCWRs). M Fulger et al. [50] has used this technique to study corrosion behavior of Incoloy 800 under simulated supercritical water conditions. Results made from this study using EDS in the SEM were able to show how the elemental concentration distribution coupled with the morphology of the corrosion samples formed two distinct layers. An outer iron enriched layer and an inner layer enriched with chromium and nickel oxides. These layers showed differing degrees of porosity for the different exposure temperatures that ultimately lead to a higher degree of porosity and therefore lower corrosion resistance for the samples exposed at higher temperatures.

Xianglin Wu et al. [48] has used EBSD in an SEM as a means of studying flow localization in candidate structural materials for Gen-4 reactor systems. This 316L stainless steel is sensitive to irradiation damage in the temperature range of 150–400°C even at very low doses causing a severe loss of ductility. EBSD has been used to determine the mechanism for which this loss of ductility occurs under these conditions.

An SEM fitted with a scanning transmission electron (STEM) detector may be used with good results for high-resolution imaging if the funds for a dedicated TEM are not available, however the sample preparation requirements for this are the same high standard as required for the TEM.

It should also be noted that EDS is also an important analysis technique that may be utilised in the TEM. The main benefit of performing this type of analysis in the TEM is the very small probe size and x-ray interaction volume it creates. EA. Kenik [41] successfully used this technique to show how radiation-induced grain boundary segregation differs in two grades of 304 stainless steel after neutron irradiation. It was shown that certain elements would segregate giving rise to higher intergranular stress corrosion cracking tolerance for one grade leading to a significant affect on the material's mechanical properties. Further work using x-ray analysis in the TEM by R.D. Carter et al. [42] was undertaken to determine the origins of irradiation-assisted stress corrosion cracking in austenitic alloys in light water reactors. This work was performed

using a proton beam instead of neutrons, however, similar conclusions were made with respect to the segregation of certain elements at the grain boundaries.

4 EXPERIMENTAL: RADIATION DAMAGE & TESTING METHODS

4.1 Introduction

The study of nuclear reactor materials, both existing and proposed, is important to ensure their reliability and integrity when exposed to radiation damage during their service life. By understanding the damage mechanisms of such materials, existing materials can be optimised and new improved materials can be developed.

This chapter of the thesis will cover the instrumentation and methods used to study the effects of radiation damage on materials.

4.2 Ion Implantation Versus Neutron Irradiation

The simulation of a neutron irradiation environment using ion implantation has been chosen as an alternative to reactor based neutron irradiation, without activating the material. Helium ions can damage regions in a metal alloy's microstructure primarily through atomic displacement. Point defects are formed and when these point defects are mobile they can cluster forming point defect agglomerates and voids [51]. The implanted helium ions may reside in these voids and change their time dependent growth dynamics similar to those observed in fast neutron radiation damage studies [52]. Farrell [53] has shown the importance of helium gas (predominantly formed by nuclear transmutations) in radiation damage studies promoting the formation of cavities and enhancing the dislocation structure.

We have discussed the fundamental differences of charged particle implantation versus neutron irradiation in chapter 3.2 of the literature review. For this project the main reason of using ion implantation instead of neutron irradiation is the time requirement to complete this work and to a slightly lesser extent, gaining access to a neutron source is not possible. Required dose rates in ion implanted samples can be achieved in a fraction of the time when compared to neutrons. In fact the time required for an equivalent neutron study would run well beyond the time required to complete this thesis. Another

main factor is that ion implanted samples do not become radioactive, as would be the case if we had used neutron irradiation. Active samples require long periods of time to deactivate to a level where they can be handled safely. Even once the samples have had time to become less active they would still require very special equipment, instrumentation and safety procedures for their characterisation, which would be beyond the timeline and scope of this project.

4.3 Plasma Immersion Ion Implantation (PI³)

Plasma immersion ion implantation (PI³) is a method designed to implant large areas of samples simultaneously, to very high fluences, with a small energy variation. A photograph of the PI³ instrument used in these experiments is shown in figure 4.1. It originally grew out of an ANSTO project in the 1980s investigating the fundamental properties of plasmas relevant for use in nuclear fusion. The process involves forming an ionised plasma at a controlled temperature with radio frequency (RF) excitation. Ion implantation occurs when the positive ions from the plasma are accelerated towards all exposed surfaces by pulsing a high negative voltage on the sample, figure 4.2 shows a schematic diagram of this process. It has previously been used for surface hardening and improving corrosion properties of metals. In this work the ion implantation technique is being utilised to simulate some of the effects from a neutron irradiation environment. The ability to implant ions with low energy at a high flux is very useful for these radiation damage studies when the PI³ ion implantation is complimented with the use of the STAR accelerator's high-energy low flux ion implantation.

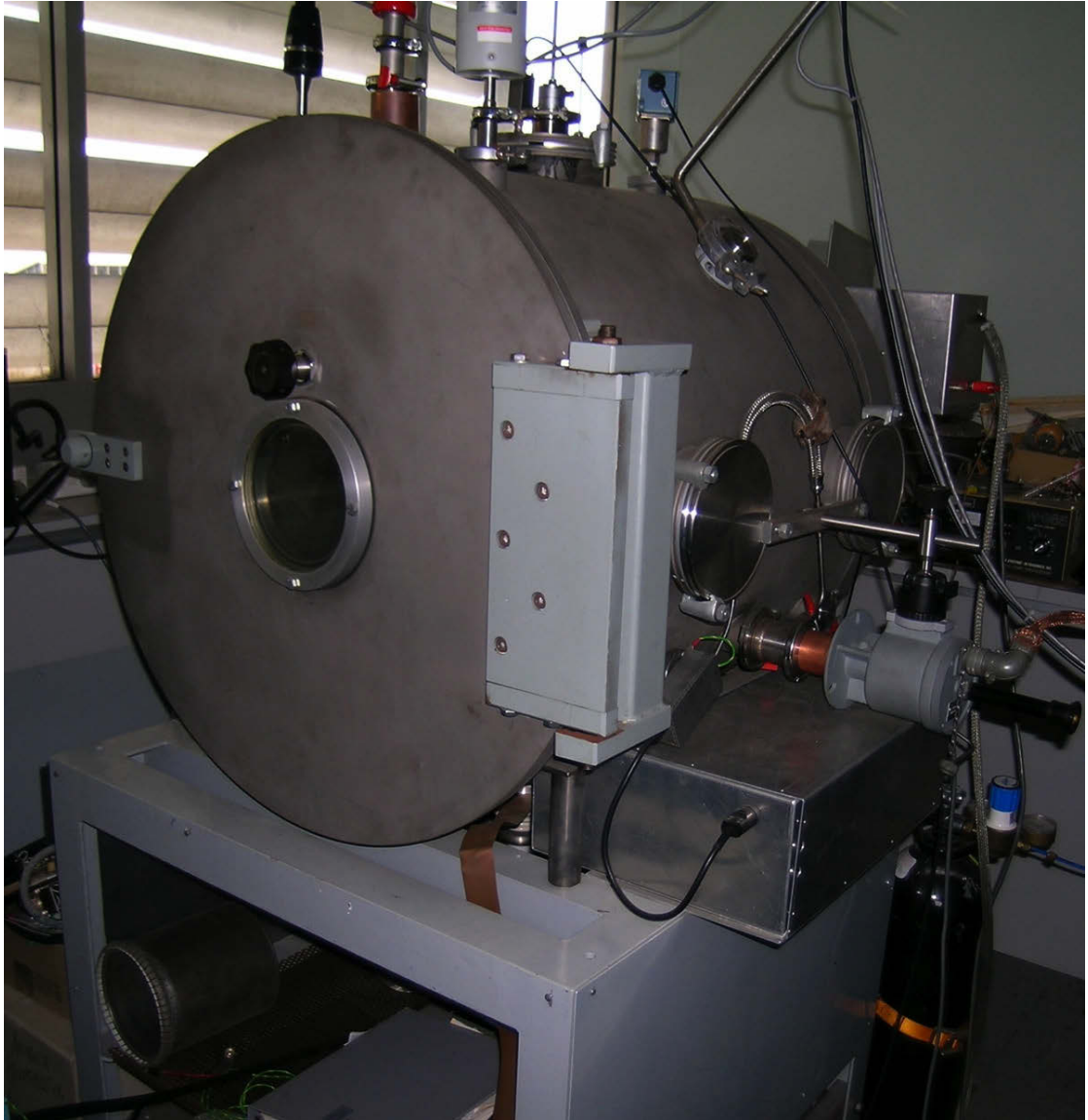


Figure 4-1: Plasma immersion ion implantation (PI³) instrument used for this project, which is housed at the Institute of Materials Engineering, ANSTO.

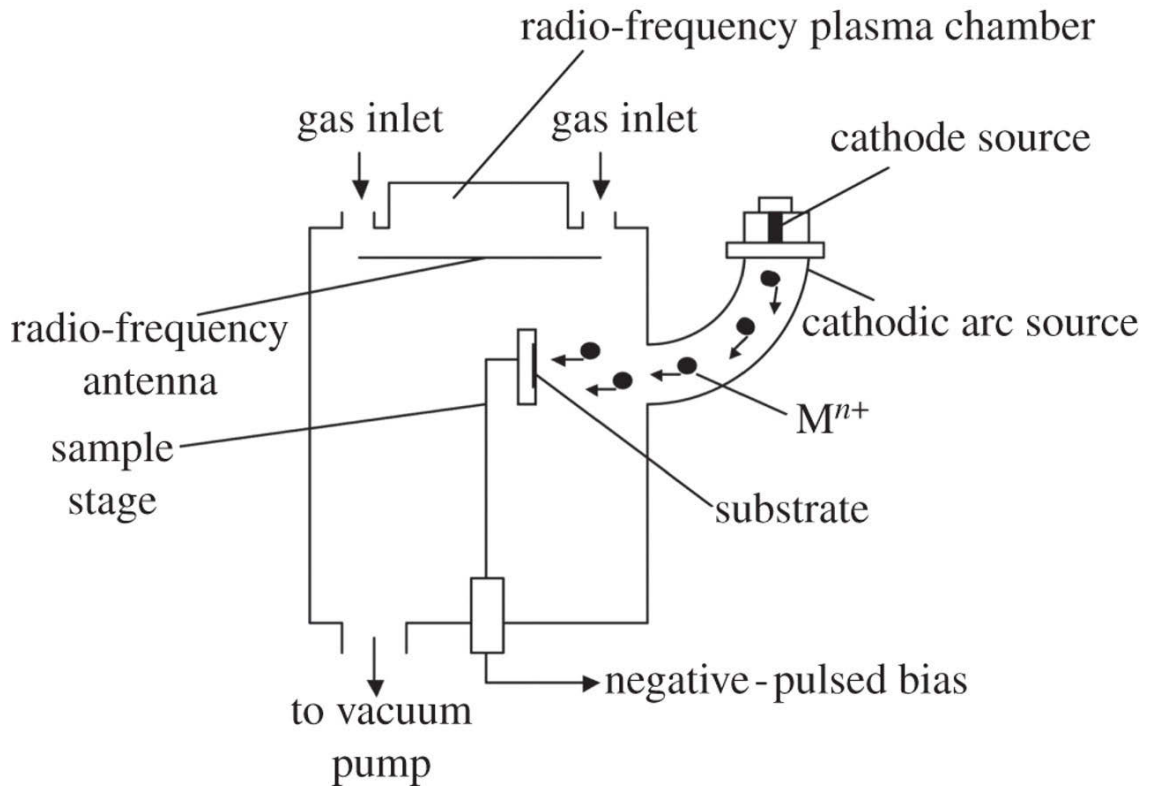


Figure 4-2: Schematic diagram showing the plasma immersion ion implantation (PI³) process [54].

4.4 Small Tandem for Applied Research (STAR) Accelerator

Fully commissioned in 2004, STAR is a two million volt tandem designed specifically with state-of-the-art capability for dual functionality, providing both ion beam analysis and high-throughput and high-precision accelerator mass spectrometry (AMS) radiocarbon analysis. In these experiments we are using the ion accelerator to bombard materials with ions to simulate some of the effects from a neutron irradiation environment. The STAR accelerator can produce a wide range of light and medium weight ions with energies as high as 5 MeV however the tandem design means no heavy ions can be accelerated. The result is a high-energy low flux irradiation of the sample.



Figure 4-3: The STAR accelerator used for this project, which is housed at the Centre for Accelerator Science, ANSTO.

4.5 Materials Selection

Nuclear reactors are made up of many different materials, from metal alloys through to semi-metallic and ceramics. Some of these materials will be directly exposed to radiation of varying dose.

Material selection for this project was initially broad, however after some initial experiments a large suit of stainless steel grades were chosen as the focus materials in order to give a good comparison between a similar material with a broad range of crystal structures and alloying elements. As discussed in the literature review, stainless steels have long been used in the construction of nuclear reactors and are still one of the main materials chosen for construction today.

Table 4-1: Table showing materials used in various types of nuclear reactors. M.T. Simnad, Nuclear reactor materials and fuels, in Encyclopedia of Physical Science and Technology, Third Edition, R.A. Meyers (Ed.), Academic Press, 2001, pp. 775 – 815.

Reactor component	Reactor system material				
	BWR	PWR	CANDU	AGR	LMFBR
Core					
Fuel/cladding	UO ₂ /Zircaloy	UO ₂ /Zircaloy	UO ₂ /Zircaloy	UO ₂ /SS	UO ₂ , 25 ± 5% PuO ₂ /SS
Control materials	B ₄ C/Type 304 SS	AgInCd alloy	B ₄ C/SS	B ₄ C/SS	B ₄ C/SS
	UO ₂ -Gd ₂ O ₃ /Zircaloy 2	B ₄ C-Al ₂ O ₃ ; borosilicate glass			
Breeding blanket	NA	NA	NA	NA	UO ₂ /Type 316 SS
Reactor vessel					
Shell	Low-alloy steel (SA533 Gr. B)	Low-alloy steels (SA533 Gr. B., SA508)	Zircaloy tubes in Al calandria	Prestressed concrete	Type 304 SS
Cladding	Type 308L SS (SA264)	Type 308 SS: Inconel 617			NA

Of the stainless steels used in this project there are two main types, austenitic and ferritic. Austenitic steels are an important material in current and future reactors as well as one of the most commonly utilised engineering alloys. They are Fe-Cr-Ni alloys with 15 – 20% Cr, 8 – 15% Ni and the remaining balance Fe. The crystal structure is face centered cubic (fcc) which is close packed and imparts most of their physical and mechanical properties [57].

Commercial grades of austenitic stainless steel as used in nuclear reactor applications are 304, 316, 321 and 347, two of which have been studied in this project. These grades have the desired strength and ductility at both low and high temperatures, with an excellent resistance to fatigue and are most often used in the solution-annealed condition [26].

Ferritic steels are known for their excellent void swelling resistance in a radiation environment compared to austenitic steels and for this reason are seen as a candidate material for future reactor designs including fusion. The current generation of ferritic and ferritic-martensitic steels are made up of 9 – 12% Cr-Mo with the microstructure being easy to control with simple heat treatments resulting in the desired mechanical properties. The crystal structure is body centered cubic (BCC) which is carefully controlled with different alloying elements [31].

Material selection for this project is discussed further in chapter six.

4.6 Instrumentation Selected

Radiation damage studies of stainless steel reactor materials mainly focus on the change in the material's crystal lattice and how these changes will intern affect the material's mechanical properties during their service life. In order to study the material's microstructural changes several instruments have traditionally been used, these include many electron microscope techniques, Rutherford backscattering spectrometry (RBS) and X-Ray diffraction (XRD). These microstructural studies can also be complimented with many different macrostructural techniques when trying to link together how the microstructural changes induced by radiation damage effects the material's mechanical properties.

This research project has a heavy focus on electron microscopy techniques coupled with several complimentary marcostructural techniques. The use of electron microscopy has also required the use of some specialist sample preparation in order to study cross sections of the ion implanted stainless steels. In-depth discussion on all instruments used in this project will be covered in the next chapter of this thesis.

5 EXPERIMENTAL: CHARACTERISATION OF MATERIALS

5.1 Introduction

This chapter will cover the sample preparation, instrumentation and methods used in this project to characterise the materials before and after ion implantation.

5.2 Materials

As mentioned in chapter 4 the materials chosen for this project are stainless steels of varying grades, however the initial experiments were all carried out on 316 grade stainless steel until we had determined the best experimental procedure for the project. The table below summarises the materials tested in this project.

Table 5-1: Compositions and crystal structures of the stainless steel materials being studied in this project.

Grade	Crystal Structure	Composition wt%
316	FCC	Cr 17, Ni 12 Mo 2
304	FCC	Cr 18, Ni 8
430	BCC	Cr 17
MA956	BCC	Cr 19, Al 4
2205	FCC/BCC	Cr 22 Ni 5 Mo 3

5.3 Pre Irradiation Sample Preparation

It is extremely important that the samples being analysed in these experiments be free from any deformation before the ion implantation takes place otherwise any radiation damage simulated using ion implantation may have been pre-existing. Electron backscatter diffraction (EBSD) is a technique that requires deformation free samples and therefore was chosen as the method for ensuring the samples have been prepared

correctly before any ion implantation was done. EBSD is fully explained in the following section.

The stainless steel samples were prepared for EBSD analysis following the Struers method for polishing Low Carbon Steels (Method No. 1879). The samples were then mapped using a Zeiss Ultra Plus SEM coupled with an Oxford Instruments HKL NordlysS EBSD detector system at an accelerating voltage of 20 kV. The EBSD maps were generated using the HKL Channel 5 software.

5.4 Characterisation of Materials

Pre and post-irradiation characterisation is essential for quantifying changes made to the material's macro and microstructure in these experiments. For this project we have chosen to focus on electron microscopy techniques coupled with some micro surface testing studies. Detailed explanations of the instrumentation used are written below.

5.4.1 Scanning Electron Microscopy (SEM)

Scanning electron microscopy is a powerful characterisation tool in radiation damage studies. The ability to perform pre and post-irradiation of materials in plan view and cross section down to the nanometer scale along with chemical composition and crystal orientation effects is extremely useful.

For this research a Zeiss Ultra Plus field emission SEM was used fitted with an Oxford Instruments X-Max 80 mm² SDD X-ray microanalysis system and Nordlys S EBSD detector. Operating conditions can vary for each technique and will be listed specifically in the relevant chapters.

5.4.2 SEM Secondary Electron Imaging

Secondary electron imaging is primarily used for focusing the SEM and detecting changes in surface morphology due to radiation damage. With modern field emission

SEMs as used in this research we are able to achieve very high resolution even at low energy. This is very useful as at low beam energy we are imaging the true surface of the sample.

5.4.3 SEM Backscattered Electron and Backscattered Electron Channelling Contrast Imaging

Backscattered electron imaging (BSEI) is what we call atomic number contrast or composition imaging. The backscattered electrons will give a brighter signal when interacting with atoms of higher atomic number, this allows us to separate regions of differing chemical composition for further analysis in the materials we are analysing. For radiation damage studies using ion implantation this is very important, as we would like to see if there are any direct changes to the samples composition due to implantation.

Backscattered electron channelling contrast imaging (BSECCI) is what we call orientation contrast. We are attempting to filter out the atomic number contrast and reveal the orientation contrast, which will reveal changes in the crystallographic structure as a result of the ion implantation. This detector has been fundamental to this research as crystallographic changes are a primary effect of radiation damage in materials. The Zeiss Ultra Plus uses an Angular Selective Backscatter (ASB) detector to achieve the BSECC images. This works by using the absence of a magnetic field below the final objective lens, this way the BSE's are free to travel in their natural trajectory. By placing the ASB detector close to the sample we are able to detect the single elastically scattered electrons and filter out atomic number contrast giving high-resolution orientation contrast imaging.

5.4.4 Energy Dispersive X-Ray Spectroscopy (EDS)

Energy dispersive spectroscopy (EDS) allows us to qualitatively and quantitatively analyse the chemical composition of the materials studied in these experiments. It is important to fully understand the compositions of the materials studied as ion implantation effects can vary widely with differing chemical compositions. It is also

essential to analyse samples post-implantation to check for a change in composition due to the irradiation. X-ray mapping is also utilised to reveal trends in areas exposed to radiation damage.

The EDS system used in this project was an Oxford instruments X-max 80 mm² detector together with Oxford Instruments INCA software.

5.5 Atomic Force Microscopy Analysis (AFM)

Atomic force microscopy (AFM) is used in ion implantation studies to detect with very high-resolution evidence of the sputtering away of the samples surface by the accelerated ions. With electron microscope techniques we can generate images of the sample surface at very high resolution however we cannot measure the vertical dimension, the height or depth of the samples surface features. AFM uses a sharp tip to probe the surface features by raster scanning; the technique can image the surface topography with extremely high magnifications, up to 1,000,000x, comparable or even better than some electronic microscopes.

AFM was performed for this project using an Agilent Technologies G300 NanoIndenter.

5.6 Microhardness Measurement

Microhardness measurement performed in these experiments is done using instrumented indentation to maximum loads of 50 mN and 250 mN and was performed with an Agilent Technologies G300 NanoIndenter. As mentioned above the implanted ions can result in a change in the material's surface hardness that will change the material's mechanical properties. These observations are important to understand in radiation damage studies as the materials selected for reactor materials will have specific mechanical properties requirements.

5.7 Electron Backscatter Diffraction (EBSD)

Electron backscatter diffraction (EBSD) has been a very important characterization technique in this research project. EBSD gives us crystal orientation information and thus relies on the sample being crystalline with a deformation free crystal lattice. We will see later in this thesis how EBSD has been used to study deformation as a result radiation damage and how novel EBSD mapping was used to reveal trends in multi-phase systems over large areas of damaged material. The samples were mapped using a Zeiss Ultra Plus SEM coupled with an Oxford Instruments HKL NordlysS EBSD detector system at an accelerating voltage of 20 kV. The EBSD maps were generated using the HKL Channel 5 software.

5.8 Computer Modeling of Damage (SRIM)

Stopping range of ions in matter (SRIM) is a computer modeling software which allows us to predict mean depth, maximum depth, vacancies per ion implanted and total number of atoms sputtered per ion implanted. These calculations are very important in not only understanding how the sample will behave with various types of ion implantation but also allowing us to apply specific sample preparation techniques that retain the areas of interest at a target depth within the damaged samples.

5.9 Cross Sectional Sample Preparation

Cross sectional sample preparation is very significant in radiation damage studies as we want to be able to study what is happening beneath the surface of the materials as a result of the ion implantation. Due to the very shallow nature of the damage region we have had to employ and develop some very specialised sample preparation techniques. The various methods trialed and implemented in these experiments have been detailed below.

5.10 Mechanical Polishing

Using SRIM calculations we were able to determine the expected damage layer depths for both STAR and PI^3 ion implantation of helium ions in our stainless steel samples.

Using this data we first tried mechanically polishing the samples, as it is the simplest way to get a good finish without using any special equipment. Mechanical polishing involves a series of polishing steps with various polishing media. The stainless steel samples were prepared for EBSD analysis following the Struers method for polishing Low Carbon Steels (Method No. 1879). This method worked well for the STAR implanted samples as damage depths were in the order of 8 – 12 microns. For the PI³ samples, however, this method caused too much edge rounding and the region of interest was lost.

5.10.1 Cross Sectional Ion Beam Polishing

Cross sectional ion beam polishing is an EBSD sample preparation method which can be useful for preparing large cross sectional areas to a very high quality finish. The instrument uses an argon ion beam under vacuum to sputter away the cross-section and the use of a shield at the sample surface keeps this region free of sputtering. Minor or even no edge rounding in the region of interest should be achievable with this technique however we found this instrument to be very inconsistent and were not able to get a repeatable result on our implanted stainless steel materials. The instrument used was a JEOL SM-09010 Cross Section Polisher.

5.10.2 Focused Ion Beam (FIB)

Focused ion beam (FIB) is not usually used for large area cross-section preparation for EBSD however due to the shallow nature of the damage region it was decided to try and use this technique. The FIB uses a focused beam of gallium ions to sputter away material in a very controlled manner. The FIB is mounted onto an SEM column so we have the ability to image the sample at high resolution and target specific areas for ion beam milling. The main issue with FIB is instrument availability and the amount of time consumed in preparing a sample. Preparing samples for EBSD was not possible due to this however later in the project a new FIB became readily available and samples were prepared for transmission electron microscopy (TEM) successfully using this instrument.

The FIB used for the early work was a FEI Quanta 200 3D. Later FIB work was carried out using a Zeiss Auriga 60.

5.10.3 Precision Ion Beam Polishing (PIPS)

Precision ion beam polishing (PIPS) was the final technique used for preparing large area cross-sections for EBSD and was very successful. PIPS uses an argon ion beam under vacuum to sputter away the material on a rotating stage at very shallow angles. PIPS is typically used for preparing smaller areas like TEM samples however due to the shallow nature of the damage region in our samples we were able to successfully prepare an area large enough for EBSD mapping with no edge rounding in the sub 100nm region below the sample surface.

A Gatan Model 691 PIPS was used for this research project.

5.11 TEM Sample Preparation

TEM sample preparation for this research project was performed using a FIB. Please see below for full details.

5.11.1 Focused Ion Beam

Focused ion beam (FIB) allows for precise and targeted area trench cutting and the thinning and polishing of the lifted out cross sections for examination in the TEM. The use of a FIB equipped with EBSD has allowed us to target specific grain boundaries in the stainless steel samples. The grain boundaries between phases in the duplex steel have been particularly interesting with respect to radiation damage studies, without an SEM combined with FIB this would not be possible. A Zeiss Auriga 60 FIB SEM was used for this research project. Details of the method will be explained in chapter six.

5.12 Transmission Electron Microscopy (TEM) Characterisation

Transmission electron microscopy (TEM) characterisation of ion-implanted samples was required to image the resulting defects formed in the cross section of the stainless steel materials at high resolution. As discussed in the literature review, TEM is a very important technique for use in radiation damage characterisation, the contrast imaging techniques can give visual insight into the mechanisms of damage like no other instrument. The instrument used for this project was a JEOL 2200 TEM at 200 keV.

6 RESULTS AND DISCUSSION

6.1 Introduction

This chapter of the thesis will include the results obtained in this project with respect to the characterisation methods used on the materials before and after ion implantation. The results obtained will also be discussed to show how this research has been able to reveal some interesting trends using some previously undocumented characterisation techniques in radiation damage studies.

Some initial experiments were undertaken to focus the direction of this research, the first experiment involved the determination of the effect of plasma immersion ion implantation (PI³) on a stainless steel (316) microstructure, utilising argon and helium ions as damaging ions. The second initial experiment involved the determination of the effect of ion irradiation on a stainless steel (316) microstructure, utilising helium ions as the damaging ions in the Small Tandem for Applied Research (STAR) accelerator.

The results obtained from the STAR accelerator's high-energy low flux ion implantation are used to compliment the results from the PI³ ion implantation which implants ions with low energy at a high flux.

6.2 First Initial Experiment

In the first experiment a small piece of 316 stainless steel was prepared for EBSD analysis using the Struers method for polishing Low Carbon Steels (Method No. 1879). The sample was then mapped using a Zeiss Ultra Plus SEM with an Oxford Instruments HKL NordlysS detector system. The map was generated using the HKL Channel 5 software. Ion implantation utilised using two different noble gases, argon and helium respectively at 40 kV accelerating voltage, and to a fluence of $\sim 1 \times 10^{17}$ ions cm^{-2} . Portions of the materials were shielded using both a silicon wafer and a TEM grid. Atomic Force Microscopy was used to determine if material had been sputtered away from the surface due to the ion implantation. Instrumented indentation to a maximum load of 250 mN was performed with an Agilent Technologies G300 NanoIndenter to

determine if surface hardening had occurred due to the implanted ions. Post irradiation EBSD was used to analyse both the shielded and non-shielded surfaces. Finally EDS was utilised to determine the presence of remaining argon in the sample irradiated using argon.

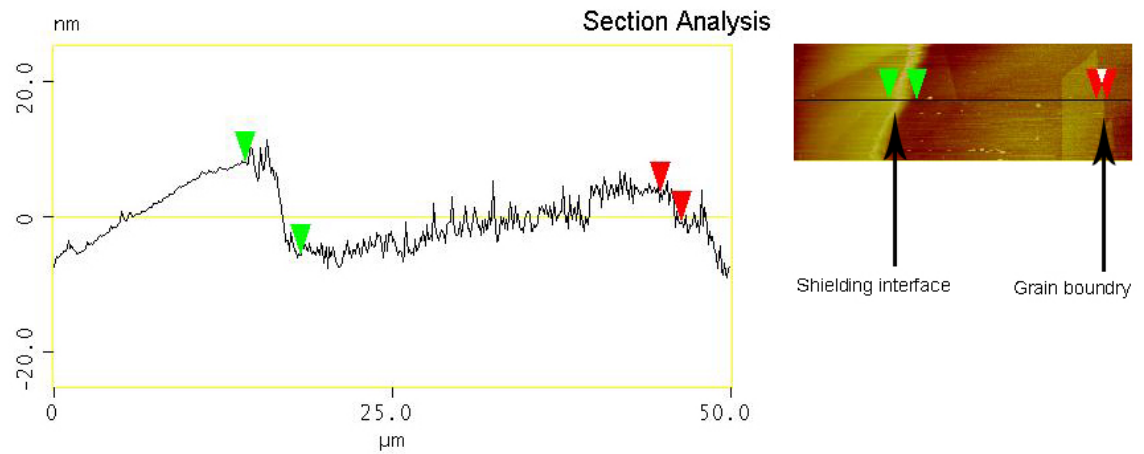


Figure 6-1: Atomic Force Microscopy (AFM) showing some evidence (13 nm) of sputtering and surface degradation was measured when using argon ions.

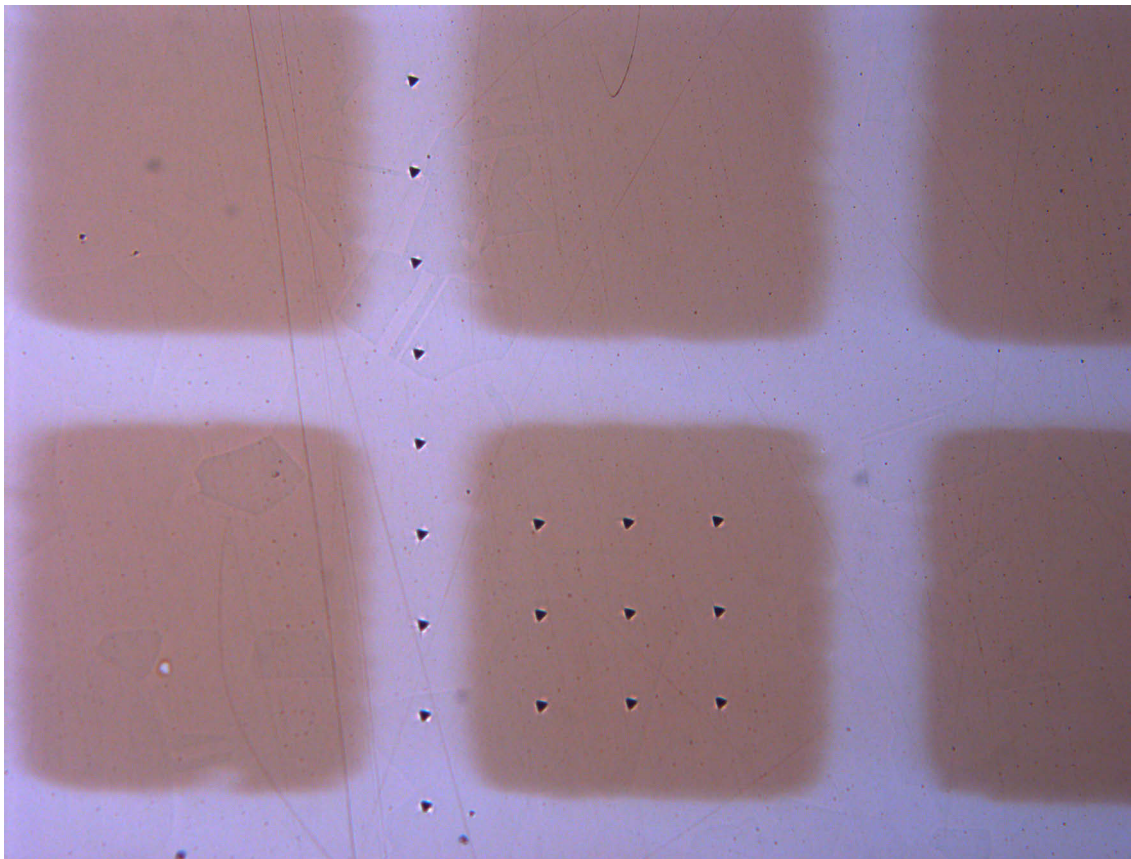


Figure 6-2: Optical image showing the regions where instrumented indentation was performed in the shielded and irradiated regions.

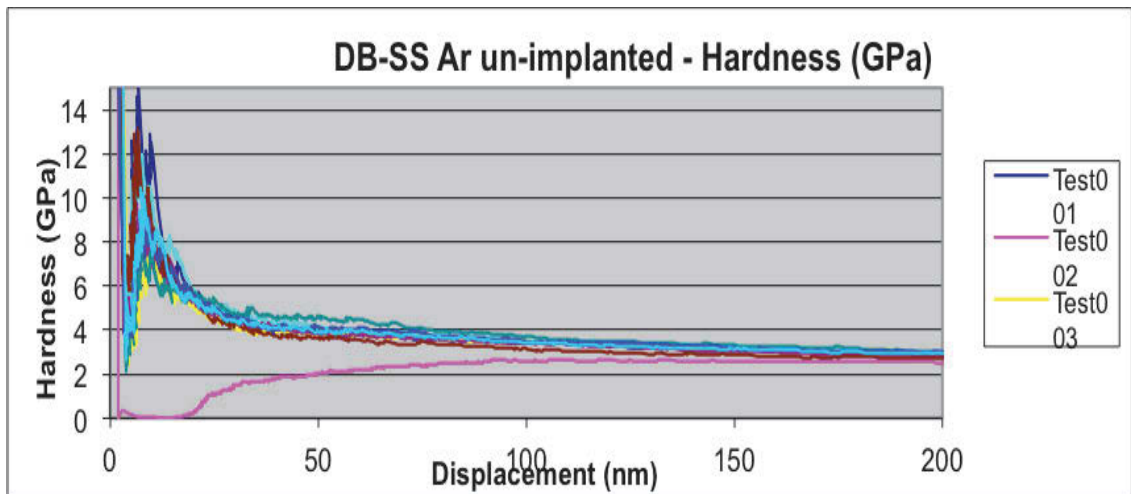


Figure 6-3: Results from the instrumented indentation to a maximum load of 250 mN as performed on the shielded region of the argon implanted steel.

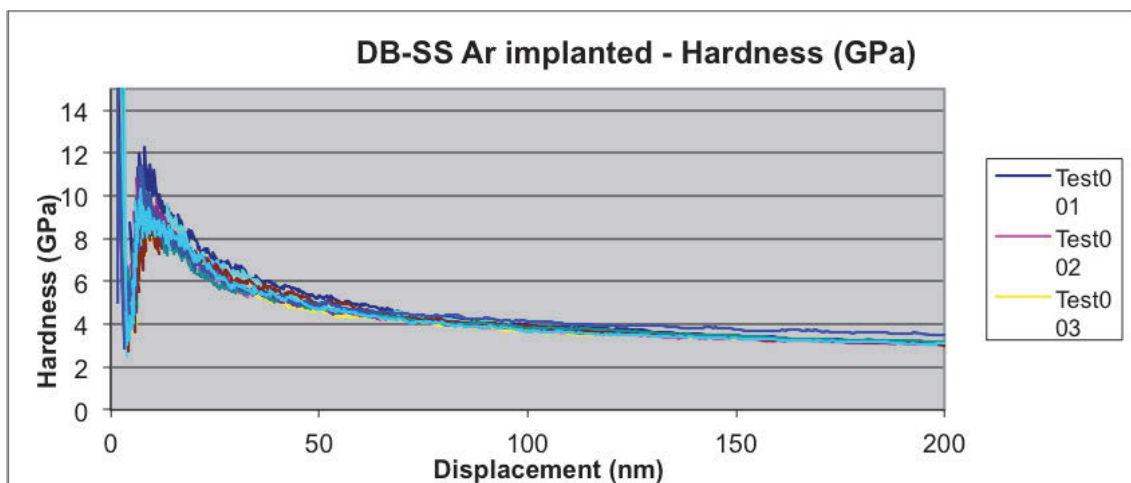


Figure 6-4: Results from the instrumented indentation to a maximum load of 250 mN as performed on the unshielded region of the argon implanted steel.



Figure 6-5: EBSD Map of 316 stainless steel before ion implantation. Map shows euler angle colouring with a very high pattern indexing rate.

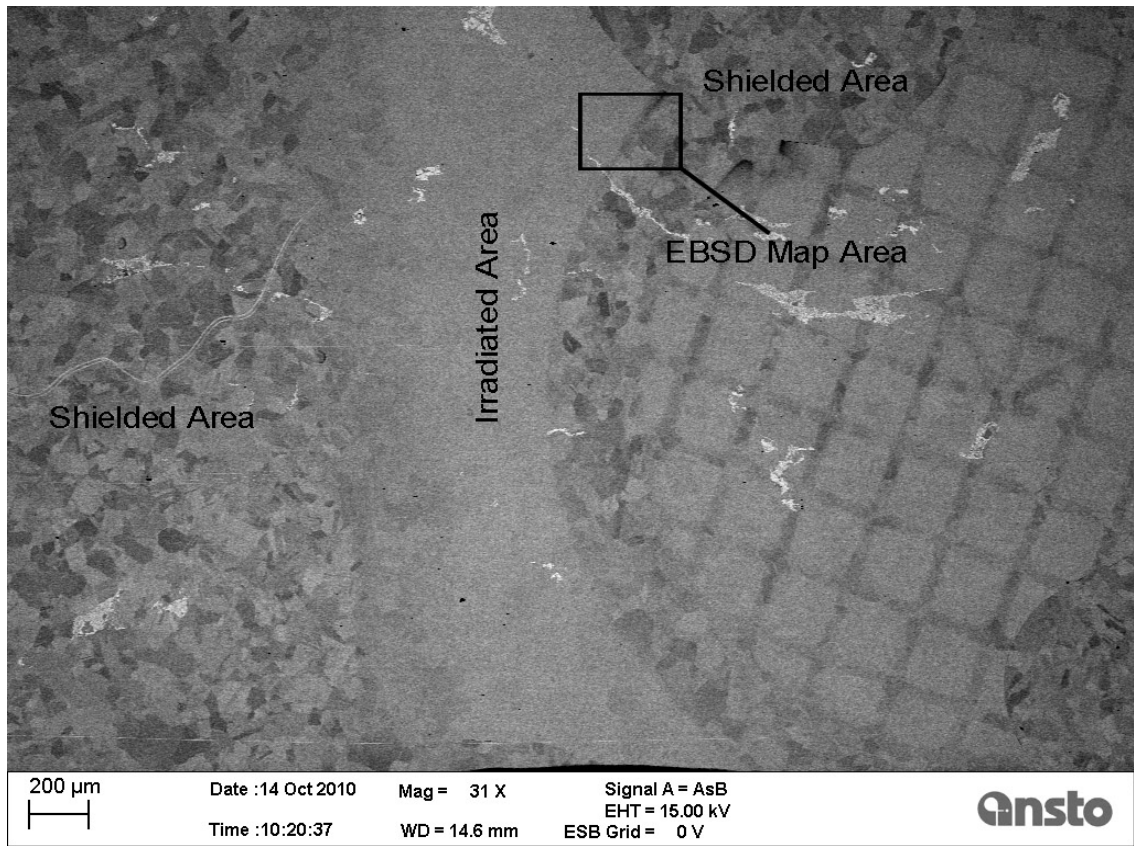


Figure 6-6: Backscattered electron image showing the irradiated and shielded regions and also the region where the EBSD map was taken from on the polished stainless steel surface. Argon ions were used for implantation.

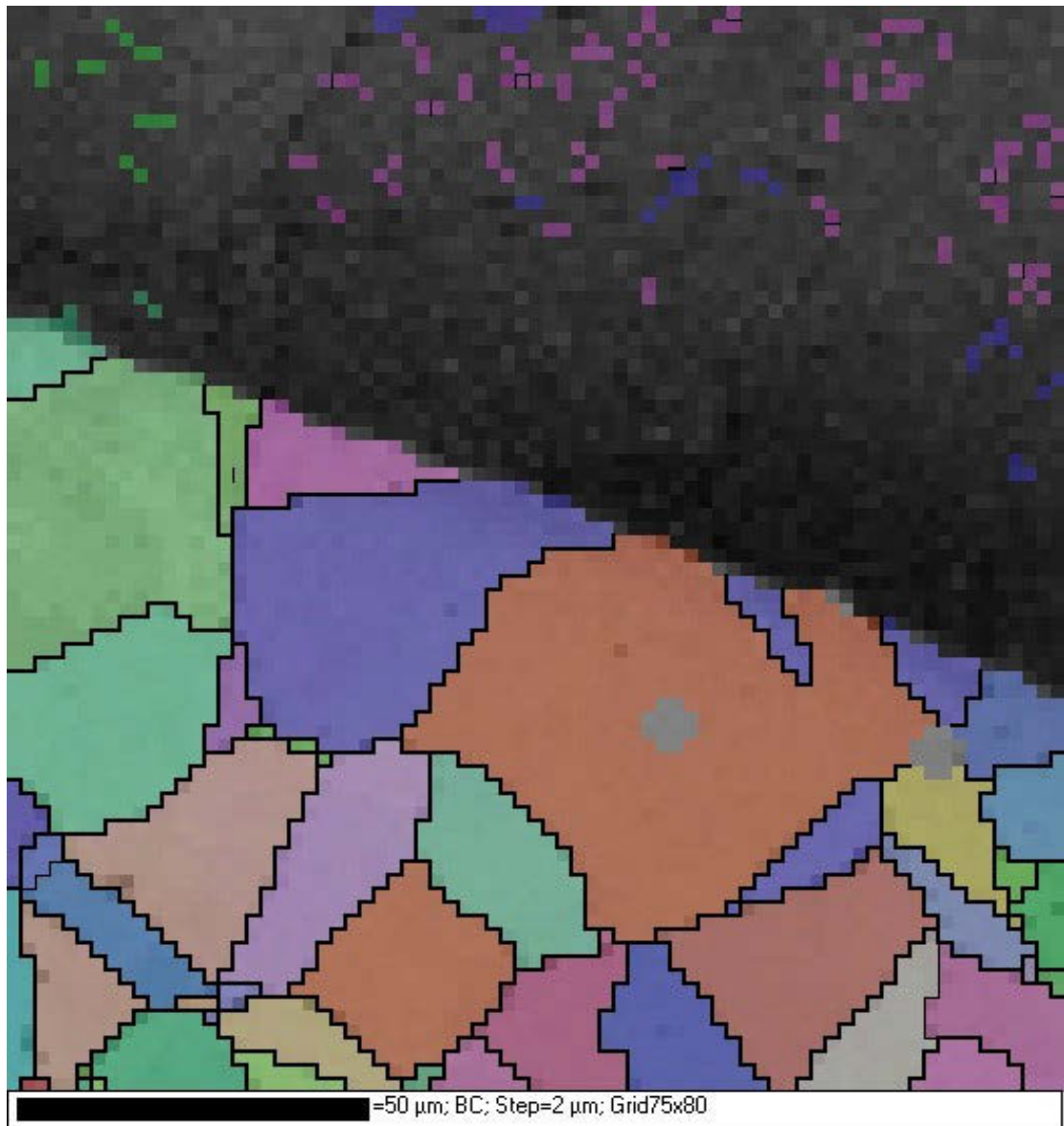


Figure 6-7: Corresponding EBSD map showing the loss of EBSD pattern indexing in the irradiated region (top of map).

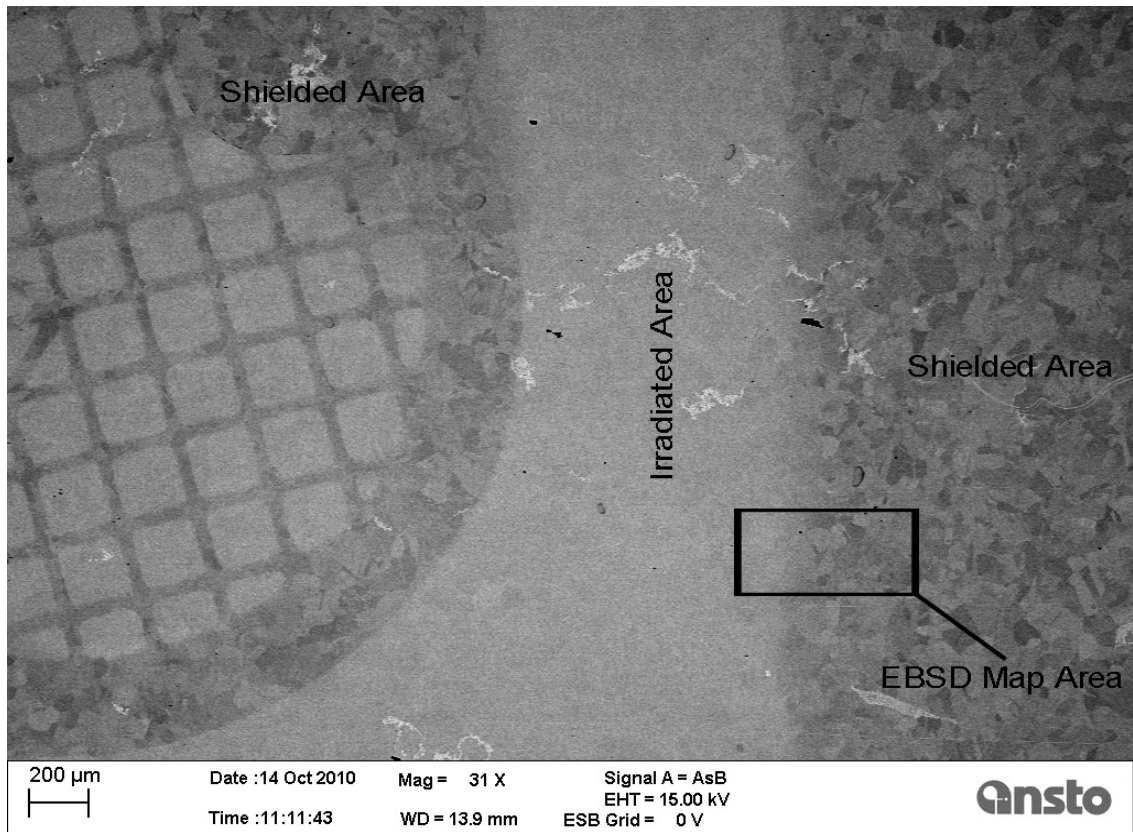


Figure 6-8: Backscattered electron image showing the irradiated and shielded regions and also the region where the EBSD map was taken from on the polished stainless steel surface. Helium ions were used for implantation.

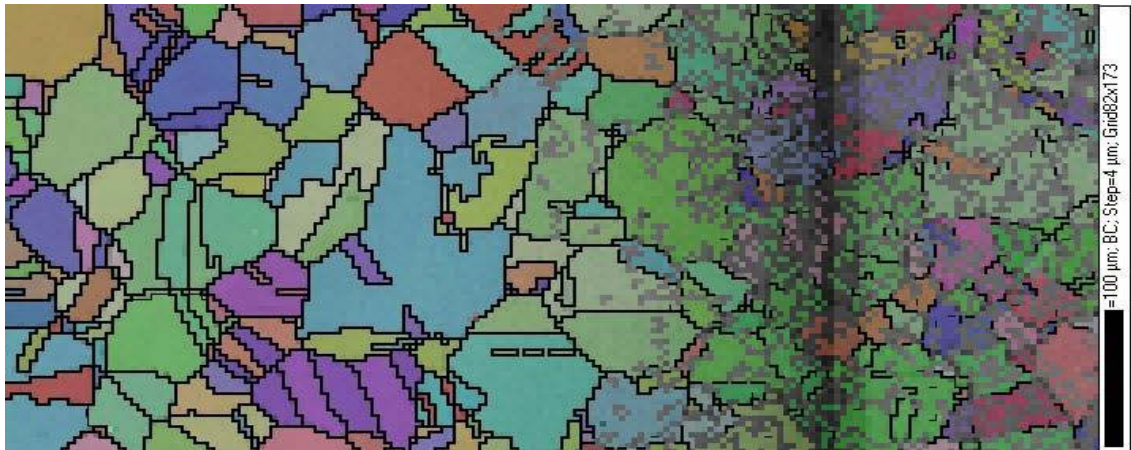


Figure 6-9: Corresponding EBSD map showing the loss of EBSD pattern in the irradiated region (right hand side of the map). Note the area mapped was shielded using a silicon wafer and gave a gradient of damage across the mapped region unlike the hard edge given by the TEM grid used in figure 6.8.

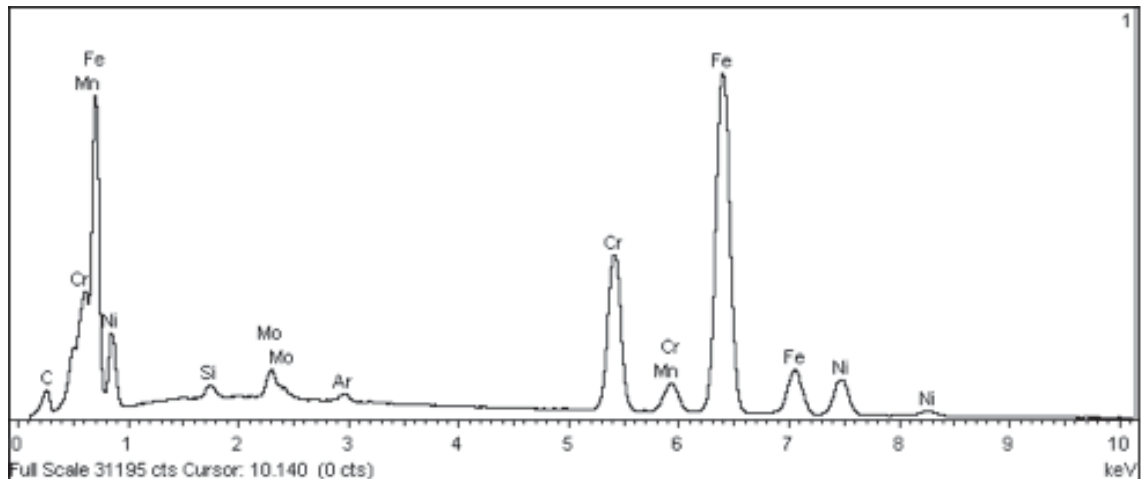


Figure 6-10: EDS spectrum showing argon present in the stainless steel ~0.2 weight % was found. However, this may not be considered representative of the true concentration as the interaction volume of X-ray generation will be predominantly below the region of deposited argon into the surface of the steel. As a result the fraction of argon present may be higher.

Discussion of First Initial Experiment:

Plasma immersion ion implantation using argon and helium ions significantly degraded the backscattered electron image and EBSD patterns on the 316 stainless steel sample. Based on these results, a comment can be made about the loss of EBSD pattern:

- i) Irradiation induced damage giving rise to a loss of ordered crystallinity in the material for sufficient diffraction.
- ii) Physical damage from the irradiation to the surface preparation for EBSD, removing the coherent scattering, and effectively giving rise to diffuse scattering from the surface
- iii) AFM of the Ar implanted stainless steel showed the sputtering away of 13nm of the material's surface.
- iv) AFM of He implanted stainless steel showed no evidence of any change in the surface topography.
- v) Differences in atomic number mean the Ar damage layer is much thinner than the He damage layer and therefore the energy is much more concentrated creating more damage.
- vi) Instrumented indentation showed a minimal increase in surface hardness for the Ar implanted steel.

vii) Instrumented indentation showed a 5 – 10% increase in surface hardness for the He implanted steel.

The next step will be to look at the cross section of the irradiated steel to determine the penetration depth of the damage and whether EBSD patterns are obtainable from the cross section. Helium ions should have penetrated further than argon, predominantly due to the mass/energy ratio of argon/helium.

6.3 Second Initial Experiment:

In the second initial experiment a small piece of 316 stainless steel was prepared as per the first initial experiment and mapped with EBSD. Ion irradiation was then utilised at 5 MeV accelerating voltage to a fluence of $\sim 2 \times 10^{17}$ ions cm^{-2} with the STAR accelerator. Post irradiation EBSD was used on the irradiated surface to determine whether the ion irradiation induced any dislocations/damage causing a loss of crystallinity sufficient to stop diffraction patterns from the material surface.

The sample was then cross-sectioned and re-polished to examine the microstructure and determine whether damage had occurred below the sample surface using high-resolution SEM imaging.

Second Initial Experiment Results:

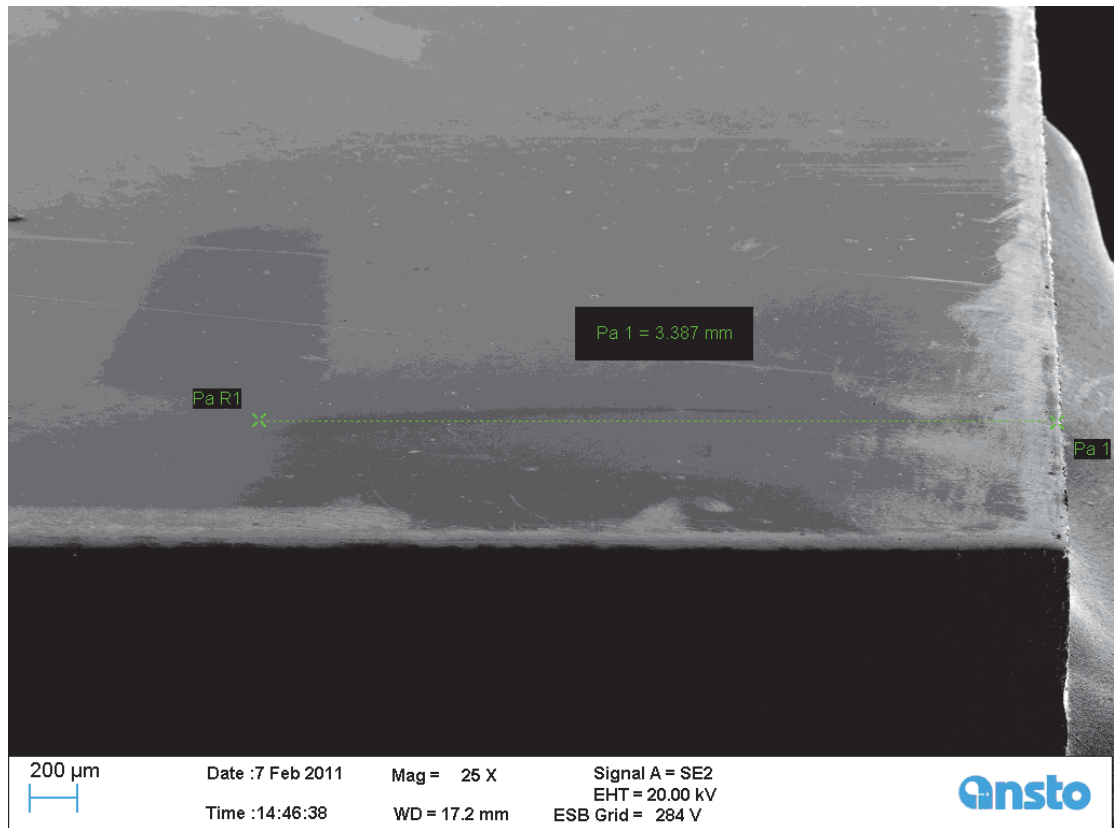


Figure 6-11: Secondary electron image showing the irradiated region.

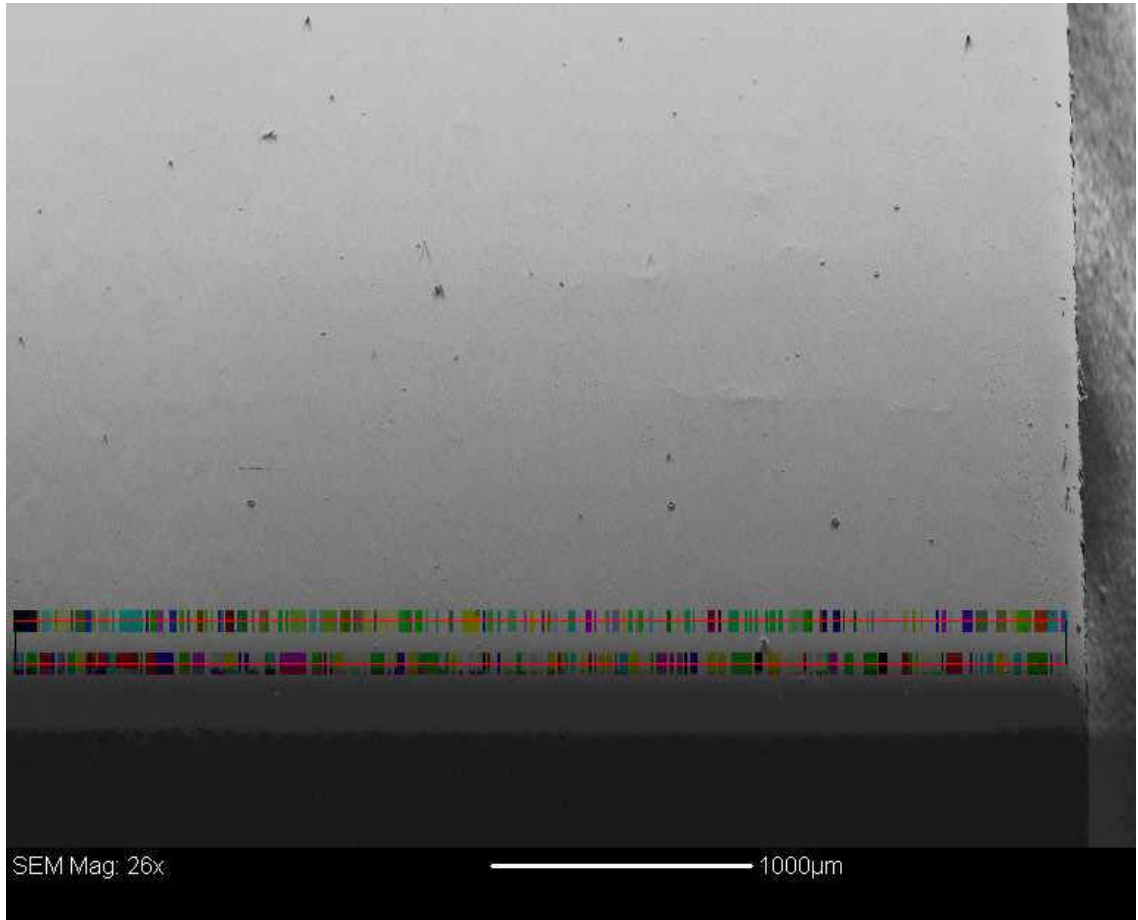


Figure 6-12: Corresponding EBSD line scans showing the EBSD pattern is still present in the irradiated region.

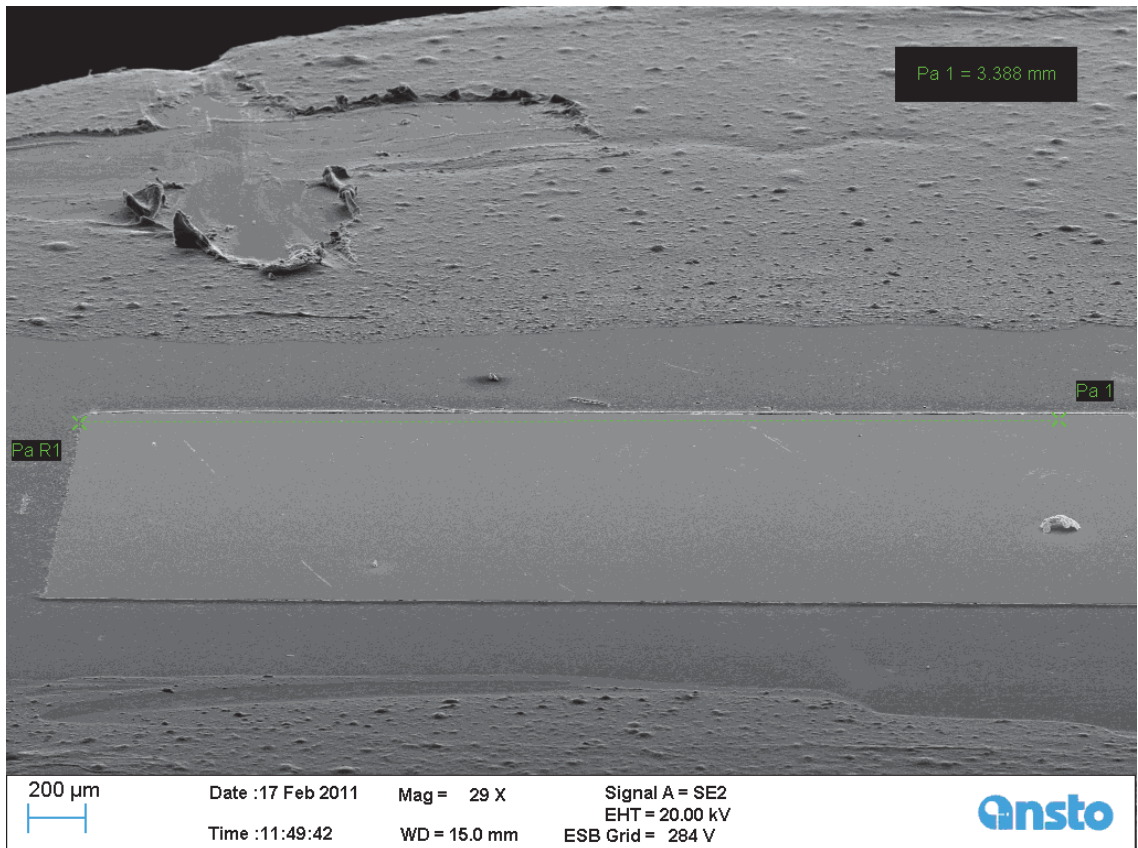


Figure 6-13: Secondary electron image showing the cross-section of the irradiated region mounted in epoxy resin and polished to a 1 micron diamond finish. Figure 6-14 below shows this region in high magnification.

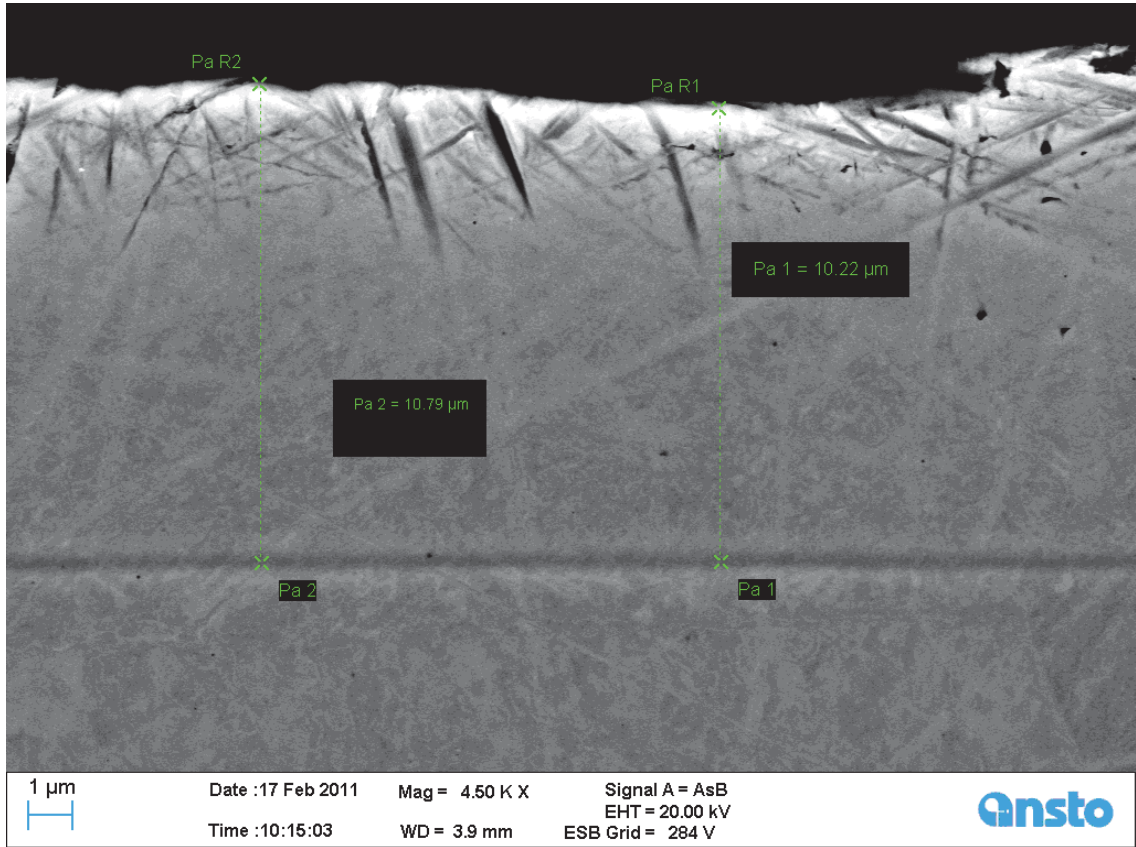


Figure 6-14: Backscattered electron channeling contrast image showing the cross-section of the irradiated region and a line of radiation damage caused by the helium ions approximately $10\mu\text{m}$ under the surface. Scratches remain in the top edge of the cross section due to edge rounding during mechanical polishing.

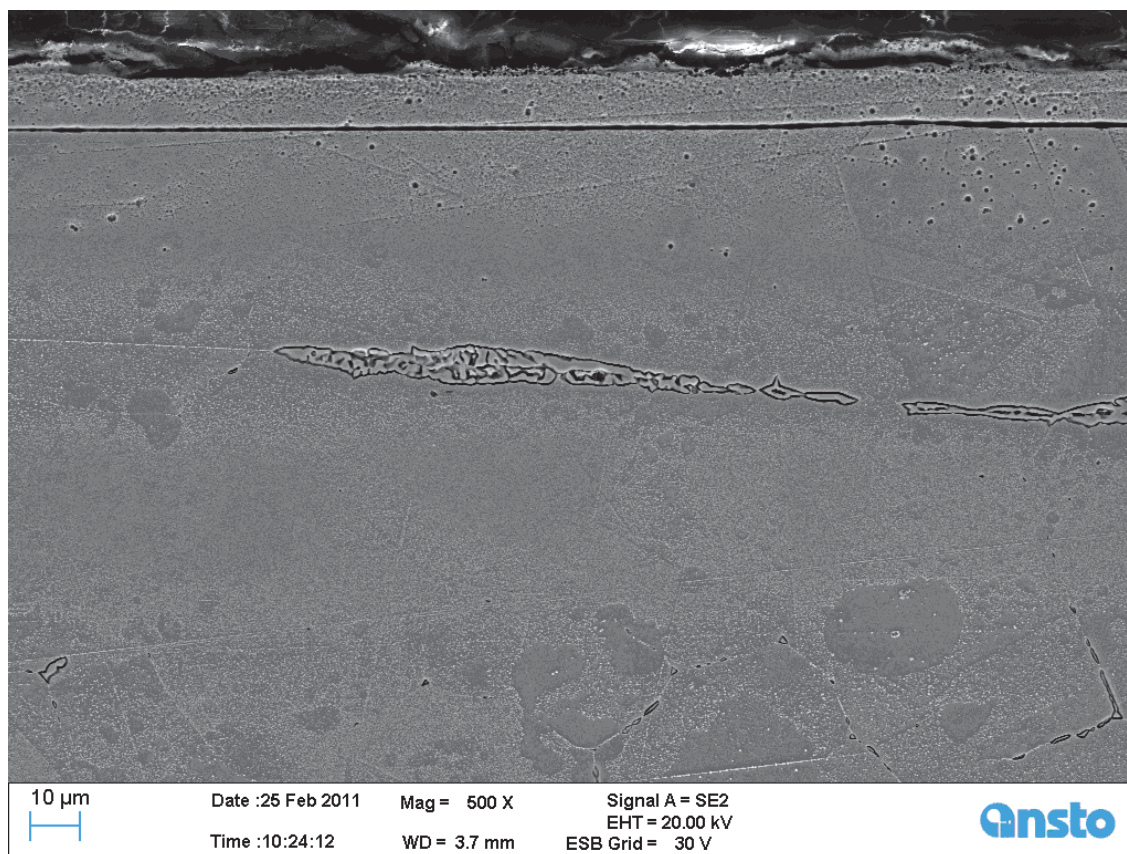


Figure 6-15: Secondary electron image showing the cross-section of the irradiated sample after heavy etching. The line of radiation damage caused by the helium ions approximately $10\mu\text{m}$ under the surface has been completely etched away.

Discussion of Second Initial Experiment Results:

Previous experiments using plasma immersion ion implantation significantly degraded the backscattered electron image and EBSD patterns on the 316 stainless steel sample as the energy used is low (40 keV) although the flux is very high causing damage predominantly at the sample surface ($< 300\text{ nm}$). This experiment using ion irradiation in the STAR accelerator uses much higher energy (5 MeV) at a relatively low flux. This high energy causes the ions to penetrate further into the material surface ($\sim 10\mu\text{m}$) leaving the material sample free from damage as confirmed by EBSD shown in figure 6.12 in this experiment. Cross sectional imaging in the SEM of the sample shown in figure 6.14 revealed a damage layer at a depth which has been predicted by SRIM calculations. Chemical etching was performed to confirm the presence of this damage layer as shown in figure 6.15. The voids and helium bubble formation present in the damage layer allow for rapid penetration of the chemical etch.

Conclusions from these initial experiments have revealed some very important aspects. Firstly we are able to use backscattered electron channelling contrast as a rapid method of identifying regions of damage to the material in the SEM as a result of the ion implantation. This was shown in both the initial experiments.

Secondly, we are seeing some interesting trends with respect to using EBSD as a characterisation technique for radiation damage studies. As discovered in the literature review EBSD has only previously been used primarily as a way of measuring bulk texture changes in metals after neutron irradiation. In these studies we are seeing a measurable loss of diffraction from the crystal lattice as a result of ion implantation.

The sole use of Helium ions for implantation will streamline future experiments, as Argon ions are not available in the high energy, low flux STAR accelerator. It has also been noted in the introduction that point defects are formed through helium ion implantation and when these point defects are mobile they can cluster forming point defect agglomerates and voids [51]. The implanted helium ions may reside in these voids and change their time dependent growth dynamics similar to those observed in fast neutron radiation damage studies [52]. Farrell [53] has shown the importance of helium gas (predominantly formed by nuclear transmutations) in radiation damage studies promoting the formation of cavities and enhancing the dislocation structure. Finally the sputtering effect we see with Argon ion implantation makes it very difficult to study the damaged material as most of it has been sputtered away.

Consequently, the research took the path of repeating the above experiments using helium ions with both accelerators on a suite of stainless steel materials with some additional characterisation techniques used to solidify our findings.

6.4 Investigation of various steels

The following stainless steel materials were chosen for next phase of the research. 316 is also shown in the table for comparison purposes. These materials are a mixture of ferritic and austenitic steels that contain different crystal structures and chemical compositions as shown in the table below.

Table 6-1: Compositions and crystal structures of the stainless steel materials being studied in this project.

Grade	Crystal Structure	Composition wt%
316	FCC	Cr 17, Ni 12 Mo 2
304	FCC	Cr 18, Ni 8
430	BCC	Cr 17
MA956	BCC	Cr 19, Al 4
2205	FCC/BCC	Cr 22 Ni 5 Mo 3

6.4.1 Investigation of 430 Grade Stainless Steel

Grade 430 stainless steel was chosen as it is ferritic with a BCC crystal structure which is different to the FCC austenitic 316 steel already tested in the initial experiments. Compositionally it has the same amount of chromium however it does not usually contain more than 1% nickel. The backscattered channeling contrast imaging and EBSD for the 316 material gave very interesting results as mentioned above in the initial work and therefore the 430 material was prepared in the same manner before ion implantation was performed using both PI³ and the STAR accelerator on two separate pieces of material.

Subsequent post-irradiation examination in the SEM using backscattered channeling contrast imaging and EBSD revealed some very interesting results. For the 430 grade steel the backscattered channeling contrast imaging was still able to distinguish grain boundaries and some orientation contrast in the unshielded region which was exposed to the ion implantation unlike the 316 material where all contrast was lost. The EBSD results were also revealing the same trend, this time we were able to partially index the ion implanted region of the 430 grade steel unlike the 316 grade steel where indexing was not possible.

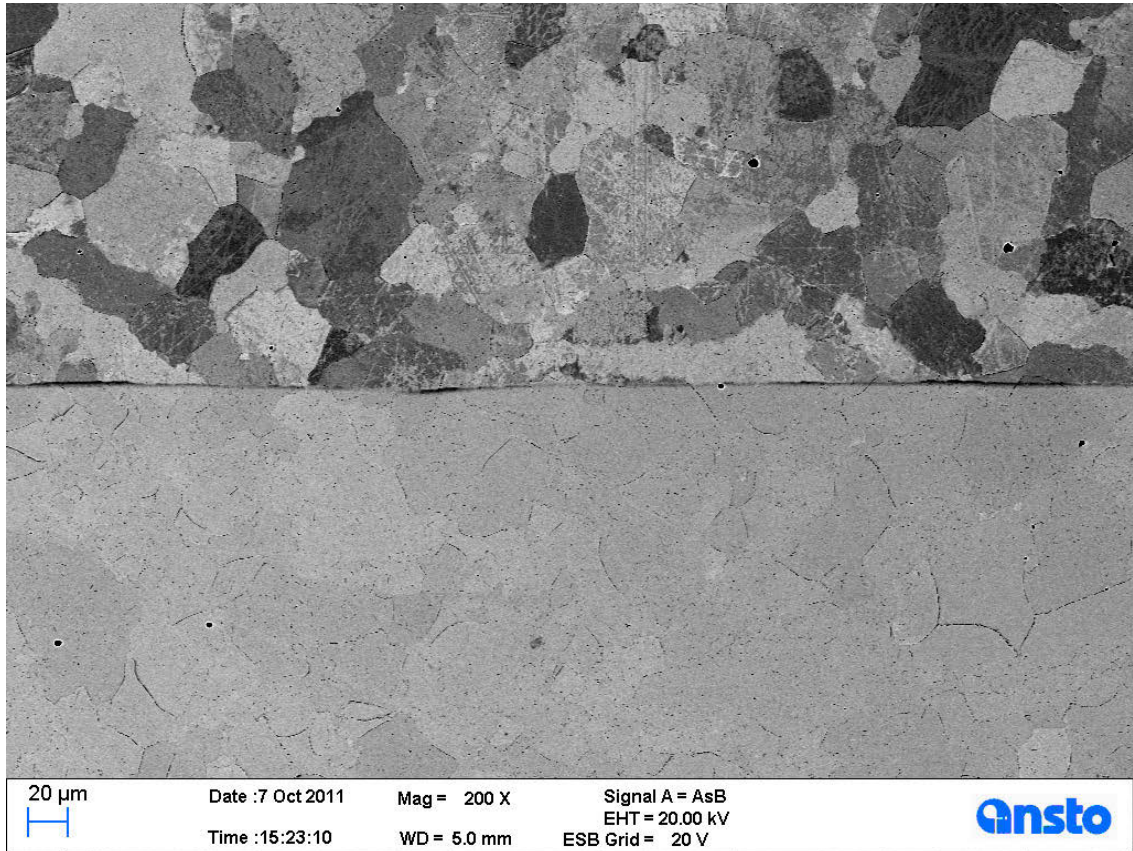


Figure 6-16: Backscattered electron channeling contrast image showing the irradiated and shielded regions of the 430 grade stainless steel. The region where the EBSD map was taken from on the polished stainless steel surface is also shown. Helium ions were used for implantation.

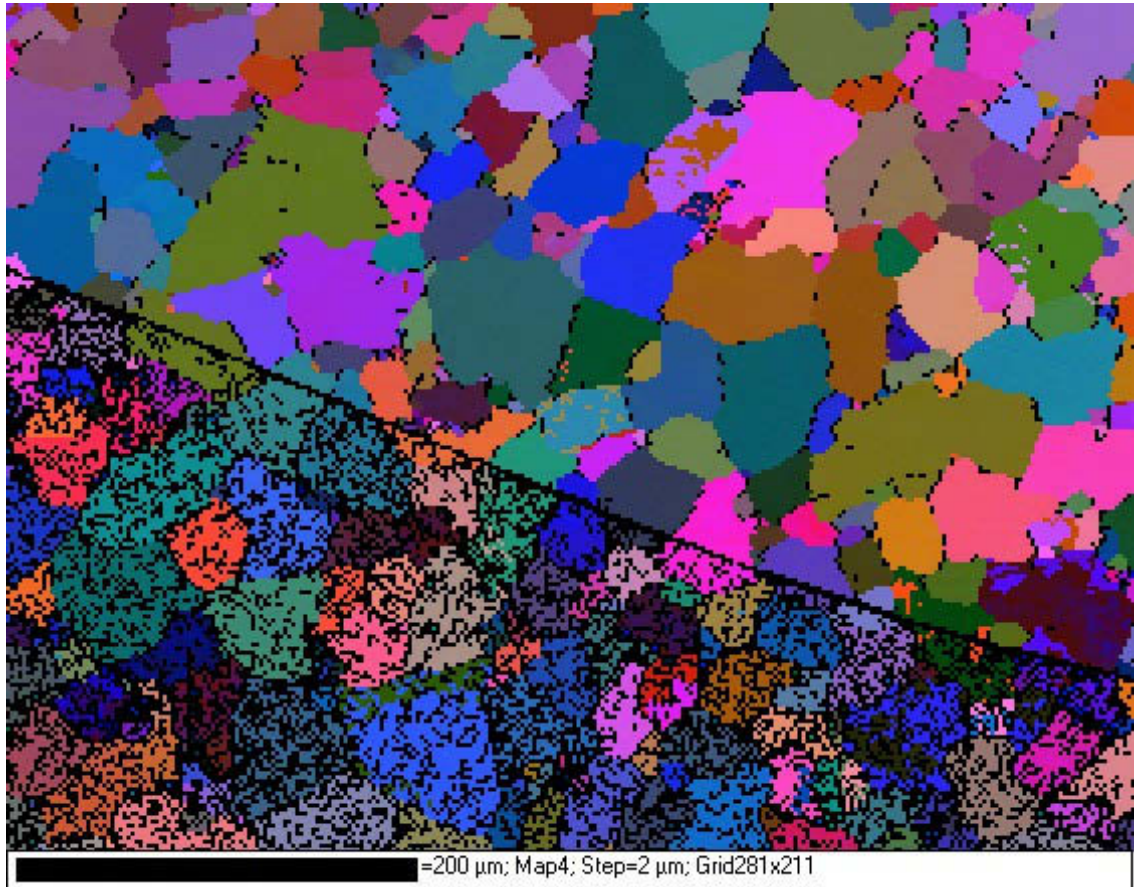


Figure 6-17: EBSD orientation map showing the partial indexing of the EBSD pattern in the non-shielded irradiated region (lower half) of the 430 grade stainless steel.

With these interesting results it was now decided to repeat these experiments on another austenitic steel sample to try and determine whether the crystal structure of the material was the main factor influencing the trend in backscattered channeling contrast imaging and EBSD results we had seen so far.

6.4.2 Investigation of 304 Grade Stainless Steel

Grade 304 stainless steel is one of the most commonly utilised steels. The stainless steel is austenitic with a FCC crystal structure and is compositionally similar to the 316, however, it contains a smaller amount of nickel and does not contain the molybdenum. The backscattered channeling contrast imaging and EBSD for the 316 and 430 materials gave very differing results. The 304 material was prepared in the same manor as these materials before ion implantation was performed using both PI^3 and the STAR accelerator on two separate pieces of metal.

Subsequent post-irradiation examination of the 304 grade steel in the SEM using backscattered channeling contrast imaging and EBSD revealed similar results we had previously seen with the 316 grade material. The backscattered channeling contrast imaging was still able to distinguish grain boundaries and some orientation contrast however not as well as in the 430 but significantly better than in the 316. The EBSD was not able to index the ion implanted region of the 304 grade steel just like we had seen in the 316 grade steel.

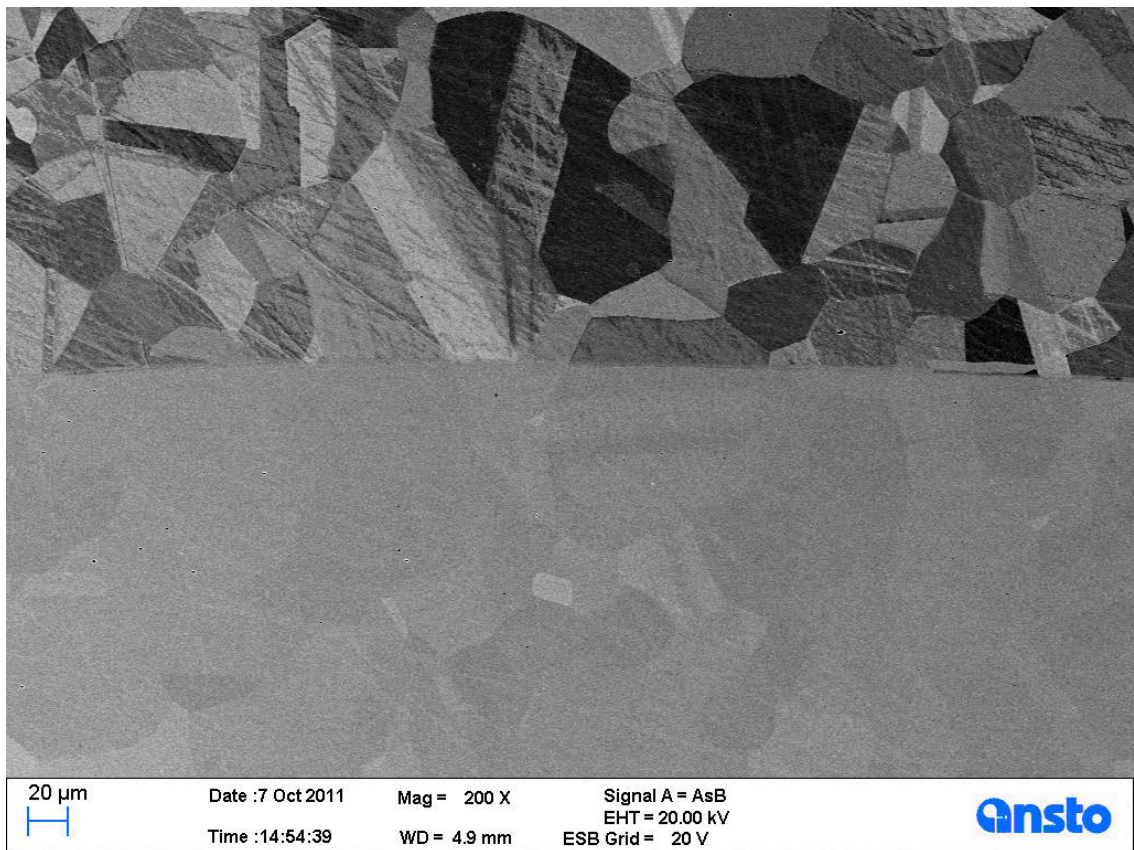


Figure 6-18: Backscattered electron channelling contrast image showing the irradiated (lower) and shielded region (upper) of the 304 grade stainless steel. Helium ions were used for implantation.

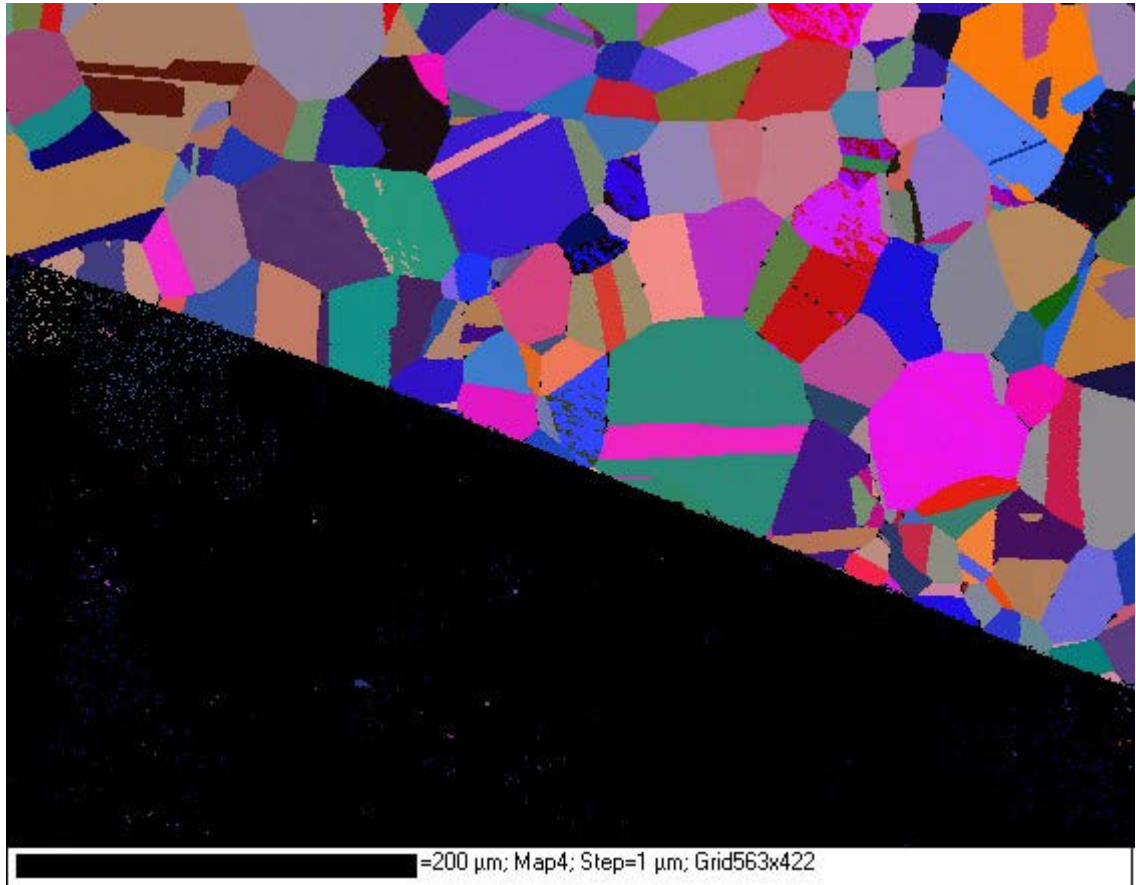


Figure 6-19: EBSD orientation map showing the complete loss of indexing of the EBSD pattern in the irradiated region (lower half) of the 304 grade stainless steel.

These results are revealing a trend for the FCC metals to lose their ability to be mapped using EBSD post helium ion implantation with the BCC metals only suffering a partial loss of pattern. It was now decided to completely solidify these findings by repeating these experiments on a 2205 grade duplex stainless steel.

6.4.3 Investigation of 2205 Grade Stainless Steel

The 2205 grade steel contains both the austenitic FCC structure and ferritic BCC structure in an equal mixture of uniform sized grains. By repeating these experiments on the duplex steel we are hoping to find the same EBSD indexing trends as seen on the individual steels previously studied but this time the effects should be seen on each grain.

The 2205 steel was prepared in the same manor as the previous experiments before ion implantation was performed using both PI³ and the STAR accelerator on two separate pieces of metal.

Subsequent post-irradiation examination of the 2205 grade steel in the SEM using backscattered channeling contrast imaging and EBSD revealed similar results we had previously seen with the 430 and 304 grade stainless steels. The backscattered channeling contrast imaging was still able to distinguish some grain boundaries and orientation contrast. The EBSD results however were quiet different with the duplex steel and it was not until we displayed the map using phases that we could see the trend we were hoping to reveal by selecting this material for the experiment.

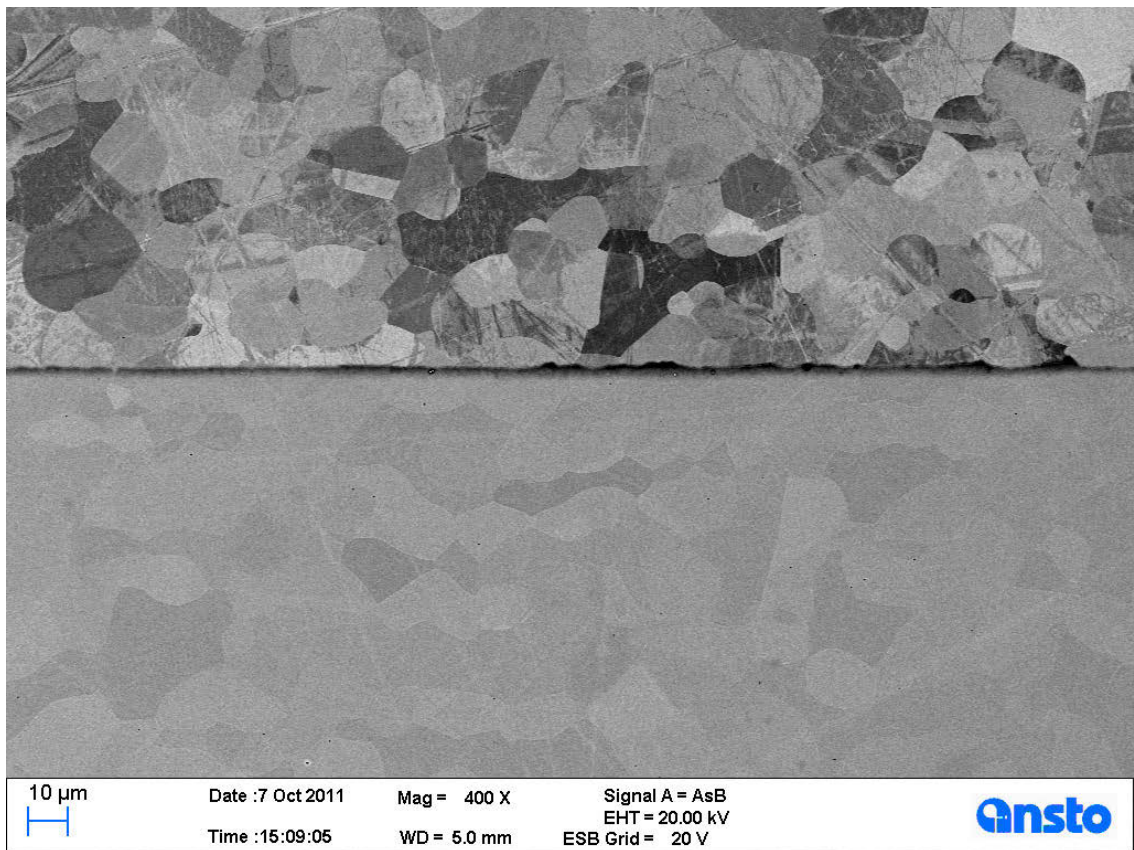


Figure 6-20: Backscattered electron channeling contrast image showing the irradiated and shielded regions of the 2205 grade stainless steel. The region where the EBSD map was taken from on the polished stainless steel surface is also shown. Helium ions were used for implantation.

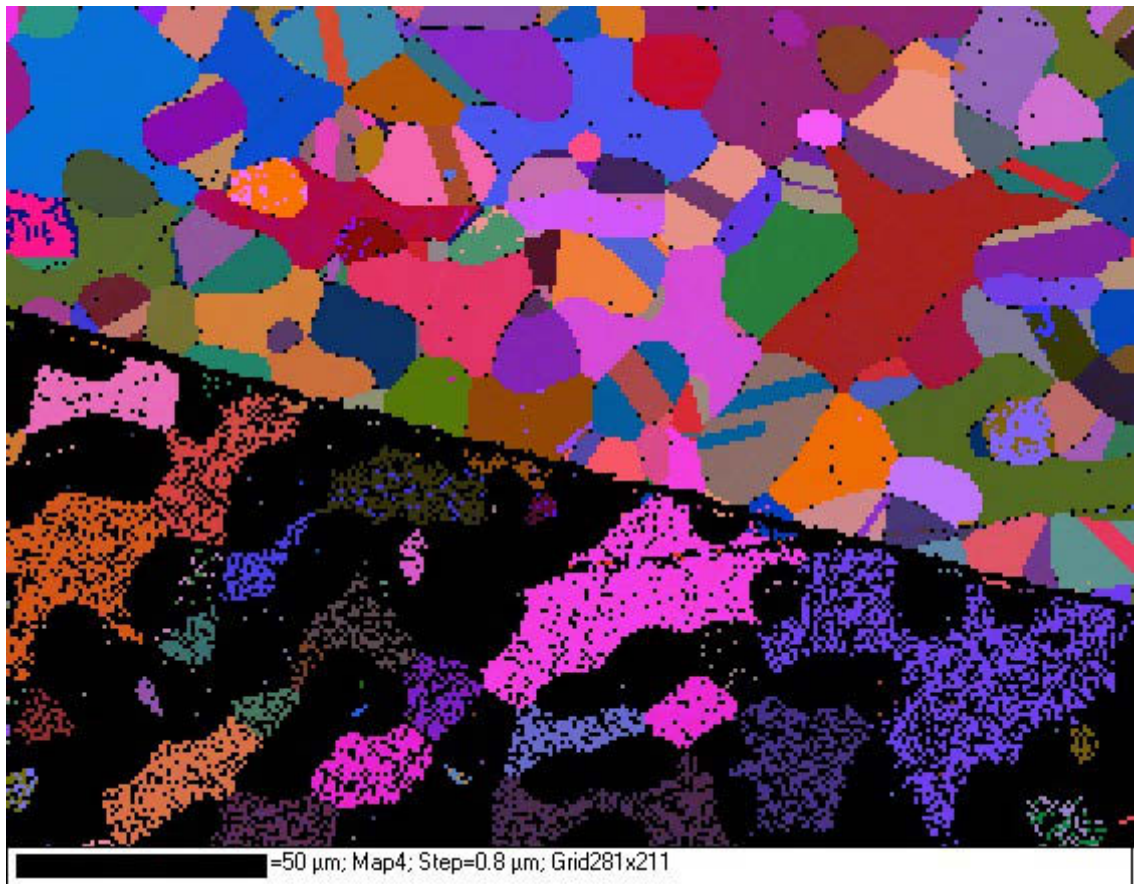


Figure 6-21: EBSD orientation map showing the partial or complete loss of pattern indexing from the grains in the irradiated region (lower half) of the 2205 grade steel.

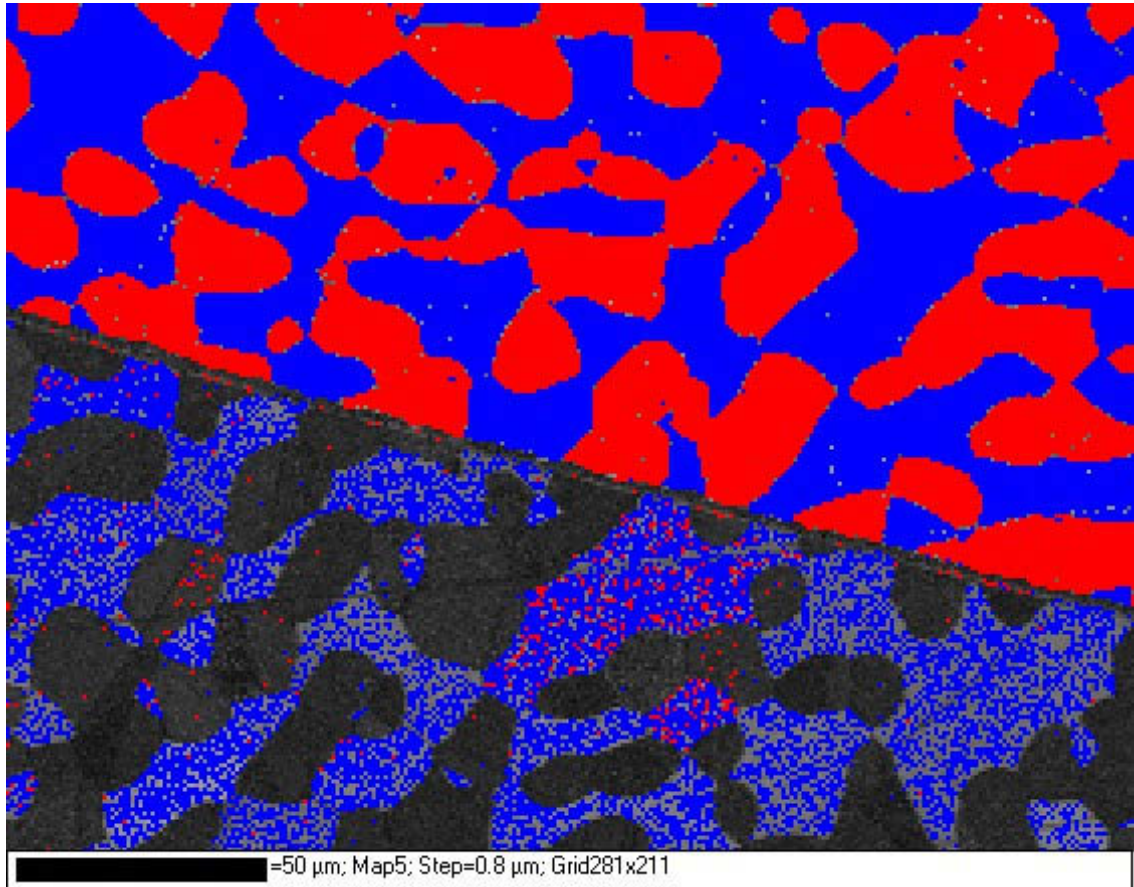


Figure 6-22: EBSD phase map showing the irradiated region (lower half) of the 2205 grade steel. The red colour is the FCC phase and the blue colour is the BCC phase. We can see that in the irradiated region (lower half) that the FCC phase was not able to be indexed however the BCC phase still shows partial indexing.

These results have confirmed the trend for the FCC metals to lose their ability to be mapped using EBSD post helium ion implantation with the BCC metals only suffering a partial loss of pattern. The results should also have implications for using EBSD in irradiation damage studies to reveal trends on large-scale area mapping.

6.4.4 Investigation of MA956 Grade Stainless Steel

MA956 grade stainless steel is another ferritic steel with the BCC crystal structure however it is unique in that it is an ODS material which has a nano-dispersion of oxide within its metallic matrix. It was now decided to repeat these experiments on this ODS material in order to answer the question, will we see something new by performing this experiment on a material that has been tailored specifically for use in the construction of nuclear reactors?

The MA956 steel was prepared in the same manner as the previous experiments before ion implantation was performed using both PI³ and the STAR accelerator on two separate pieces of metal.

Subsequent post-irradiation examination of the MA956 grade steel in the SEM using backscattered channelling contrast imaging and EBSD revealed similar results we had previously seen with the other grades of stainless steels. The backscattered channelling contrast imaging was still able to distinguish some grain boundaries and orientation contrast. The EBSD results were also revealing the same trend we had seen on the other ferritic steels with the BCC crystal structure, we were able to partially index the ion implanted region unlike the austenitic steels where indexing was not possible. Therefore the effect of the oxide dispersion in these materials was not able to be determined using these characterisation techniques.

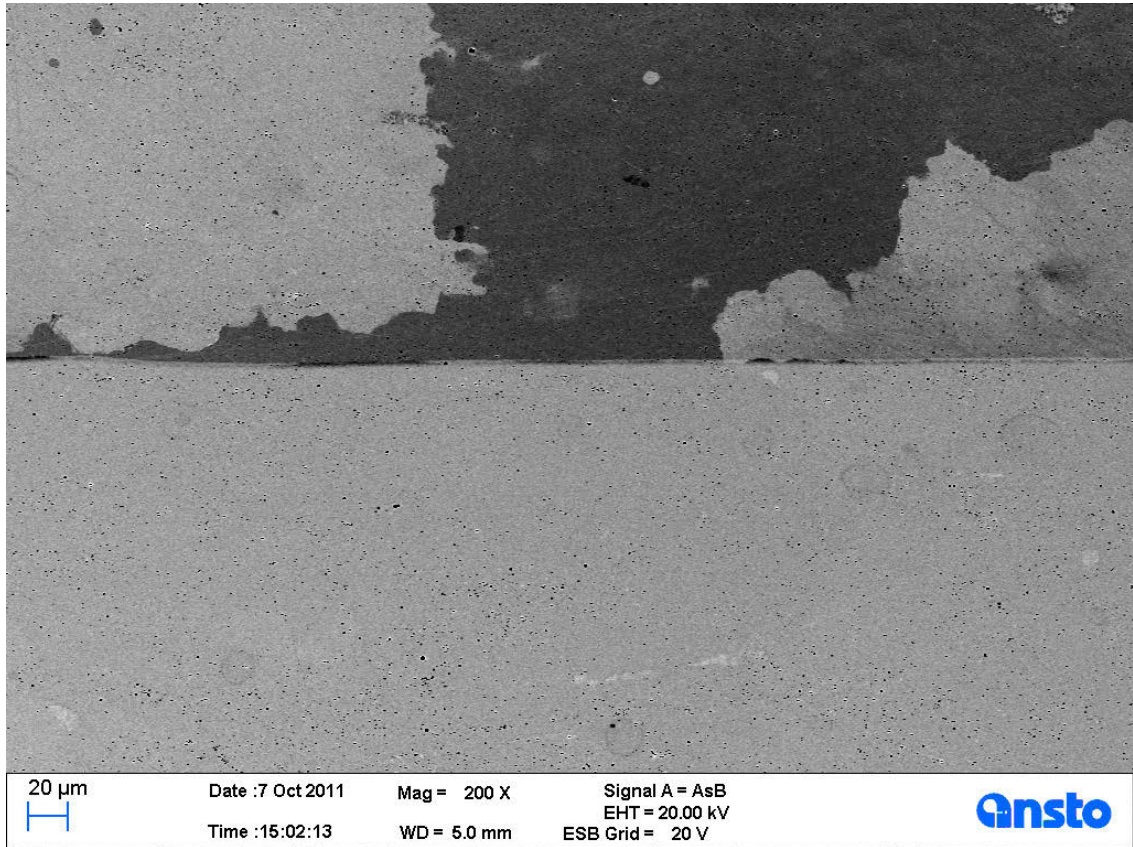


Figure 6-23: Backscattered electron channeling contrast image showing the irradiated (lower) and shielded region (upper) of the MA956 grade stainless steel. Helium ions were used for implantation.

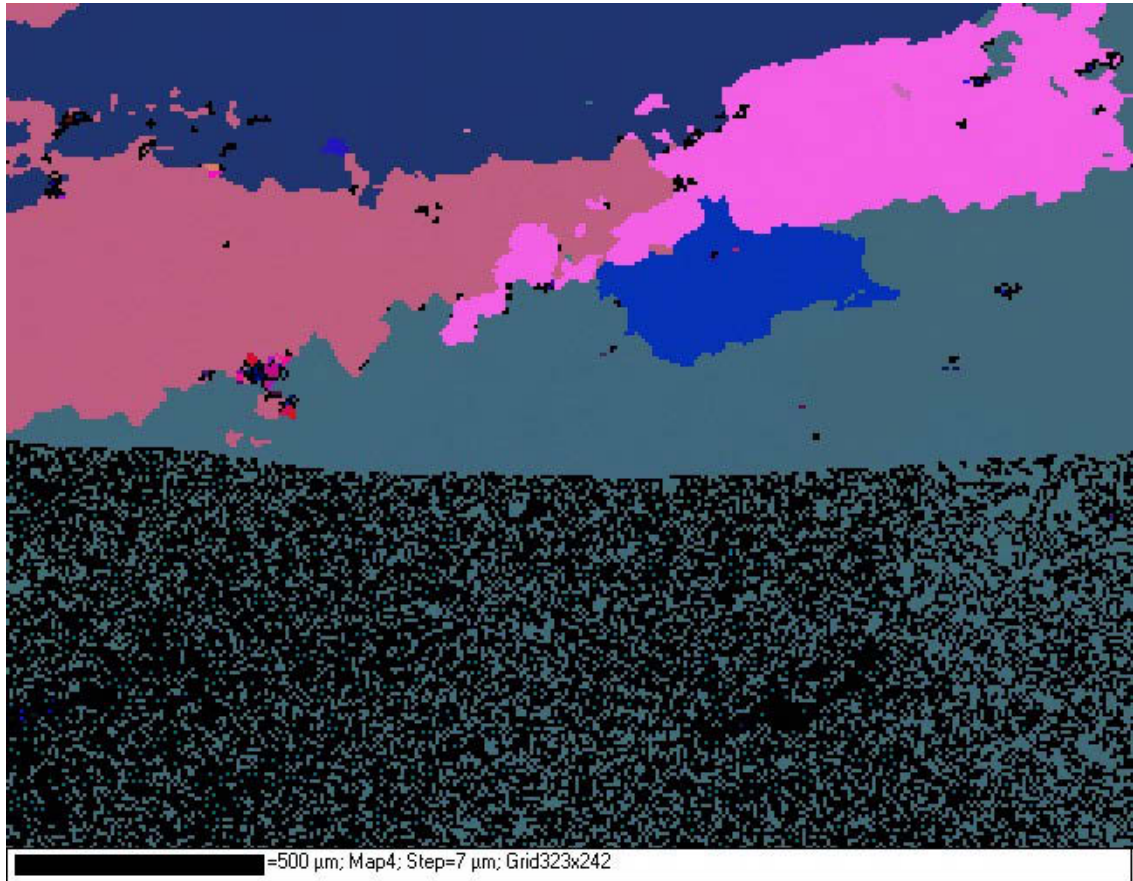


Figure 6-24: EBSD orientation map showing the partial indexing of the EBSD pattern in the irradiated region (lower half) of the MA956 grade stainless steel.

These results conclude the experiments done using backscattered electron channeling contrast and EBSD mapping on the materials irradiated in the PI³ using helium ions. We have confirmed the trend for the FCC metals to lose their ability to be mapped using EBSD post helium ion implantation with the BCC metals only suffering a partial loss of pattern.

As mentioned above, in these experiments we have also placed these materials in the STAR accelerator for implantation at a much higher energy. The following section will outline these results.

6.5 STAR Accelerator Results

The STAR accelerator uses much higher energy (5MeV) at a relatively low flux when compared to the PI³ accelerator. This high energy causes the ions to penetrate further into the material surface (~10 μm) leaving the material sample free from damage as confirmed by EBSD in the second initial experiment. Cross sections of the four remaining grades of steel which had been implanted to a fluence of $\sim 2 \times 10^{17}$ ions cm^{-2} helium ions have been prepared with a very high quality polish. These samples were then studied in the SEM using backscattered electron channeling contrast.

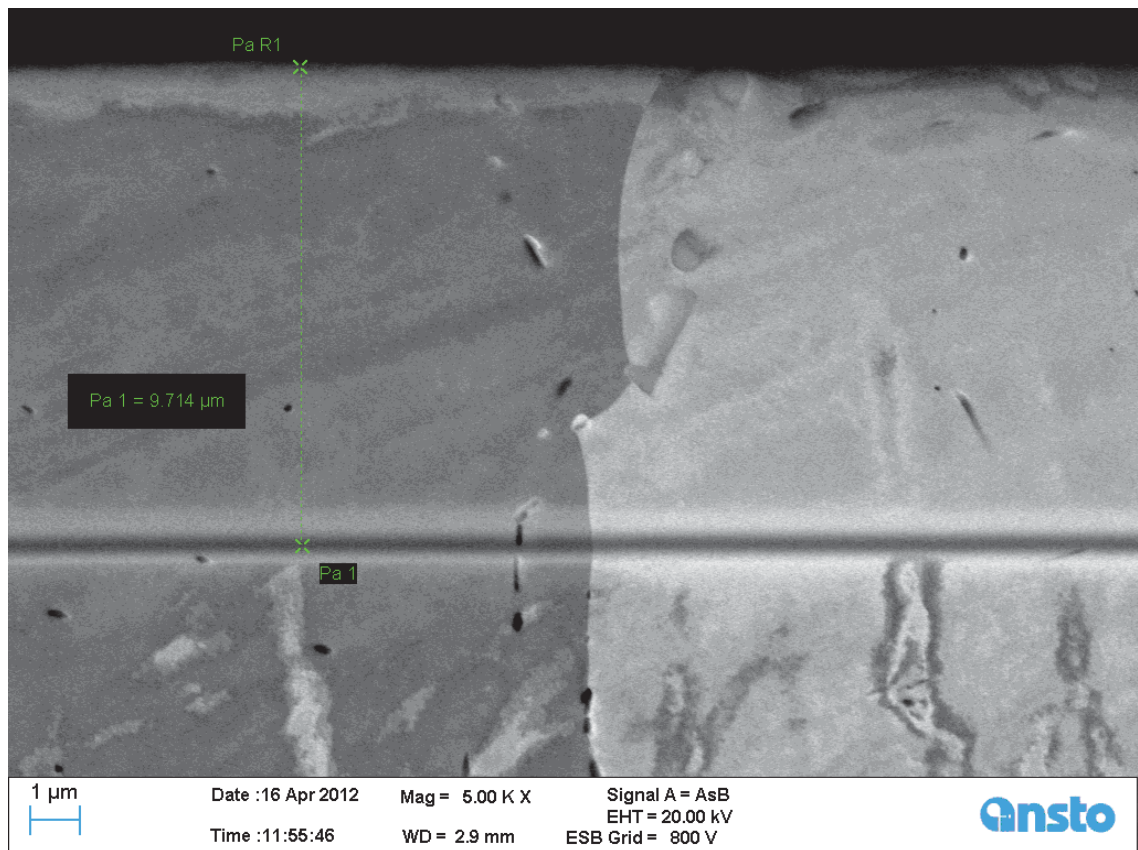


Figure 6-25: Backscattered electron channeling contrast image of the 430 grade steel showing the cross-section of the irradiated region and a line of radiation damage caused by the helium ions approximately 9.7 μm under the surface.

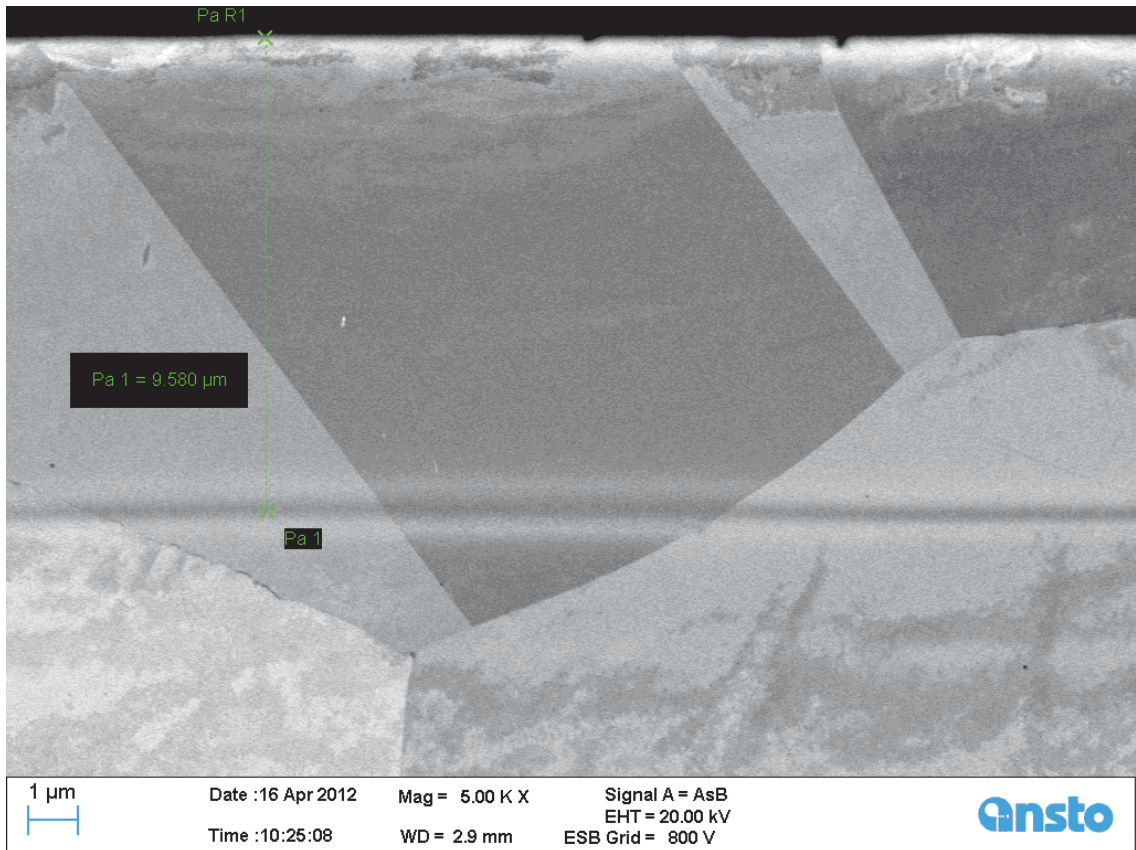


Figure 6-26: Backscattered electron channeling contrast image of the 304 grade steel showing the cross-section of the irradiated region and a line of radiation damage caused by the helium ions approximately 9.6 μm under the surface.

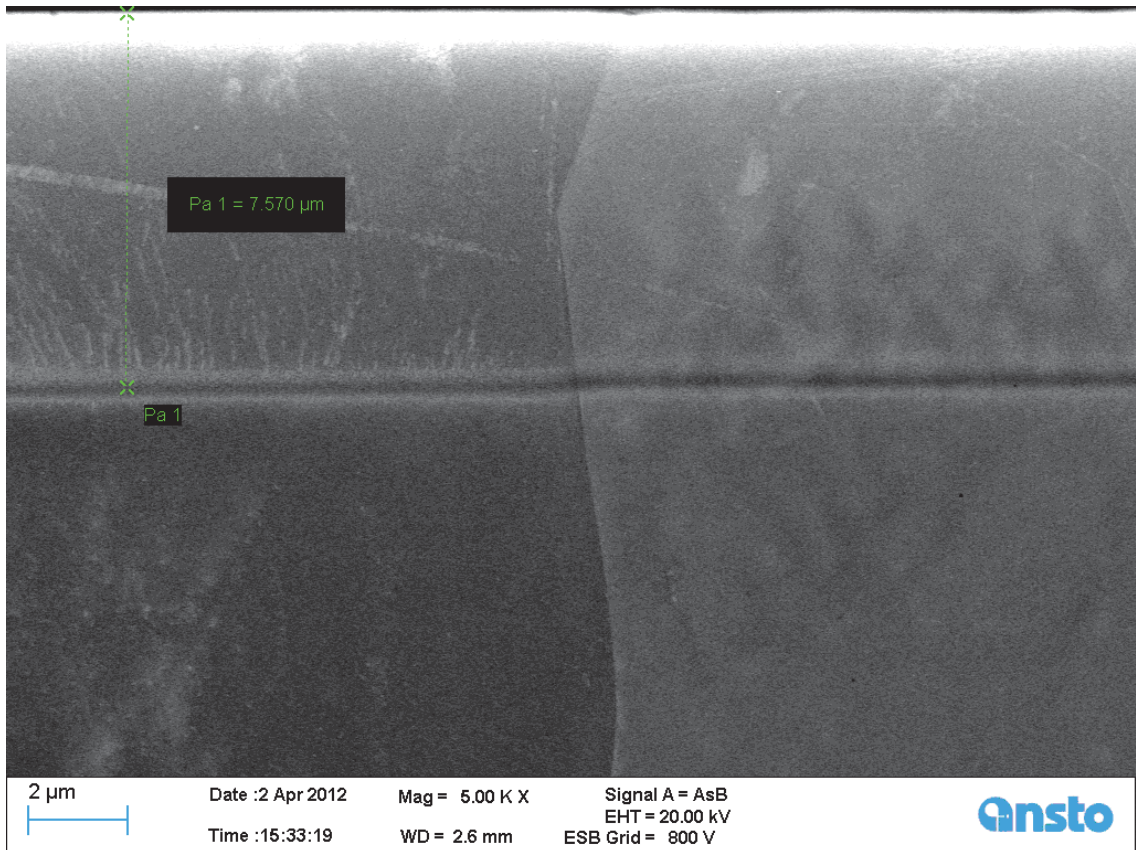


Figure 6-27: Backscattered electron channeling contrast image of the 2205 grade duplex steel showing the cross-section of the irradiated region and a line of radiation damage caused by the helium ions approximately 7.6 μm under the surface.

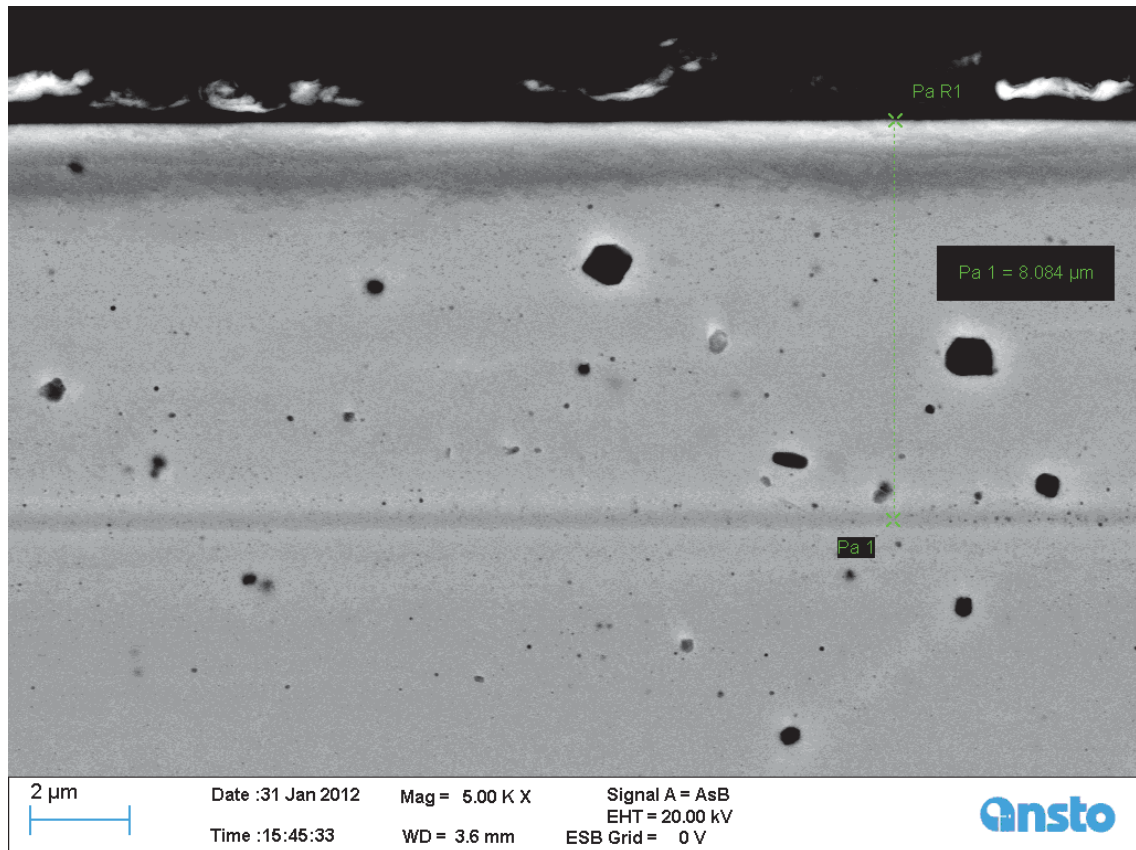


Figure 6-28: Backscattered electron channeling contrast image of the MA956 grade ODS steel showing the cross-section of the irradiated region and a line of radiation damage caused by the helium ions approximately 8 μm under the surface.

The backscattered channelling contrast results in the SEM are very similar for all the materials examined in these experiments. The crisp line of damage from the helium ions created with the STAR accelerator appears to be a similar depth for all four grades of steel tested. Slight changes in the damage depth will exist due to the differing composition of the steels and some orientation or channelling effects within the grains. This sharp line of damage occurs due to the energy of all the helium ions in the accelerator being the same energy when they penetrate the sample. The bulk of the damage occurs when the ions lose momentum and come to rest inside the crystal lattice of the steel.

6.5.1 Further investigation of the 2205 Duplex Steel

During the previous research using the PI³ accelerator we found the duplex stainless material to be great at revealing trends due to its combination of crystal phases in the

one material. It was therefore decided to take a closer look at the effects of the irradiation done using the STAR accelerator.

The backscattered electron channeling contrast images of the damage region done at high magnification reveal a slight change in damage depth at a grain boundary in the material. The resolution of the SEM is at the limit here and in order to study the defects in each phase in more detail a transmission electron microscope (TEM) would be required.

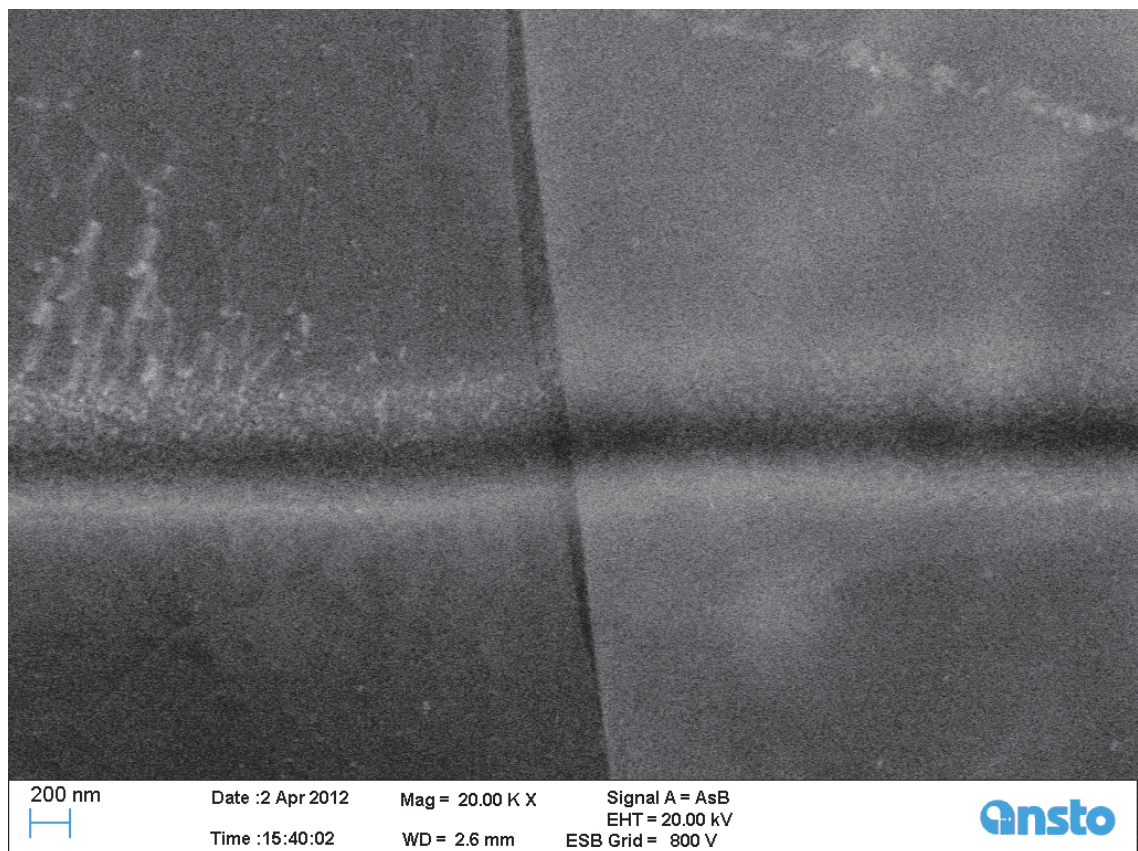


Figure 6-29: Backscattered electron channeling contrast image of the 2205 grade duplex steel at high magnification showing the damage region caused by the helium ions at a grain boundary.

EBSD mapping of this grain boundary was then performed to see if the grain boundary shown was a boundary between the FCC and BCC crystal phases. Subsequent X-Ray mapping was also performed to determine the composition of the two grains.

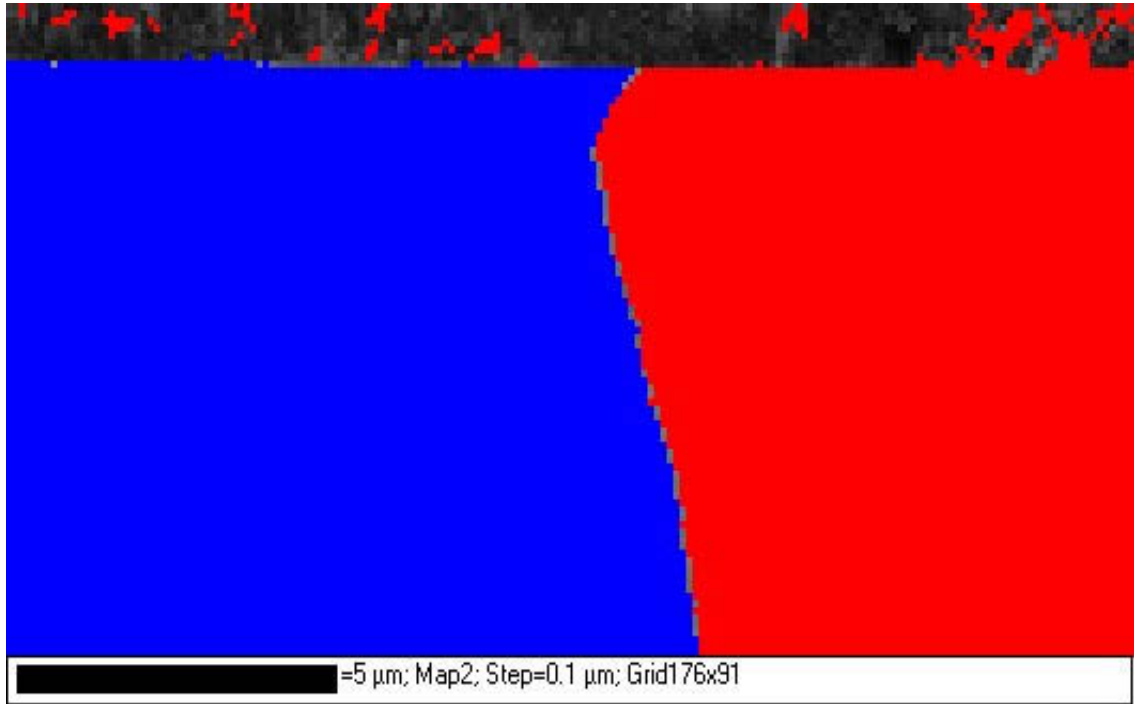


Figure 6-30: EBSD phase map of the cross section of the 2205 grade duplex steel grain boundary region showing the BCC phase in blue on the left grain and the FCC phase in red on the right grain.

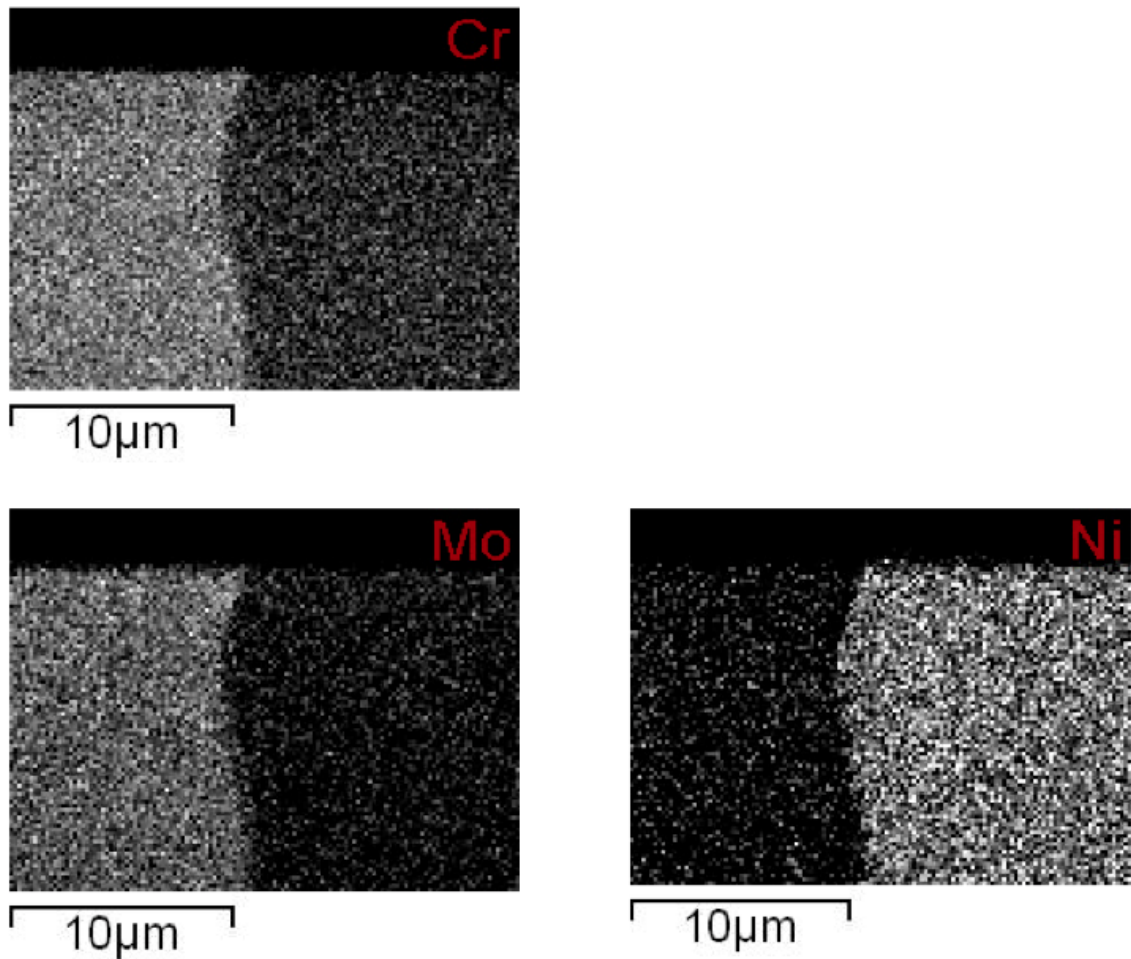


Figure 6-31: X-ray mapping of the cross section of the 2205 grade duplex stainless steel showing the corresponding grains as seen in figure 6.30. The X-ray mapping shows which elements are specific to the BCC and FCC phases.

It was not possible to determine if the change in depth for the damage layer was a result of composition, crystal phase, crystal orientation or simply polishing relief at the grain boundary from the pre-irradiation sample preparation. To further study the effect of radiation damage on the material it was decided that the broad damage layer resulting from the PI³ accelerator would give us a better chance to examine the region in cross section than the thin crisp damage layer formed by implantation in the STAR accelerator.

We also need to confirm whether what we had been seeing with the loss of EBSD pattern in plan view would also be observed in the cross section. For this purpose a broad damage layer would be much more suitable than a thin crisp line for EBSD mapping.

Ultimately using high-resolution transmission electron microscopy would be the best technique to see the concentration of defects in each phase once the EBSD technique had been tested.

6.6 Cross-section Method Development for Shallow Damage Layers

The shallow nature of the radiation damage (< 100 nm, see figure 1.) caused by the PI³ accelerator created a new challenge for the preparation of cross sections adequate for EBSD mapping. Traditional methods involve mechanical polishing, large-scale ion beam polishing in a standalone device or targeted small-scale ion beam polishing in a focused ion beam (FIB).

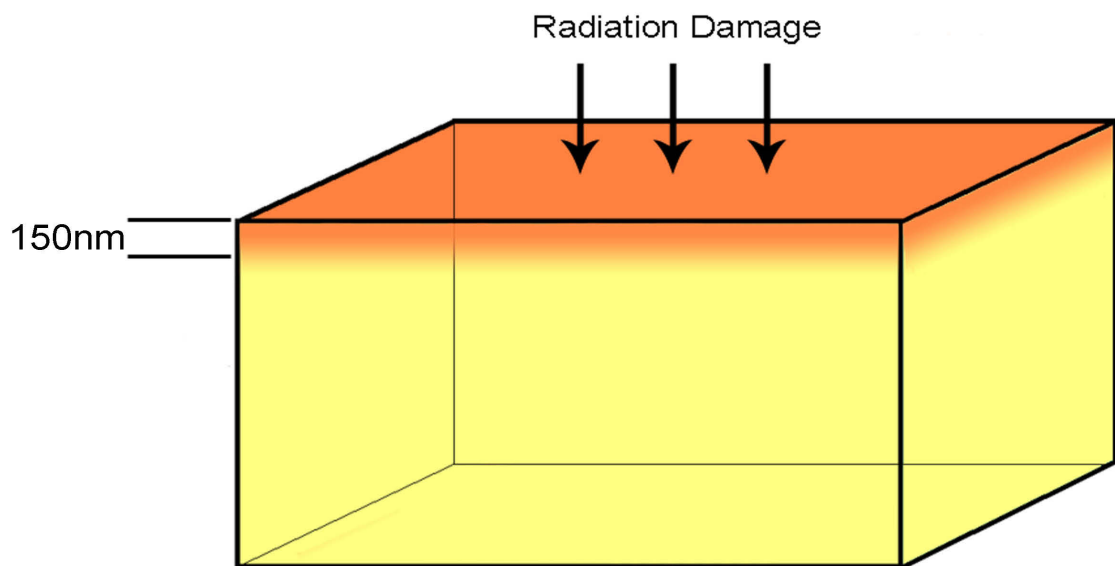


Figure 6-32: Illustration demonstrating the Stopping Range of Ions in Matter (SRIM) calculations put the expected peak damage layer at a depth of ~ 150 nm for 316 stainless steel.

6.6.1 Mechanical Polishing

Mechanical polishing for EBSD has been previously performed successfully on large area plan view sections of material using the Struers method for polishing Low Carbon Steels (Method No. 1879). An attempt was made to prepare the cross sections using this method by first cutting the sample to reveal the cross section of interest and then bonding the two faces together before polishing in an attempt to limit edge rounding.

Edge rounding using this method was in the order of several hundred nanometers, which was well beyond the area of interest we had calculated, using SRIM, see figure 6.33.

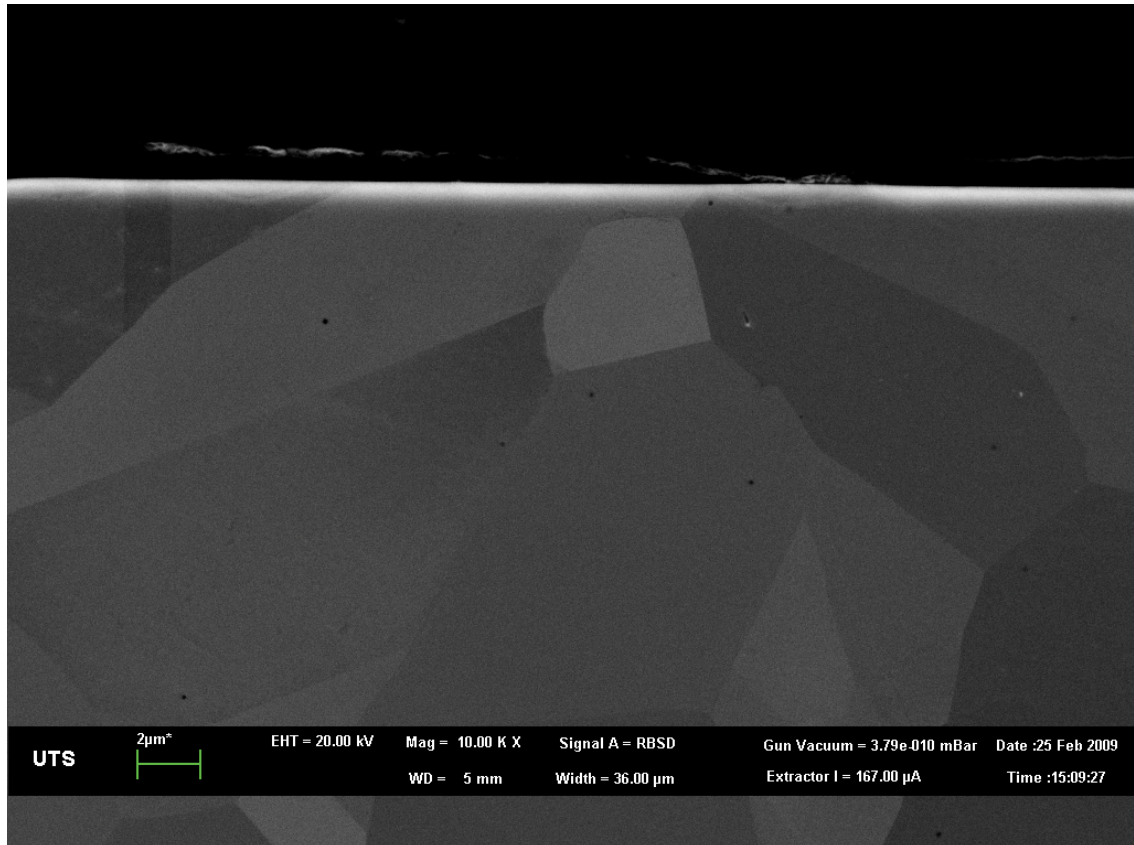


Figure 6-33: The result of mechanical polishing of the cross sectioned stainless steel samples showing edge rounding well beyond the 100nm below surface area of interest. The area above the steel is an epoxy resin which is much softer and allows for the polishing rate to differ causing the rounding of the stainless steel edge.

6.6.2 Large-Scale Ion Beam Cross Sectional Polishing

Another technique available to us was ion beam polishing using a JEOL SM-09010 cross section polisher. The instrument works by placing the sample in a broad beam of argon ions under vacuum with a shielding material above the sample to prevent milling of the top surface, see figure 6.34.

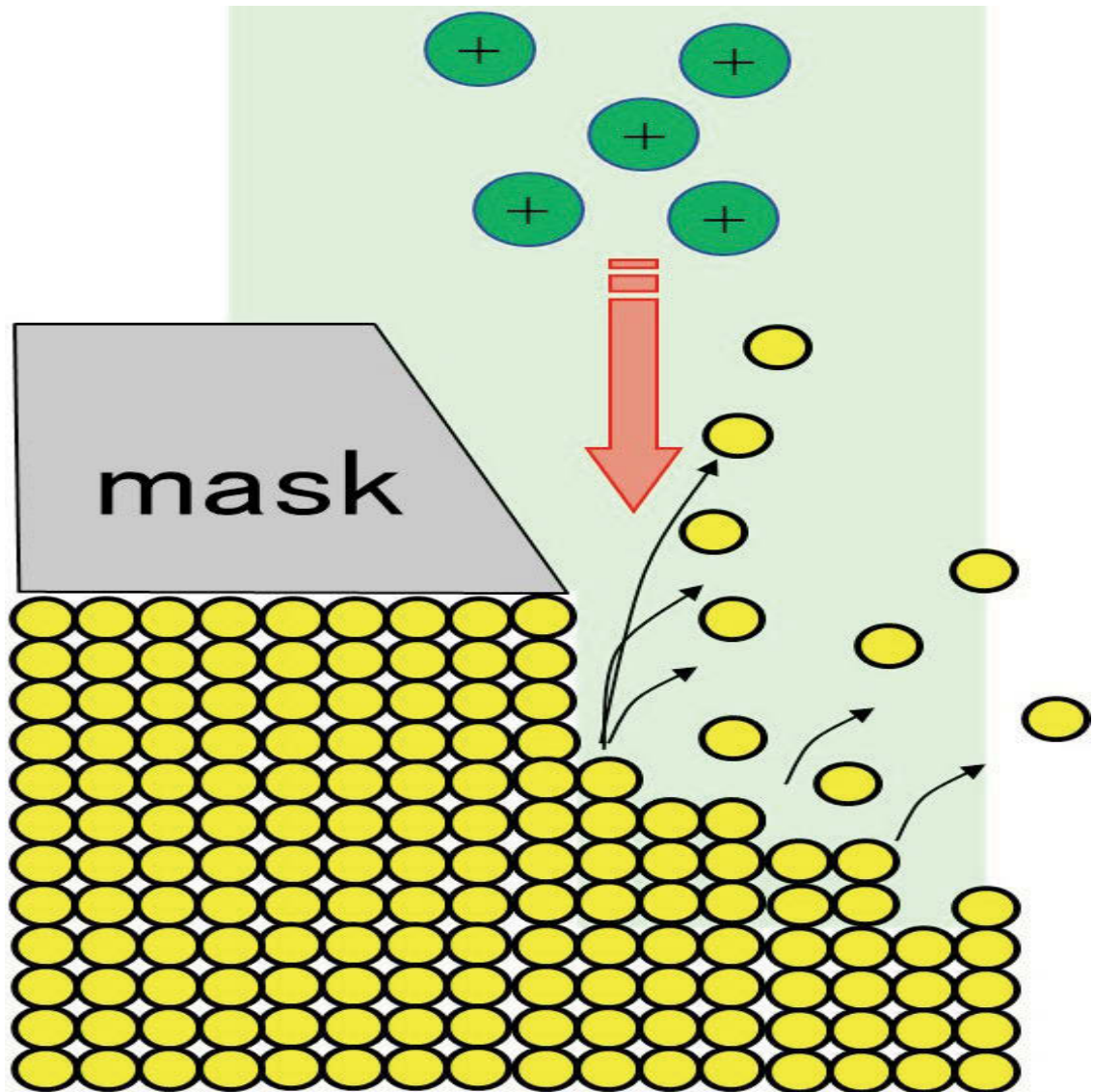


Figure 6-34: Schematic diagram showing the method of polishing performed in the large scale ion beam cross sectional polisher. [Hitachi High Technologies America, Inc. 2015]

In order to perfect this technique a number of un-irradiated or blank samples were first polish until we could achieve the results required for EBSD mapping of the cross section with the sub 100 nm area of interest still intact. The instrument allows the user to choose milling times and beam currents to get the required results. Figure 6.35 shows a blank sample we prepared in this instrument with the desired edge retention.

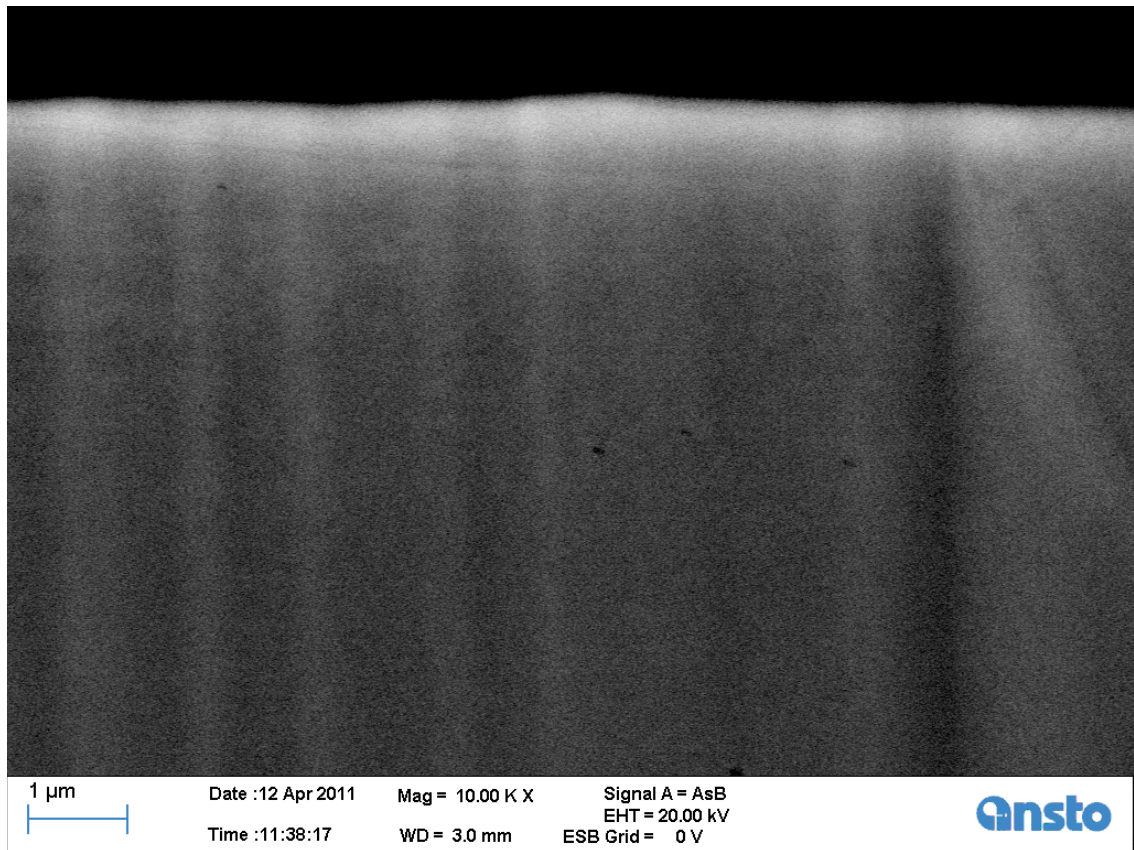


Figure 6-35: Blank stainless steel sample prepared using the JEOL cross sectional polisher with edge retention in the sub 100nm region.

Despite successful trials, reproducible results could not be achieved using the JEOL SM-09010 cross-section polisher. After a number of failed attempts it was decided to move onto a new technique.

6.6.3 Cross Section Preparation Using Focused Ion Beam

The focused ion beam (FIB) is a powerful tool for doing targeted milling of samples although it is generally used on smaller areas than what we were working with in this research. Access to this equipment is difficult as the technique is very time consuming and the instrument itself very expensive and therefore in high demand. We only required one sample to prove our concept so it was decided to try and secure some FIB time at a local university. The instrument used was an older FEI model and we were able to mill significant amounts of material away to make our cross section in the allotted time. However, sample drift was found to be a significant problem and it became clear this technique was not appropriate given the amount of time we had available for this project. A partially milled sample is shown in figure 6.36.

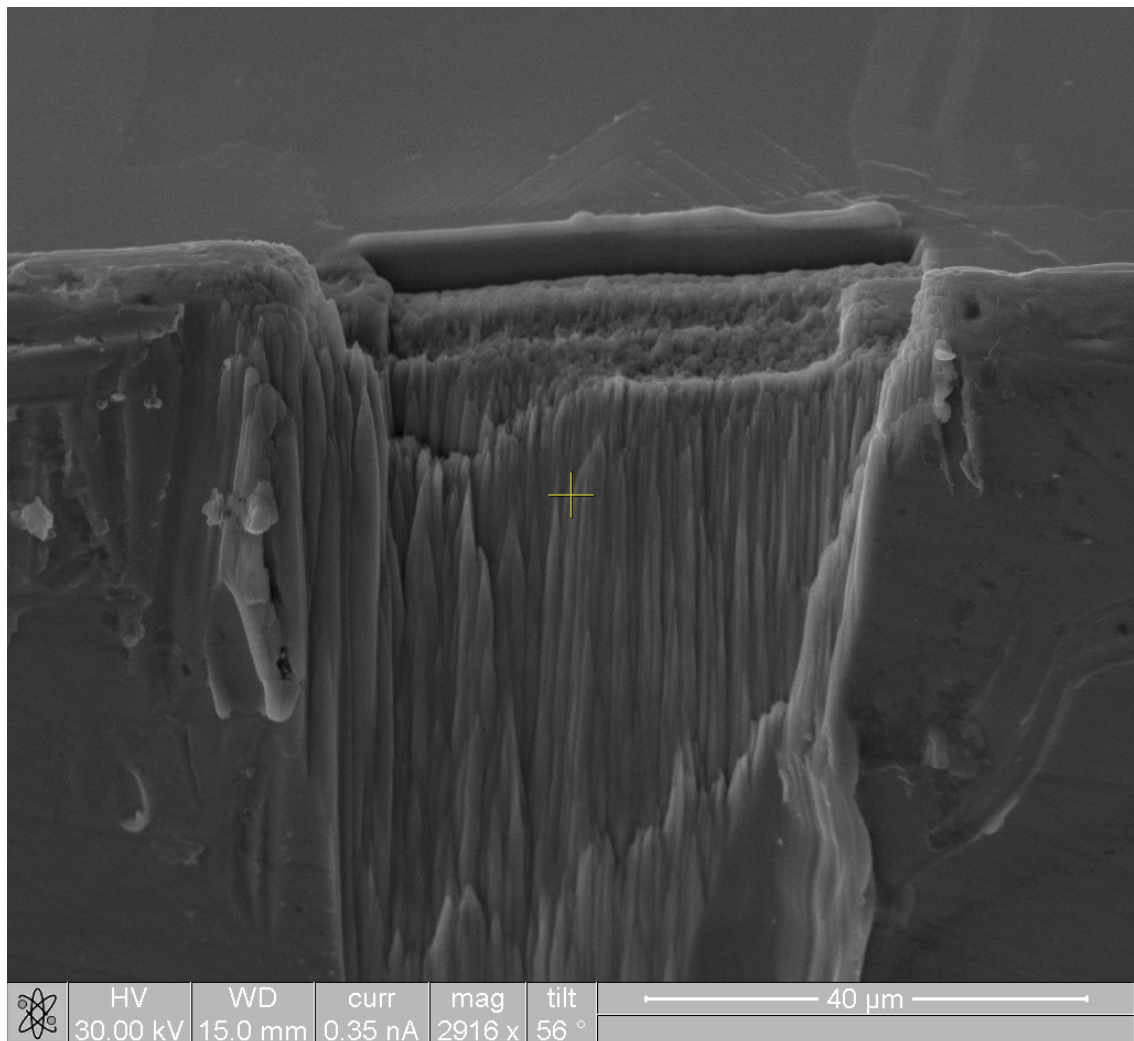


Figure 6-36: SEM image of the partially milled cross section using the focused ion beam.

6.6.4 Cross Section Preparation Using Precision Ion Beam Polishing

Precision ion beam polishing (PIPS) using an argon ion beam at a shallow angle under vacuum on a rotating stage to remove material, see figure 6.37. This technique is traditionally used for preparing thin sections for transmission electron microscopy (TEM). However, we were able to mount the cross section such that it would be polished by the ions in a direction moving away from the top surface to reveal a highly polished face with minimal edge rounding, see figure 6.38.

The method for this successful use of PIPS first involved cutting the sample in half with a Buehler ISOMET low speed saw fitted with a Buehler wafering blade. The two halves

of the sample were then bonded together using a G1 epoxy kit and placed on a hot plate to cure under pressure from a spring-loaded press.

Once cured the sample was placed in a Gatan disc grinder (623) to get a flat even face on both sides of the cross-section. The sample must be ground down and polished until it is approximately 1.48mm thick so once in the custom Gatan PIPS holder the total height is approximately 2.55mm.

Grinding/Polishing paper grades are used in the following order: 500, 800, 1200, 2400 and 4000.

The PIPS was then run at 5 keV with 4° tilt for 6 hours. Then at 4.5 keV with 3° tilt for 3 hours then finally 4 keV at 3° tilt for 1 – 2 hours.

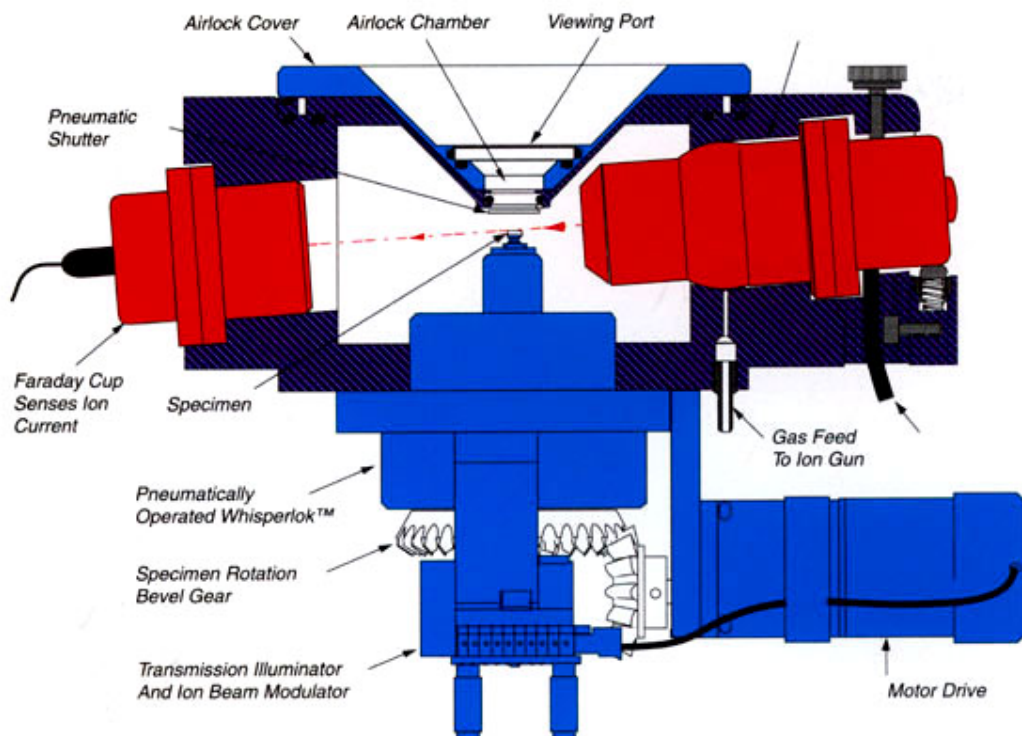


Figure 6-37: Schematic diagram of the PIPS instrument [Gatan Inc.]

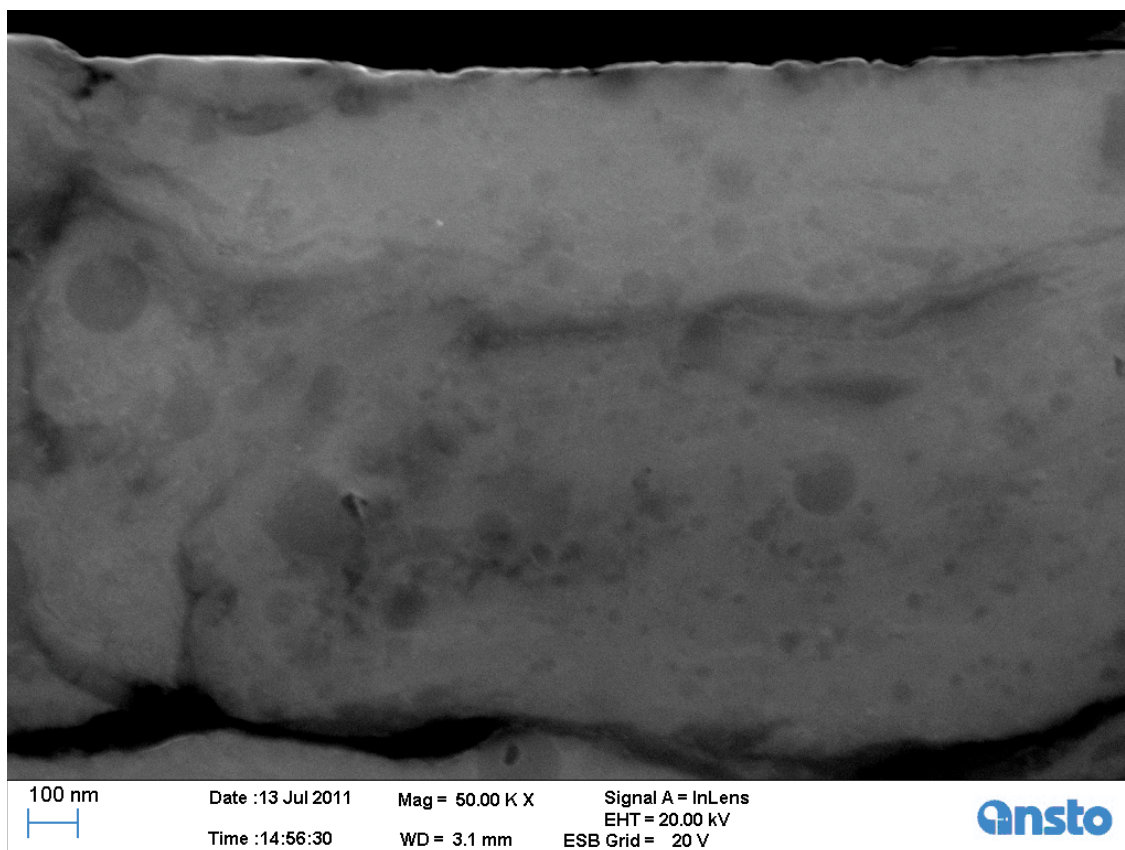


Figure 6-38: Precision ion beam polished cross section of the 316 stainless steel un-irradiated test sample showing excellent edge retention in the sub 150nm region.

After completing a successful trial we were then able to replicate the result on a real sample that had been irradiated with helium ions as per the plan view studies.

6.6.5 EBSD study of irradiated 316 stainless steel cross section

Using the PIPS method summarised above the cross section of a piece of 316 stainless steel which had been previously ion implanted in the PI3 to a dose of 1×10^{17} He ions/cm³ at 30 keV was polished for EBSD mapping.

Initial investigation of this sample with backscattered electron channelling contrast revealed a change in contrast in the expected damage region, see figure 6.39. This was expected as changes in contrast had been previously observed with the plan view samples.

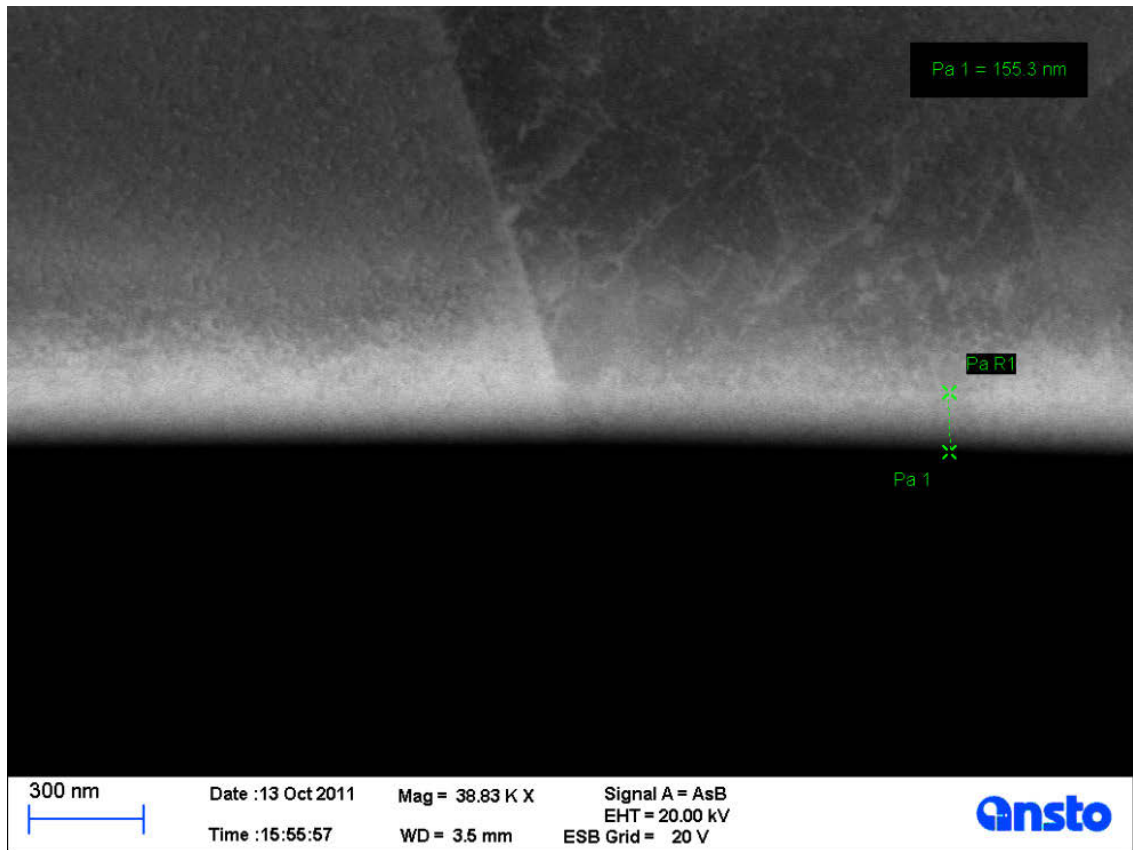


Figure 6-39: Backscattered electron channelling contrast image showing the helium ion implantation damage layer in the PIPS prepared cross section with a depth that agrees with SRIM calculations.

The sample was then mapped with EBSD, see figure 6.40. The results from the EBSD map of the cross section reveal the same trend as seen in the plan view samples that had been implanted in the same manor. A partial loss of pattern indexing was found in the damage region that compares well with the observed depth calculated using SRIM and the contrast shown in the backscattered electron channelling contrast image above. We can also see in the orientation map there is a colour change in the damage layer that corresponds to a slight change in crystal orientation (3 – 5 degrees) with respect to the parent metal underneath. Point defects and vacancies by the atomic displacement of atoms during ion implantation result in the formation of many dislocations throughout the damage layer. These dislocations formed give us this slight change in crystal orientation observed. Consequently it can be confirmed that the observations made in plan view with respect to the loss of indexing in the damage region are not simply a result of a sputtering effect and the damage is occurring throughout the entire damage layer. The next step is to study this damage layer in higher resolution using transmission electron microscopy.

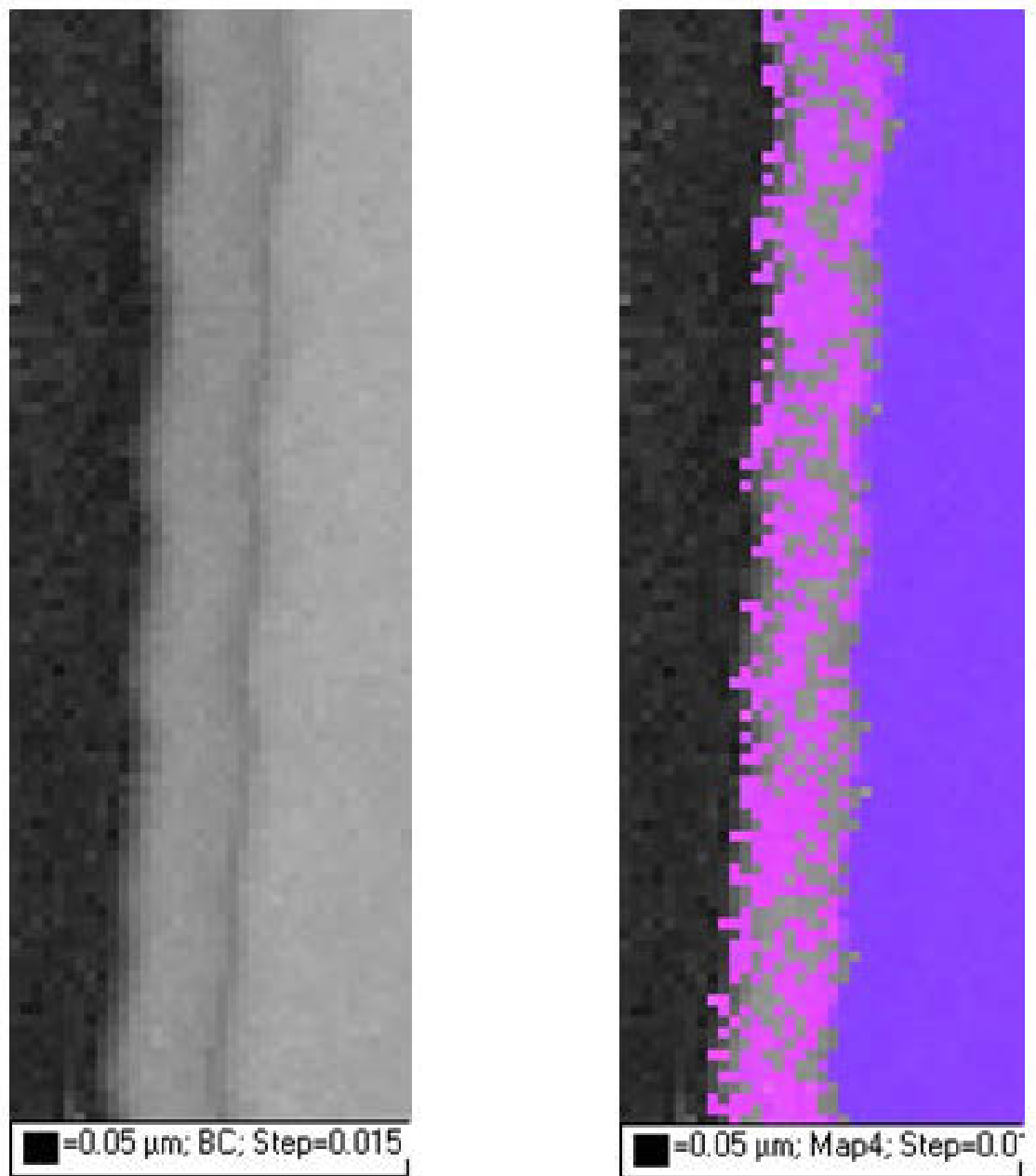


Figure 6-40: EBSD band contrast map (left) and orientation map (right) of the cross section showing a partial loss of indexing in the damage region.

6.7 Sample Preparation for Transmission Electron Microscopy

Transmission electron microscopy (TEM) allows the study of the damage region in the PI³ implanted steel cross section in very high resolution compared to SEM. In order to observe the sample in the TEM we require the material to be very thin (~50 nm) to

allow the electrons to transmit through and form an image on the screen. There are several techniques available for TEM sample preparation, some of which we have already used in this research when preparing the cross sections for EBSD. This next step, however, is even more difficult with the edge retention still being the major factor however now we need the sample to be thinned to 50 nm in the other plane.

The only technique really capable of such precision is the focused ion beam (FIB). The FIB will also allow us to target a specific grain boundary and thus it was decided to use this method on the duplex steel in an attempt to make a cross section containing a grain boundary between the FCC and BCC phases. This would offer a very unique opportunity to study the damage behavior of the two phases side by side in the one sample.

Careful planning was done in order to determine the location of each phase first in plan view using EBSD to map a select area of grains, see figure 6.41. Once the positions of each phase were known the sample was then transferred into the FIB in order to mill a trench across the grain boundary of interest. Once in position the standard method for TEM sample preparation was used to remove the cross section containing the grain boundary. This involves firstly depositing a 20 x 2 micron rectangular layer of protective platinum above the area in which we do not want to mill with the ion beam. Coarse milling of a trapezoidal shaped trench is then performed on both sides of this platinum layer, the trench is first milled at 30 kV 16 nA and then a rectangular shaped cleaner pass is done using 30 kV 2 nA to form the final shape before lifting out. A “u” cut is then made at a shallow tilt angle in order to free the bottom and sides of the lamella. The lamella is then lifted out *in situ* with a needle and welded onto a TEM copper grid for further thinning.

Several attempts were made to complete this sample due to the difficult nature of preserving the top 100 nm damage layer underneath the protective platinum whilst thinning the sample all the way down to 50 nm. The method, which worked in the end, was a result of bottom up thinning with the lamella positioned 2 degrees off the axis of the ion beam on each side.

The final polishing steps are done at 30 kV 120 pA and then dropping down to 15 kV 80 pA to remove the damage created by the 30 kV gallium ions. Finally a long 2 kV 20 pA polishing pass is done on each side at six degrees off milling access to remove any further damage created by the 15 kV gallium ions.

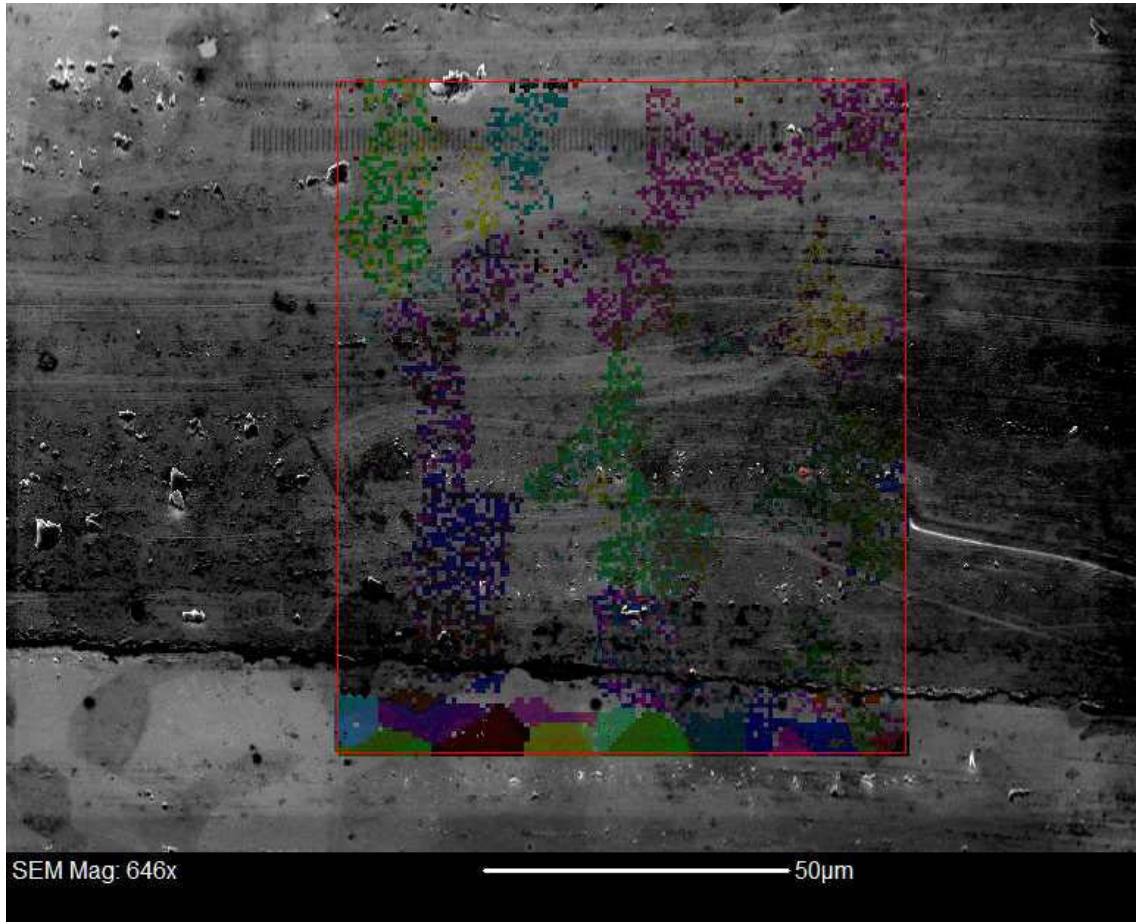


Figure 6-41: EBSD map of the area in the irradiated region to determine the grain boundary of interest prior to FIB milling.

6.8 Transmission Electron Microscopy Results

The FIB prepared TEM sample was examined in a JEOL 2200 TEM at 200 keV using the scanning transmission electron microscopy (STEM) mode and bright field image detection. Figure 6.42 shows a low magnification STEM image of the FIB prepared cross section showing the grain boundary of the helium implanted duplex stainless steel with the BCC phase in the lower region and the FCC phase in the upper region. Note the first three layers are the protective platinum layers that were deposited in the FIB to

protect the material surface during milling. The thicker (~160 nm) and darker grey region below this is the damage layer from ion implantation.

High magnification bright field TEM images (Figure 6.43.) reveal point defects, defect clusters and voids that have formed in the damage layer (~140 nm). Using Fresnel-fringe contrast we can distinguish between features that may be either voids or point defects in the damage layer. This technique, which is demonstrated in figure 6.44, involves taking images in an under-focus and over-focus condition. If a feature contains a bright spot in the middle surrounded by a dark ring when imaged in an under-focus condition and this same feature also exhibits a black dot in the middle and a bright ring surrounding it when imaged in the over-focus condition then it is considered a void. If this condition is not met and the feature is a dark or black spot under both imaging conditions then the feature is most likely a point defect and larger dark regions are considered to be defect clusters [58].

Comparing the amount of defects and clusters using TEM in the BCC and FCC phases a clearer understanding of the EBSD mapping results performed in the earlier experiments is obtained. The FCC phase (top), which could not be indexed, contains a much higher concentration of defects when compared to the BCC phase (bottom), which could be only partially indexed with EBSD. It is clear that the number of defects present directly affects the sample's ability to diffract electrons and form the Kikuchi patterns required for EBSD mapping. This observation agrees with several studies from the literature for ion implantation or neutron irradiation studies in metals that show a lower tolerance to radiation damage for FCC metals when compared to BCC metals [40, 59, 60]. When subjected to neutron or ion irradiation FCC metals have been shown to form large dislocation clusters which can lead to the formation of stacking fault tetrahedra even at low doses. The mobility of these dislocation clusters is determined by the stacking fault energy (SFE) [60 - 61]. Work by Michael [62] has shown that ion beam irradiation can cause significant microstructural changes in FCC metals with fine grain structure. Changes include new grain formation in the channeling direction parallel to the ion beam, however no changes were observed in the BCC metals.

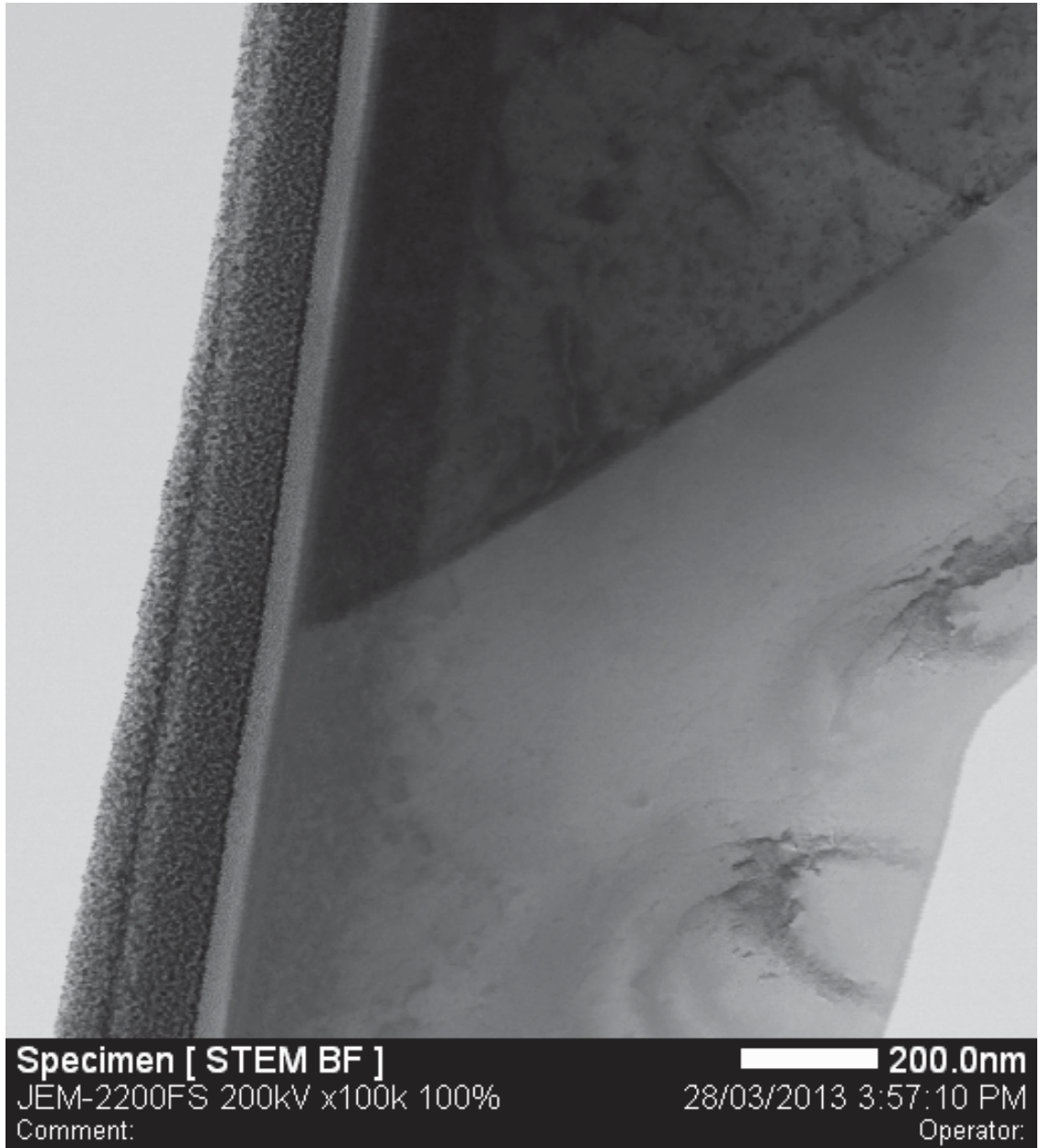


Figure 6-42: Low magnification STEM image of the FIB prepared cross section showing the grain boundary of the helium implanted duplex stainless steel. BCC phase is the lower region; FCC phase is the upper region.

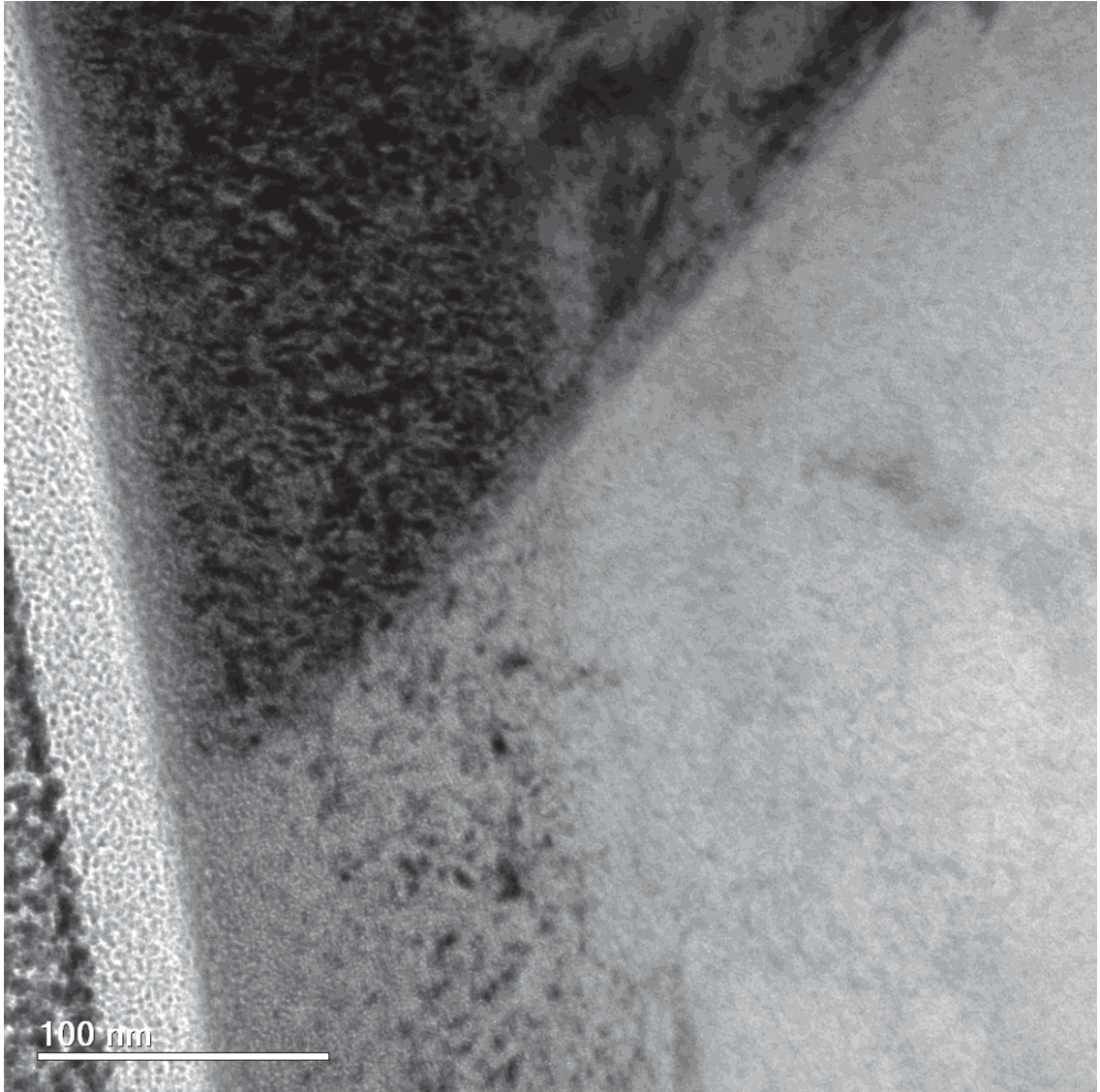


Figure 6-43: High magnification TEM image showing the grain boundary between the two phases. We can see in this image the significant increase in the amount of defects in the FCC phase compared to the BCC phase.

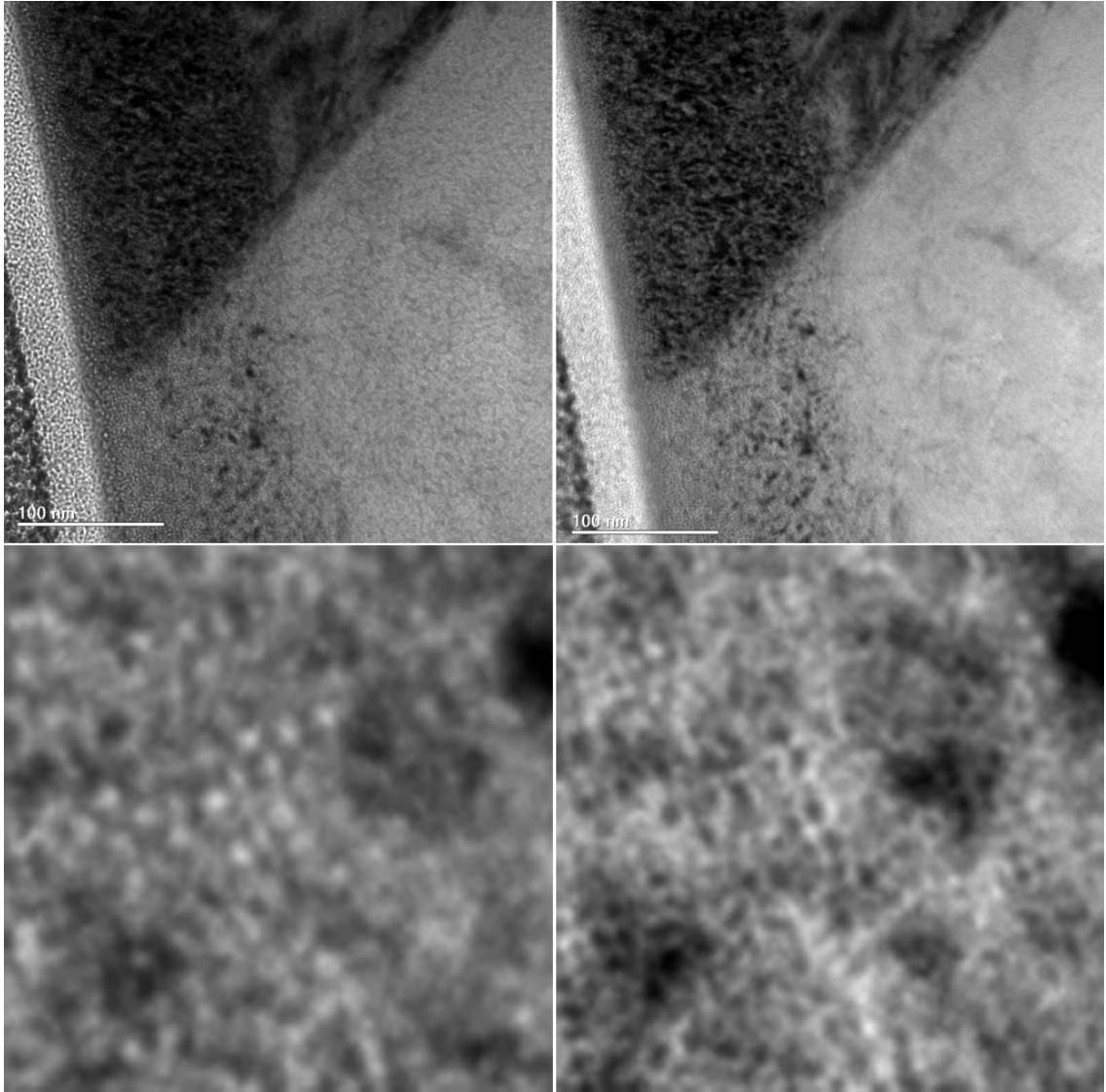


Figure 6-44: TEM images of the grain boundary between phases shown in under-focus (left) and over-focus (right) condition. The lower images are digitally blown up regions of the corresponding images above for ease of viewing. Fresnel-contrast imaging is used to reveal the voids and point defects in the damage layer.

6.9 CHAPTER CONCLUSION

In this chapter the veracity of the research was demonstrated. These experiments paved the way for an extended experimental program on a larger suit of stainless steel materials. The experimental work revealed interesting trends in the material's behaviour under a radiation damage environment. Furthermore electron microscopy techniques were devised that may have implications for future reactor material design and research. These novel techniques developed throughout this project using backscattered electron channelling contrast and electron backscattered diffraction mapping have been validated

in this final chapter with the use of transmission electron microscopy contrast mechanism imaging.

7 CONCLUSIONS AND FUTURE WORK

The purpose of this work has been to gain an understanding of the radiation damage tolerance of structural reactor materials and ideally fill a gap in the knowledge base in the use of scanning electron microscopy based techniques to characterise this radiation damage.

Initial experiments were conducted on a 316 grade stainless steel to determine a methodology for ion implantation and characterisation of the damage. The use of backscattered electron channelling contrast as a means of identifying large areas of damage in the stainless steel surface in plan view was used and atomic force microscopy results confirmed that this result is not simply due to the sputtering away of the highly polished sample surface. Subsequent electron backscatter diffraction mapping of these large areas in plan view showed a potential for a novel use of this technique as a means of mapping large areas of radiation damage. Previous radiation damage studies using this technique have only been performed as a bulk mechanical property measurement as discussed in the literature review. An understanding was then gained in EBSD sample preparation conditions for cross sectional samples with minimal edge rounding in the sub 100 nm range. These methods were very difficult to develop, however, they were essential for imaging the very shallow radiation damage caused by charged particle implantation at low energies. Results from the initial experiments lead the way for an expanded study on a suite of stainless steel grades with current and future implications as structural reactor materials.

The key result from the EBSD mapping studies of the other stainless steel materials was the revealing of a trend for the FCC iron phase to be less tolerant to ion implantation when compared to the BCC iron phase in the duplex stainless steel. This trend was then confirmed throughout the depth of the radiation damage layer by preparing cross-sections for subsequent EBSD mapping using the previously developed sample preparation methods.

The next key step was to prepare a cross sectional sample of this duplex steel material which encompassed a grain boundary between the FCC and BCC crystal phases. The intention of this sample preparation was for using transmission electron microscope contrast mechanisms to image the defects present in each phase along the grain

boundary and confirm the results found using EBSD mapping of the plan view and cross-sectional irradiated steels.

The TEM results showed a much higher concentration of defects in the FCC phase compared to the BCC phase, this was expected based on the EBSD mapping results. In the literature review we have discussed some of the damage mechanisms inherent in ferritic (BCC) and austenitic (FCC) steels when exposed to a radiation damage environment. Neutron-induced void swelling in relatively large amounts even with moderate doses and low thermal conductivity coupled with phase segregation and phase stability issues are the key areas affecting austenitic steels [10, 28]. Ferritic steels offer some improvements over austenitic steels with regard to void swelling and the addition of oxides in the ODS materials have vastly improved their high temperature performance. The ferritic steel lattice is well understood and the mechanisms in which point defects interact with dislocations for microstructural stability have been extensively investigated in the literature [30, 31].

With the damage mechanisms of ferritic and austenitic steels noted as being well understood there is no specific need to further characterise the nature of the point defects and dislocations in the TEM prepared duplex stainless steel sample. Future work however would best be based around further development of the EBSD mapping techniques on other candidate reactor materials and possibly exploring the use of high-resolution transmission EBSD mapping of the damage region in the TEM prepared duplex steel sample.

There is also scope for the development of surface treatments of the austenite materials and many other materials found to be more susceptible to radiation damage. The EBSD technique developed in this research could be employed to assess the merit and further develop these treatments alongside the traditional methods also employed in this research. The highly developed methods for the sample preparation of cross-sections used in this research would also be of valuable use in this future work.

REFERENCES

- [1] The First Reactor, U.S. Dept of Energy (1982).
- [2] D. Okrent, Nuclear Reactor Safety, The University of Wisconsin Press (1981).
- [3] Nuclear Reactor Analysis, J. J. Duderstadt, L. J. Hamilton, J. Wiley & Sons, Inc. (1976).
- [4] C. R. F. Azevedo, Eng. Failure. Analysis 18 (2011) 1921-1942.
- [5] E. A. Little, Neutron-irradiation hardening in irons and ferritic steels, Int Metals Rev March 1976 25-60.
- [6] P. D. Wilson, The Nuclear Fuel Cycle, Oxford University Press (1996).
- [7] Charles. O. Smith, Nuclear Reactor Materials, Addison-Wesley Pub. Co (1967).
- [8] M. L. Grossbeck, Effect of Radiation on Strength and Ductility of Metals and Alloys, Comprehensive Nuclear Materials, Vol.1, Elsevier 2012.
- [9] Radiation Effects in Structural and Functional Materials for Fission and Fusion Reactors, Comprehensive Nuclear Materials, Vol.4, Elsevier 2012.
- [10] K.L. Murty, I. Charit, Structural materials for Gen-IV nuclear reactors: Challenges and opportunities, J. Nucl. Mater. 383 (2008) 189–195.
- [11] A. Kimura, H. Cho, N. Toda, R. Casada, H. Kishimoto, N. Iwata, S. Ukai, S. Ohtsuka, M. Fujiwara, in: Proceedings of ICAPP'06, Reno, USA, 2006, Paper #6456, p. 2229.
- [12] Steven J. Zinkle, Jeremy T. Busby, Structural materials for fission and fusion energy, Materials Today, Volume 12, Issue 11, November 2009, Pages 12-19.
- [13] G.R. Odette, T. Yamamoto, H.J. Rathbun, M.Y. He, M.L. Hribernik, J.W. Rensman, Cleavage fracture and irradiation embrittlement of fusion reactor alloys: mechanisms, multiscale models, toughness measurements and implications to structural integrity assessment, J. Nucl. Mater. Vol. 323, Issues 2–3, 2003, Pages 313-340.
- [14] P.J. Maziasz, Formation and stability of radiation-induced phases in neutron-irradiated austenitic and ferritic steels, J. Nucl. Mater. Vol. 169, 1989, Pages 95-115.
- [15] F.A Garner, M.B Toloczko, B.H Sencer, Comparison of swelling and irradiation creep behaviour of fcc-austenitic and bcc-ferritic/martensitic alloys at high neutron exposure, J. Nucl. Mater. Vol. 276, Issues 1–3, 1 January 2000, Pages 123-142.
- [16] C. H. Woo, Modeling irradiation growth of zirconium and its alloys, Radiation Effects and Defects in Solids. Vol. 144, Iss. 1-4, 1998.

- [17] H. Schroeder, H. Ullmaier, Helium and hydrogen effects on the embrittlement of iron- and nickel-based alloys, *J. Nucl. Mater.* Vol. 179–181, Part 1, March–April 1991, Pages 118-124.
- [18] K.J. Leonard, 4.06 - Radiation Effects in Refractory Metals and Alloys, In *Comprehensive Nuclear Materials*, edited by Rudy J.M. Konings, Elsevier, Oxford, 2012, Pages 181-213.
- [19] S. Ukai, 4.08 - Oxide Dispersion Strengthened Steels, In *Comprehensive Nuclear Materials*, edited by Rudy J.M. Konings, Elsevier, Oxford, 2012, Pages 241-271.
- [20] R.M. Boothby, 4.04 - Radiation Effects in Nickel-Based Alloys, In *Comprehensive Nuclear Materials*, edited by Rudy J.M. Konings, Elsevier, Oxford, 2012, Pages 123-150.
- [21] A.F. Rowcliffe, L.K. Mansur, D.T. Hoelzer, R.K. Nanstad, Perspectives on radiation effects in nickel-base alloys for applications in advanced reactors, *J. Nucl. Mater.* Vol. 392, Issue 2, 15 July 2009, Pages 341-352.
- [22] Thomas M. Angeliu, John T. Ward, Jonathan K. Witter, Assessing the effects of radiation damage on Ni-base alloys for the prometheus space reactor system, *J. Nucl. Mater.* Vol. 366, Issues 1–2, 30 June 2007, Pages 223-237.
- [23] Benes, O., C. Cabet, S. Delpech, P. Hosnedl, V. Ignatiev, R. Konings, D. Lecarpentier et al. "Review Report on Liquid Salts for Various Applications, Deliverable D50, Assessment of Liquid Salts for Innovative Applications." ALISIA project, Euratom 7th FWP 2008.
- [24] F. Onimus and J.L. Béchade, 4.01 - Radiation Effects in Zirconium Alloys, In *Comprehensive Nuclear Materials*, edited by Rudy J.M. Konings, Elsevier, Oxford, 2012, Pages 1-31.
- [25] L.L. Snead, Y. Katoh and T. Nozawa, 4.07 - Radiation Effects in SiC and SiC–SiC, In *Comprehensive Nuclear Materials*, edited by Rudy J.M. Konings, Elsevier, Oxford, 2012, Pages 215-240.
- [26] P.J. Maziasz and J.T. Busby, 2.09 - Properties of Austenitic Steels for Nuclear Reactor Applications, In *Comprehensive Nuclear Materials*, edited by Rudy J.M. Konings, Elsevier, Oxford, 2012, Pages 267-283.
- [27] F.A. Garner, 4.02 - Radiation Damage in Austenitic Steels, In *Comprehensive Nuclear Materials*, edited by Rudy J.M. Konings, Elsevier, Oxford, 2012, Pages 33-95.
- [28] Corwin, William R. "US Generation IV reactor integrated materials technology program." *Nuclear Engineering and Technology* 38, no. 7 (2006): 591.

- [29] T.R. Allen, J.I. Cole, J. Gan, G.S. Was, R. Dropek, E.A. Kenik, Swelling and radiation-induced segregation in austenitic alloys, *J. Nucl. Mater.* Vol. 342, Issues 1–3, 30 June 2005, Pages 90-100.
- [30] E.A. Little, D.A. Stow, Void-swelling in irons and ferritic steels: II. An experimental survey of materials irradiated in a fast reactor, *J. Nucl. Mater.* Vol. 87, Issue 1, November 1979, Pages 25-39.
- [31] B. Raj and M. Vijayalakshmi, 4.03 - Ferritic Steels and Advanced Ferritic–Martensitic Steels, In *Comprehensive Nuclear Materials*, edited by Rudy J.M. Konings, Elsevier, Oxford, 2012, Pages 97-121.
- [32] M. J. Fluss, P. Hosemann and J. Marian, Charged-Particle Irradiation for Neutron Radiation Damage Studies. *Characterisation of Materials.* 1–17, 2012.
- [33] I. Hore-Lacy. *Nuclear Energy in the 21st Century.* 2nd Ed. World Nuclear University Press 2010.
- [34] Y. Dai, G.R. Odette and T. Yamamoto, 1.06 - The Effects of Helium in Irradiated Structural Alloys, In *Comprehensive Nuclear Materials*, edited by Rudy J.M. Konings, Elsevier, Oxford, 2012, Pages 141-193.
- [35] T Tanaka, K Oka, S Ohnuki, S Yamashita, T Suda, S Watanabe, E Wakai, Synergistic effect of helium and hydrogen for defect evolution under multi-ion irradiation of Fe–Cr ferritic alloys, *J. Nucl. Mater.* Vol. 329–333, Part A, 1 August 2004, Pages 294-298.
- [36] A.S. Kumar, Influence of helium-generated interstitials in dual ion irradiations, *J. Nucl. Mater.* Vol. 133–134, August 1985, Pages 482-485.
- [37] Levy, Viviane, Didier Gilbon, and Christian Rivera. Influence of helium on swelling of steels. *ASTM STP 870 (1985):* 317-329.
- [38] Yves Serruys, Marie-Odile Ruault, Patrick Trocellier, Sandrine Miro, Alain Barbu, Loïc Boulanger, Odile Kaïtasov, Sylvain Henry, Olivier Leseigneur, Philippe Trouslard, Stéphanie Pellegrino, Sylvain Vaubaillon, JANNUS: experimental validation at the scale of atomic modelling, *Comptes Rendus Physique*, Volume 9, Issues 3–4, April–May 2008, Pages 437-444.
- [39] M.L. Jenkins, Characterisation of radiation-damage microstructures by TEM, *J. Nucl. Mater.* Vol. 216, October 1994, Pages 124-156.
- [40] C.A. English, Low-dose neutron irradiation damage in FCC and BCC metals, *J. Nucl. Mater.* Vol. 108–109, July–August 1982, Pages 104-123.

- [41] E.A. Kenik, Radiation-induced segregation in irradiated Type 304 stainless steels, *J. Nucl. Mater.* Vol. 187, Issue 3, May 1992, Pages 239-246.
- [42] R.D. Carter, D.L. Damcott, M. Atzmon, G.S. Was, E.A. Kenik, Effects of proton irradiation on the microstructure and microchemistry of type 304L stainless steel, *J. Nucl. Mater.* Vol. 205, October 1993, Pages 361-373.
- [43] D.S. Gelles, Microstructural examination of commercial ferritic alloys at 200 dpa, *J. Nucl. Mater.* Vol. 233–237, Part 1, 1 October 1996, Pages 293-298.
- [44] Z. Yao, M. Hernández-Mayoral, M.L. Jenkins & M.A. Kirk, Damage evolution in thin-foils at lower doses. Pages 2851-2880, *Philosophical Mag*, Vol 88, Issue 21, 2008
- [45] M. L. Jenkins , K.-H. Katerbau , M. Wilkens, Transmission electron microscopy studies of displacement cascades in Cu₃Au. Pages 1141–1153, *Philosophical Mag*, Vol. 34, Iss. 6, 1976.
- [46] M.L. Jenkins and M. Wilkens, *Philos. Mag. A* 34 (1976) 1155.
- [47] M. Wilkens, M.L. Jenkins and K.-H. Katerbau, *Phys. Status Solidi A* 39 (1977) 103.
- [48] Xianglin Wu, Xiao Pan, James C. Mabon, Meimei Li, James F. Stubbins, An EBSD investigation on flow localization and microstructure evolution of 316L stainless steel for Gen IV reactor applications, *J. Nucl. Mater.* Vol. 371, Issues 1–3, 15 September 2007, Pages 90-97.
- [49] J Chen, Y Dai, F Carsughi, W.F Sommer, G.S Bauer, H Ullmaier, Mechanical properties of 304L stainless steel irradiated with 800 MeV protons, *J. Nucl. Mater.* Vol. 275, Issue 1, October 1999, Pages 115-118.
- [50] M. Fulger, D. Ohai, M. Mihalache, M. Pantiru, V. Malinovschi, Oxidation behavior of Incoloy 800 under simulated supercritical water conditions, *J. Nucl. Mater.* Vol. 385, Issue 2, 31 March 2009, Pages 288-293.
- [51] R.W. Cahn, *Physical Metallurgy* 4th ed., Elsevier Ltd, 1996.
- [52] M.B. Lewis, N.H. Packan, G.F. Wells, R.A. Buhl, Improved techniques for heavy-ion simulation of neutron radiation damage, *Nuclear Instruments and Methods*, Volume 167, Issue 2, 20 December 1979, Pages 233-247.
- [53] K. Farrell, Experimental effects of helium on cavity formation during irradiation—a review. *Radiation Effects*. Vol. 53, Iss. 3-4, 1980.
- [54] Lu, Tao, Yuqin Qiao, and Xuanyong Liu. Surface modification of biomaterials using plasma immersion ion implantation and deposition. *Interface focus* 2, no. 3 (2012): 325-336.

- [55] G.S. Was and R.S. Averback, 1.07 - Radiation Damage Using Ion Beams, In Comprehensive Nuclear Materials, edited by Rudy J.M. Konings, Elsevier, Oxford, 2012, Pages 195-221.
- [56] Kulcinski, GL, Brimhall, JL, Kissinger, HE (1972) Production of Voids in Pure Metals by High-Energy Heavy-Ion Bombardment, Proc. 1971 International Conference on Radiation Induced Voids in Metals, Albany, New York, June 1971, USAEC, CONF-710601, NTIS.
- [57] S.D. Washko, G. Aggen. Metals Handbook: Properties and Selection: Irons, Steels, and High-Performance Alloys (10th ed.), Vol. 1 ASM International, Materials Park, OH (1990), pp. 841–907.
- [58] Transmission Electron Microscopy: A Textbook for Materials Science, Vol 3. D. B. Williams, C. B. Carter, Springer (2009).
- [59] B.N. Singh, J.H. Evans, Significant differences in defect accumulation behavior between fcc and bcc crystals under cascade damage conditions, J. Nucl. Mater. Vol. 226 (1995) Pages 277 - 285.
- [60] M.J. Caturla, N. Soneda, E. Alonso, Comparative study of radiation damage accumulation in Cu and Fe, J. Nucl. Mater. Vol. 276 (2000) Pages 13 - 21.
- [61] J.P. Hirth, J. Lothe, Theory of Dislocations, second ed., Wiley, New York, 1982.
- [62] J.R. Michael, Focused ion beam induced microstructural alterations: texture development, grain growth, and intermetallic formation, Microsc. Microanal. Vol. 17 (2011) Pages 386 - 397.

APPENDICES

Below are the full versions of publications arising from this work.

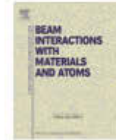
Nuclear Instruments and Methods in Physics Research B 295 (2013) 38–41



Contents lists available at SciVerse ScienceDirect

Nuclear Instruments and Methods in Physics Research B

journal homepage: www.elsevier.com/locate/nimb



Electron backscatter diffraction characterization of plasma immersion ion implantation effects in stainless steel

Joel Davis^{a,*}, Ken Short^a, Richard Wuhrer^b, Matthew R. Phillips^c, Gregory R. Lumpkin^a, Karl R. Whittle^d

^aInstitute of Materials Engineering, Australian Nuclear Science and Technology Organization, Australia
^bAdvanced Materials Characterisation Facility (AMCF), University of Western Sydney, Australia
^cMicrostructural Analysis Unit, Faculty of Science, University of Technology Sydney, Australia
^dSchool of Materials Science and Engineering, University of Sheffield, South Yorkshire, UK

ARTICLE INFO

Article history:
Received 9 July 2012
Received in revised form 17 October 2012
Available online 31 October 2012

Keywords:
Electron backscattering diffraction (EBSD)
Scanning electron microscopy (SEM)
Radiation damage
Ion implantation

ABSTRACT

In these experiments plasma immersion ion implantation is utilised to simulate some of the radiation effects in a nuclear reactor environment. Scanning electron microscopy using the angular selective backscatter detector has revealed observable changes in crystallographic contrast after irradiation with helium ions. Further studies using electron backscatter diffraction in both plan and cross section view allow us to visualize the extent and depth of damage and observe differences in the behavior of different crystalline phases present in several grades of stainless steel.

© 2012 Elsevier B.V. All rights reserved.

1. Introduction

The study of nuclear reactor materials, both existing and proposed, is important to ensure their reliability and integrity when exposed to radiation damage during their service life. By understanding the damage mechanisms of such materials, existing materials can be optimised and new improved materials can be developed.

The simulation of a neutron irradiation environment using ion implantation has been chosen as an alternative to reactor based neutron irradiation, without activating the material. Helium ions can damage regions in a metal alloy's microstructure primarily through atomic displacement. Point defects are formed and when these point defects are mobile they can cluster forming point defect agglomerates and voids [1]. The implanted helium ions may reside in these voids and change their time dependent growth dynamics similar to those observed in fast neutron radiation damage studies [2]. A schematic representation of these effects is shown in Fig. 1.

The plasma immersion ion implantation (PI³) process forms positively-charged ions within a radio frequency (RF) excited plasma, followed by acceleration of the positive ions into the material by negative high voltage pulse bias of the target material. This method was designed to implant large areas of samples

simultaneously to very high fluences and has been used for surface hardening and improving corrosion properties of metals [3].

Farrell [4] has shown the importance of helium gas (predominantly formed by nuclear transmutations) in radiation damage studies promoting the formation of cavities and enhancing the dislocation structure. Current research is focused on radiation damage and microstructural helium tolerance by helium ion implantation in materials that have applications in both fission and fusion reactor technologies e.g. inert matrix fuels, reactor core liners, fuel cladding and structural materials within the reactor [5].

In this research the effect of PI³ induced helium ion damage on materials has been studied using scanning electron microscopy (SEM) techniques such as angle selective backscatter (ASB) and electron backscatter diffraction (EBSD). Angle selective backscattering is a form of BSE channeling contrast imaging where single elastically scattered electrons are imaged, revealing both crystalline grain orientation and sub-grain information with very high contrast [6]. Bringing the detector very close to the sample in the absence of a magnetic field can increase the backscattered electron image resolution and can be used to selectively filter out atomic number contrast, leaving only orientation information behind. Electron backscattered diffraction mapping was then used determine the damaged areas in both plan view and cross-section.

For EBSD to be observable the sample must be crystalline, satisfying the Bragg condition and free from gross deformation [7]. Dislocations, crystallographic defect density and grain orientation information all give rise to information that reveals those areas

* Corresponding author.
E-mail address: joel.davis@ansto.gov.au (J. Davis).

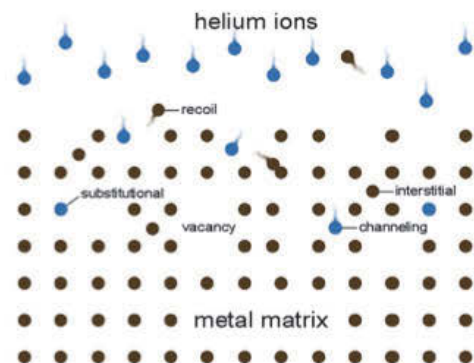


Fig. 1. Schematic representation of the initial formation of point defects created in the metal matrix as a result of helium ion implantation.

Table 1
SRIM calculation results for the helium implantation at 30 kV of the stainless steels in these experiments.

Grade	Mean depth (nm)	Max. depth (nm)	Vacancies/ion	Total atoms sputtered/ion
316	116	240	1.18E+02	0.0634
304	115	240	1.20E+02	0.0764
430	119	240	1.16E+02	0.0826
MA956	125	250	1.13E+02	0.074
2205 (FCC)		115	230	1.18E+02
0.0902				
2205 (BCC)		119	220	1.16E+02
0.0878				

Table 2
Summary of stainless steel grades and crystal structures as used in these experiments.

Grade	Crystal structure	Composition (wt.%)
316	FCC	Cr 17, Ni 12 Mo 2
304	FCC	Cr 18, Ni 8
430	BCC	Cr 17
MA956	BCC	Cr 19, Al 4
2205	FCC/BCC	Cr 22 Ni 5 Mo 3

affected by radiation damage. If these damaged areas contain enough defects, the coherence of the diffraction pattern is lost, and indexing is not possible.

Through the use of computer based SRIM calculations (Stopping Range of Ions in Matter) we are able to predict an expected depth of damage for a given material, which was then compared to the experimental results [8], see Table 1.

In this paper, results are presented from BSE channeling contrast imaging and EBSD mapping of several grades of stainless steel, both ferritic and austenitic, which have been implanted using helium ions via plasma ion implantation at the same dose. It will be shown how EBSD mapping can reveal a preferential pattern loss for specific phases in the stainless steel after helium ion implantation.

2. Material and methods

The materials studied in this investigation consist of five grades of stainless steel; two austenitic; two ferritic grades and one

duplex as outlined in Table 2. The stainless steel samples were prepared for EBSD analysis following the Struers method for polishing Low Carbon Steels (Method No. 1879). The samples were then mapped using a Zeiss Ultra Plus SEM coupled with an Oxford Instruments HKL NordlysS EBSD detector system at an accelerating voltage of 20 kV. The EBSD maps were generated using the HKL Channel 5 software.

PI^3 ion implantation using helium at 30 kV and a fluence of $\sim 1 \times 10^{17}$ ions cm^{-2} was used for the irradiation. Portions of the materials were shielded using paint to provide an interface between damage and undamaged regions for comparison.

Post-irradiation BSE channeling contrast imaging and EBSD mapping were used to analyse both shielded and non-shielded surfaces. The BSE channeling contrast imaging and EBSD mapping was done with 20 kV accelerating voltage in high current mode with the 60 μm aperture. Individual EBSD map resolution is reported in the respective figure captions. The Instrumented indentation to maximum loads of 50 and 250 mN was performed with an Agilent Technologies C300 NanoIndenter on the 316 stainless steel to determine if a change was present in surface hardness post-irradiation. A 5–10% increase in surface hardness was measured for helium irradiated 316SS samples.

SRIM simulations using default elemental values put the expected damage depth in the sub 150 nm range (see Table 2). Therefore several methods of preparing cross sections were trialed with the intention of minimising edge rounding. The method with the best achievable edge retention was precision ion beam polishing (PIPS).

The samples were prepared by sectioning the material using a precision cut-off machine and bonding the material face to face (irradiated sides). The ion beam polishing was carried out in several steps using different accelerating voltages, angles and time (see Table 3). The cross-sections were then imaged in the SEM using BSE channeling contrast imaging and mapped with EBSD.

3. Results and discussion

Helium ion implantation with PI^3 significantly degraded both BSE channeling contrast images and EBSD patterns in the unshielded regions of the stainless steel samples in plan view. Fig. 2a–d shows the BSE channeling contrast images, where the top section has been shielded and the bottom section exposed to the ion implantation. The shielded region shows high contrast orientation information, clearly defined grain boundaries and sub-grain information. The quality of the BSE channeling contrast image in the exposed area is significantly degraded; however, some contrast is still visible. These initial BSE channeling contrast images prompted further investigation using EBSD.

Fig. 3a–d shows the corresponding EBSD maps for the same materials imaged using BSE channeling contrast imaging. Once again the top portion of the map is shielded and the lower region exposed to the ion implantation. The EBSD orientation maps show a degraded image in the exposed area at the bottom of the maps; this is due to the poor quality Kikuchi patterns being formed on the EBSD detector screen whilst acquiring the map. It is not easy to index the pattern when the Kikuchi bands become diffuse and/or distorted. This is due to the loss of coherence in the diffraction pattern primarily from point defects and dislocations from damage cascades formed within the material during ion implantation.

The loss of pattern in the EBSD orientation maps also reveals a trend for the two different phases present in the stainless steel materials tested. In the FCC iron phase in the 304 grade stainless steel shown in Fig. 2a it can be seen that the EBSD pattern is completely lost in the exposed region. If we compare this to the BCC iron phase containing 430 and MA956 grade stainless steels shown in Fig. 3b and c, it can be seen that the EBSD pattern still retains partial indexing in the exposed regions.

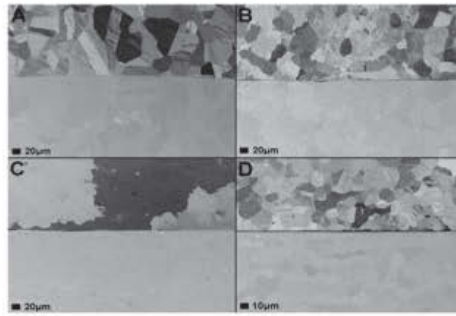


Fig. 2. BSE channeling contrast images of the shielded to unshielded interface in plan view of (a) 304 grade stainless steel, (b) 430 grade stainless steel, (c) MA956 oxide dispersed strengthened (ODS) steel and (d) 2205 duplex stainless steel, implanted with helium ions at 30 kV and a fluence of $\sim 1 \times 10^{17}$ ions cm^{-2} .

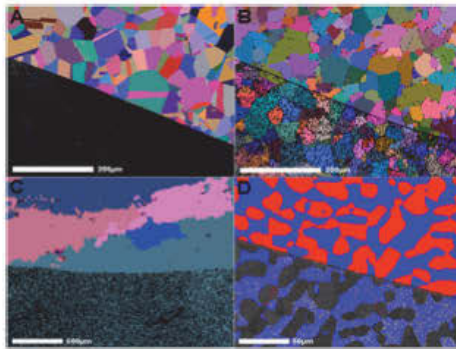


Fig. 3. EBSD orientation maps of the shielded to unshielded interface in plan view of (a) 304 grade stainless steel, 100 \times magnification, 280 \times 210, 4 μm step size (b) 430 grade stainless steel, 200 \times magnification, 187 \times 140, 3 μm step size (c) MA956 oxide dispersed strengthened (ODS) steel, 50 \times magnification, 283 \times 212, 8 μm step size and (d) a phase map of the 2205 duplex stainless steel, 200 \times magnification, 281 \times 211, 2 μm step size. In this map we have assigned the FCC iron phase with a red colour and the BCC iron phase with a blue colour. All samples were implanted with helium ions at 30 kV and a fluence of $\sim 1 \times 10^{17}$ ions cm^{-2} . (For interpretation of the references to colour in this figure legend, the reader is referred to the web version of this article.)

The EBSD phase map of 2205 grade stainless steel shown in Fig. 3d further supports the observed trend. In this map we have assigned the FCC iron phase with a red colour and the BCC iron phase with a blue colour. In the exposed region it is clear that the FCC iron phase is not being indexed and the BCC iron phase is still partially indexed in the same way we have seen in Fig. 3a and b. This observation agrees with several studies from the literature for ion implantation or neutron irradiation studies in metals that show a lower tolerance to radiation damage for FCC metals when compared to BCC metals [9–11]. When subjected to neutron or ion irradiation FCC metals have been shown to form large dislocation clusters which can lead to the formation of stacking fault tetrahedra even at low doses. The mobility of these dislocation clusters is determined by the stacking fault energy (SFE) [11,12]. Work by Michael [13] has shown that ion beam irradiation can cause significant microstructural changes in FCC metals with fine

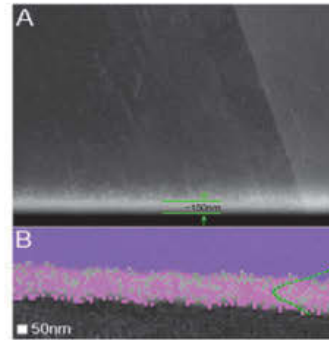


Fig. 4. (a) BSE channeling contrast image of an irradiated 316 stainless steel cross-section showing a ~ 150 nm band with a distinct change in contrast in the expected damage region. (b) Corresponding EBSD map of this region showing the loss of EBSD pattern in the damage region, a misorientation of between 3 and 5 degrees is also observed between the damage layer and parent metal in this EBSD map. The SRIM depth distribution curve is also shown.

grain structure. Changes include new grain formation in the channeling direction parallel to the ion beam, however no changes were observed in the BCC metals.

The EBSD patterns may have been lost due to a sputtering effect or physical damage to the highly polished sample surface; however it must be noted that the SRIM calculations in Table 2 shows the sputtering yield to be minimal for all materials tested. Cross-sections were then prepared to confirm the observations made in plan view. Fig. 4 shows a cross-section sample prepared using PIPS from the 316 stainless steel, which had been implanted with helium ions to the same dose as the other materials in these experiments. SRIM calculations put the expected mean damage layer at a depth of ~ 116 nm with a peak depth of ~ 240 nm, the critical damage fluence will be somewhere between these values. Fig. 4a shows a BSE channeling contrast image of an approximately 150 nm band with a distinct change in contrast in this expected critical damage fluence region. Fig. 4b confirms the loss of EBSD pattern is also observed in the cross-section, a misorientation of between 3 and 5 degrees is also observed between the damage layer and parent metal. The depth of damage in this EBSD map is similar to that observed in the BSE channeling contrast image. The SRIM depth distribution curve is superimposed over the EBSD map to demonstrate how the experimental data agrees with the computer based simulations. It should be noted that the EBSD performed on the cross-sections was done at higher resolution than the plan view samples and because of this we were able to achieve approximately 30% better indexing. However at this increased magnification the area mapped is significantly reduced and we are only mapping one grain at a time, which would not have allowed us to reveal the trends seen when mapping large areas in plan view.

Atomic force microscopy (AFM) has also been utilised on all the materials in this study to determine whether a change in surface

Table 3

Summary of precision ion polishing steps used for preparing the stainless steel cross sections used in these experiments.

Step	Energy (kV)	Angle ($^{\circ}$)	Time (h)
1	5	4	6
2	4.5	3	3
3	4	3	1–2

topography is apparent between the irradiated and shielded regions of the sample surface. The AFM was done in contact mode using a Veeco Digital Instruments D3000 with IIIa controller. No change in surface topography was measured within a scan area that spanned the irradiated/unirradiated interface region. However in previous studies implanting using argon ions in 316 stainless steel to the same energy and fluence, some evidence of sputtering and surface degradation was measured using AFM [14].

4. Conclusion

In this study the effect of ion implantation using helium ions on various grades of stainless steel was examined using angular selective backscatter imaging and electron backscatter diffraction mapping techniques.

The BSE channeling contrast imaging reveals high contrast orientation information, clearly defined grain boundaries and sub-grain information on the highly polished stainless steel samples. The quality of the BSE channeling contrast image in the exposed area is significantly degraded although some contrast is still visible.

The EBSD orientation and phase maps show a loss of indexing or poor quality Kikuchi patterns being formed in the areas exposed to helium ion implantation. This is due to point defects and dislocations in the stainless steel samples causing a loss of coherence in the diffraction patterns during EBSD acquisition.

Preferential loss of indexing of the FCC phase over the BCC ferritic phase is in agreement with a relative higher rate of radiation point defect formation observed in FCC crystals.

Cross-sections prepared in this study confirm the observations made in plan view along with AFM results from which we can

say this is not as a result of surface roughening by sputtering away of the highly polished sample surface.

In summary, BSE channeling contrast imaging and EBSD mapping techniques as mentioned in this paper may be used as a qualitative method in radiation damage studies.

Acknowledgements

The authors would like to acknowledge the support with metallography and sample preparation from Tim Palmer, Clint Jennison and Robert Aughterson from the Institute of Materials Engineering, Australian Nuclear Science and Technology Organization (ANSTO). The authors would also like to thank the University of Technology, Sydney (UTS).

References

- [1] R.W. Cahn, *Physical Metallurgy*, fourth ed., Elsevier Ltd., 1996.
- [2] M.B. Lewis, N.H. Packan, G.F. Wells, R.A. Buhl, *Nucl. Instr. Meth.* 167 (1979) 233.
- [3] M.J. Kenny, L.S. Wielunski, J. Tendys, G.A. Collins, *Nucl. Instr. Meth. B* 80–81 (1993) 262.
- [4] K. Farrell, *Radiat. Eff. Defects Solids* 53 (2006) 175.
- [5] S.J. Zinkle, J.T. Busby, *Mater. Today* 12 (2009) 12.
- [6] M. Laysberg, K. Tillmann, *EMC 2008: Instrumentation and Methods*, Springer-Verlag, Berlin Heidelberg, 2008.
- [7] B.D. Cullity, *Elements of X-ray Diffraction*, second ed., Addison-Wesley, Reading, MA, 1978.
- [8] J.F. Ziegler, M.D. Ziegler, J.P. Biersack, *Nucl. Instr. Meth. B* 268 (2010) 1818.
- [9] B.N. Singh, J.H. Evans, *J. Nucl. Mater.* 226 (1995) 277.
- [10] C.A. English, *J. Nucl. Mater.* 108 (1982) 123.
- [11] M.J. Caturla, N. Soneda, E. Alonso, *J. Nucl. Mater.* 276 (2000) 13.
- [12] J.P. Hirth, J. Lothe, *Theory of Dislocations*, second ed., Wiley, New York, 1982.
- [13] J.R. Michael, *Microsc. Microanal.* 17 (2011) 386.
- [14] J. Davis, K. Short, R. Wührer, M. Phillips, K. Whittle, *Microsc. Microanal.* 17 (2011) 1886.

EBSD Studies of Ion Implanted Duplex Stainless Steel

J. Davis¹, K. Short¹, R. Wuhrer², M. R. Phillips², G. R. Lumpkin¹ and K. R. Whittle¹

1. Institute of Materials Engineering, Australian Nuclear Science and Technology Organization
2. Microstructural Analysis Unit, Faculty of Science, University of Technology, Sydney.

The study of current and future reactor materials has important implications from a safety and longevity standpoint. There has been a historical increase in the service life of nuclear reactors that results in reactor materials being exposed to higher doses over longer periods of time [1]. It is therefore critical that research is carried out to understand the radiation effects on the microstructure of these materials and develop new methods to characterise the damage mechanisms.

Ion implantation has long been used as an alternative method to neutron irradiation for the simulation of a nuclear reactor environment. The use of helium ions provides a mechanism for damage through atomic displacement leading to point defects and possible defect clusters and voids. Residual helium ions may also remain trapped in the voids created changing the materials recovery dynamics [2]. Research is currently being done to study the microstructural effects of helium ion implantation on 2205 duplex stainless steel using SEM imaging techniques and electron backscattered diffraction (EBSD). This duplex steel consists of an equal distribution of both FCC iron and BCC iron phases making it the perfect candidate to examine the inherent differences in tolerance to radiation damage of these two phases.

The experimental procedure involved preparing the 2205 duplex stainless steel for EBSD analysis using a modified Struers method for polishing Low Carbon Steels (Method No. 1879). The sample was imaged using a Zeiss Ultra Plus SEM equipped with an angular backscatter detector (AsB). An Oxford Instruments HKL NordlysS detector system and HKL Channel 5 software was used for EBSD mapping. Ion implantation was carried out using plasma immersion ion implantation (PII) at 30 kV accelerating voltage to a fluence of $\sim 1 \times 10^{17}$ ions cm^{-2} . Part of the sample was shielded in order to give an interface where the irradiated and non-irradiated material could be studied using SEM imaging and EBSD techniques.

Fig 1. shows the angular selective backscatter image of the 2205 duplex stainless steel after ion implantation. The top half of the image is shielded from the irradiation and the lower half is exposed. We see a loss of the crystallographic image contrast in the irradiated region as a result of the atomic displacement of atoms creating point defects in the material due to ion implantation.

Fig 2. shows an electron backscatter diffraction phase map of the 2205 duplex stainless steel. The red colour is assigned to the FCC iron phase and the blue colour is assigned to the BCC iron phase. The top half of the map is the shielded region and the lower half has been exposed. We see a complete loss of indexing in the FCC iron phase however the BCC phase is still partially indexed. Indexing of the FCC iron phase is not possible due to point defects created by the ion implantation causing a loss of coherence in the diffraction patterns. By mapping this material using EBSD we can see how the BCC phase is more tolerant to the effects of the irradiation dose used in this experiment, less point defects have occurred and remained in the BCC phase [3]. The ability of the two phases in this material to recover from atomic displacements depends on the mobility of the point defects and whether clustering occurs. How the phase recovers dynamically will also depend on this mobility of these defect clusters.

This paper will present the SEM AsB imaging and EBSD findings from a number of stainless steel samples investigated. EBSD pattern quality and cross sectional sampling results will be also presented. Future research will look at the effect of changing the energy and dose.

References

- [1] C.R.F. Azevedo. "A review on neutron-irradiation-induced hardening of metallic components" *Engineering Failure Analysis*, Volume 18, Issue 8, December 2011, Pages 1921-1942, ISSN 1350-6307, 10.1016/j.engfailanal.2011.06.008.
- [2] M. B. Lewis, N. H. Packan, G. F. Wells And R. A. Buhl. "Improved Techniques For Heavy-Ion Simulation Of Neutron Radiation Damage" *Nuclear Instruments and Methods*, Volume 167, Issue 2, 20 December 1979, Pages 233-247, ISSN 0029-554X, 10.1016/0029-554X(79)90011-9.
- [3] J Davis, K Short, R Wuhler, M Phillips and K Whittle (2011). Plasma Immersion Ion Implantation of Stainless Steel 316. *Microscopy and Microanalysis*, 17 (Suppl. 2) , pp 1886-1887 doi:10.1017/S1431927611010300

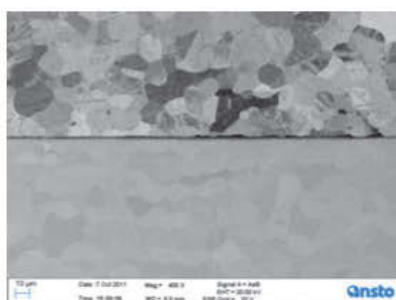


Fig. 1. AsB images of the 2205 duplex stainless steel implanted with helium ions at 30 kV accelerating voltage and to a fluence of $\sim 1 \times 10^{17}$ ions cm^2 . This image shows the loss of crystallographic contrast in the lower unshielded region.

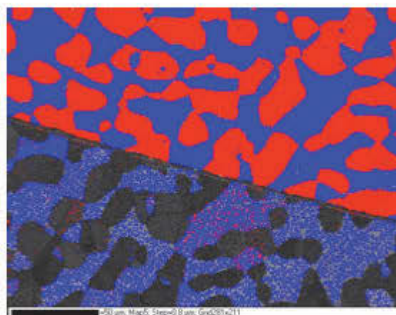


Fig. 2. EBSD phase map of the 2205 duplex stainless steel implanted with helium ions at 30 kV accelerating voltage and to a fluence of $\sim 1 \times 10^{17}$ ions cm^2 . The red colour is assigned to the FCC iron phase and the blue colour is assigned to the BCC iron phase. The top half of the map is the shielded region and the lower half has been exposed. We see a loss of indexing of the FCC phase.

Plasma Immersion Ion Implantation of Stainless Steel 316

J. Davis*, K. Short*, R. Wuhrer**, M. R. Phillips** and K. Whittle*

* Institute of Materials Engineering, Australian Nuclear Science and Technology Organization.

** Microstructural Analysis Unit, Faculty of Science, University of Technology, Sydney.

Plasma immersion ion implantation (PI³) is a method designed to implant large areas of samples simultaneously, to very high fluences, with a small energy variation. It originally grew out of an ANSTO project in the 1980's investigating the fundamental properties of plasmas relevant for use in nuclear fusion. The process involves forming an ionised plasma at a controlled temperature with radio frequency (RF) excitation. Ion implantation occurs when the positive ions from the plasma are accelerated towards all exposed surfaces by applying a high negative voltage to the sample. It has previously been used for surface hardening and improving corrosion properties of metals. This ion implantation technique is being used to simulate the effects from a neutron irradiation environment and study the effects on various materials.

Research is currently in progress to determine the effect of PI³ has on a 316 stainless steel microstructure, utilising argon and helium ions as damaging ions. The overall aim of the research is to eventually investigate other unique materials that have applications in both GenIV and fusion reactor programs, and the Advanced Fuel Cycles (AFCI) e.g. inert matrix fuels, reactor core liners, structural materials within the reactor (ODS materials). The main focus of this work will be to understand grain-boundary interactions, and how they relate to the tolerance of materials to damage.

A small piece of 316 stainless steel was prepared for EBSD analysis using the Struers method for polishing Low Carbon Steels (Method No. 1879). The sample was then mapped using a Zeiss Ultra Plus SEM with an Oxford Instruments HKL NordlysS detector system. The map was generated using the HKL Channel 5 software. Ion implantation utilising two different noble gases, argon and helium respectively at 40 kV accelerating voltage, and to a fluence of $\sim 1 \times 10^{17}$ ions cm^{-2} was used. Portions of the materials were shielded using both a silicon wafer and a TEM grid. Post irradiation EBSD was used to analyse both the shielded and non-shielded surfaces.

Fig. 1 shows the BSE image of the irradiated and shielded regions and also the region where the EBSD map was taken from on the polished stainless steel surface, where a) Argon ions were used for implantation and b) Helium ions were used for implantation. Fig. 2a shows the EBSD map of the type 316 stainless steel before ion implantation and Figure 2b shows the corresponding EBSD map showing the loss of EBSD pattern in the irradiated region.

PI³ using argon and helium ions significantly degraded the backscattered electron image and EBSD patterns on the 316 stainless steel sample. Irradiation induced dislocations/damage affected the crystallinity of the surface. Physical damage from the

irradiation to the surface preparation for EBSD, removing the coherent scattering, and effectively gave rise to diffuse scattering from the surface.

Current research and future research investigation of these and many other materials will be discussed. Cross sections of the irradiated steel are being prepared to determine the penetration depth of the damage and whether EBSD patterns are obtainable from the cross section. The affect of type of ion will also be discussed. Helium ions should have penetrated further than argon, predominantly due to the mass/energy ratio of argon/helium. Further experiments will be focused on a range of doses in combination with nano-indentation, to study the effect of radiation on the recovery from stress in materials, and the role it plays in recovery.

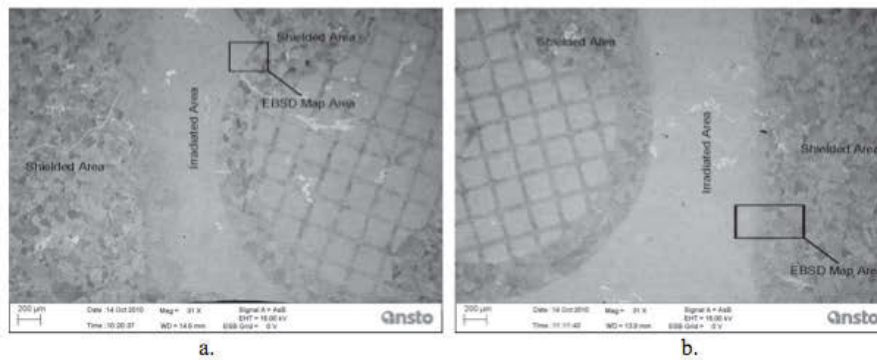


Figure 1. Backscattered electron image showing the irradiated and shielded regions and also the region where the EBSD map was taken from on the polished stainless steel surface. a) Argon ions were used for implantation and b) Helium ions were used for implantation.

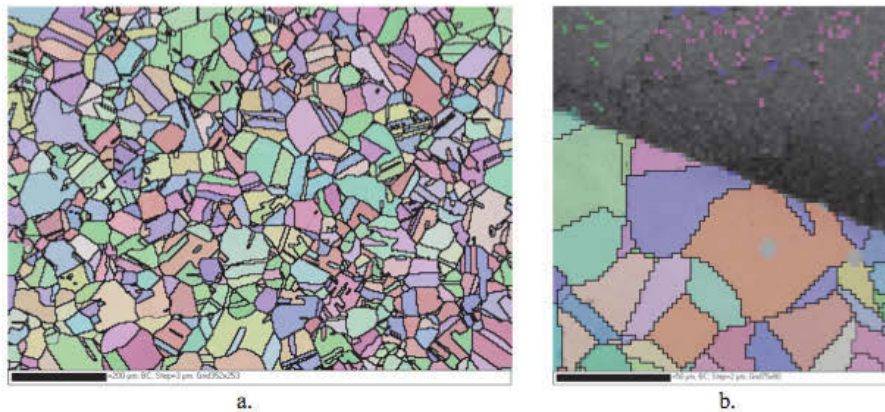


Fig. 2. EBSD map showing the loss of EBSD pattern in the irradiated region (top of map).